DISS. ETH NO. 26110

BARIUM TITANATE POCKELS MODULATORS INTEGRATED WITH SILICON PHOTONIC CIRCUITS

A thesis submitted to attain the degree of

DOCTOR OF SCIENCES of ETH ZURICH
(Dr. sc. ETH Zurich)

presented by

FELIX ELTES
M. Sc. Eng., Lunds Universitet

born on 25 March 1991
citizen of Sweden

accepted on the recommendation of

Prof. Dr. M. Fiebig, examiner
Dr. Stefan Abel, co-examiner
Prof. Dr. Jérôme Faist, co-examiner
Dr. Frédéric Boeuf, co-examiner

2019

DOI: 10.3929/ethz-b-000373660

ABSTRACT

Driven by the ever-increasing demands of video streaming, social media, and cloud computing, the traffic inside data centers has exploded, reaching 10 ZB in 2019. To cope with the increasing traffic, optical communication, which was previously only used for long-distance communication, has made its way inside data centers. The development of high-speed optical transceivers based on silicon photonic integrated circuit (PIC) technology has allowed optical fibers to replace electrical wires for communication down to the rack-level (distances >1 m). By leveraging the existing complementary metal-oxide-semiconductor (CMOS) technology, silicon photonics is a highly integrated, cheap, and scalable platform for optical transceivers. However, the intrinsic performance of silicon PICs is limited and the scaling of transceiver data rates has had to rely on costly and complex multiplexing schemes.

The current limitation of silicon photonic bandwidth lies with the electro-optic modulator (EOM). The low efficiency of electro-optic effects in silicon fundamentally limits the achievable performance. To overcome this limitation alternative concepts for EOMs are being explored. One of the most promising approaches takes inspiration from long-distance optical communications where modulators exploit a different physical effect, the Pockels effect. To bring this effect to silicon PICs, combining the best of both worlds, requires heterogeneous integration of new materials. While many material systems have been, and are being, investigated, a viable technology to bring Pockels modulators to silicon photonics does not exist.

In this thesis, integration of Pockels modulators based on barium titanate ($BaTiO_3$, BTO) with silicon photonics was developed. To this end, three main challenges of integrated BTO-based devices were addressed: i) propagation losses, ii) proof of Pockels effect in BTO-on-Si, and iii) monolithic integration with silicon PICs.

Prior work on BTO-Si modulators has reported unexpectedly large propagation losses. In this thesis the origin of these losses was investigated, and found to be chemical reactions within the materials during device

fabrication. Based on this new insight, an adjusted fabrication process was used to produce BTO-on-Si waveguides with low propagation losses.

Based on the process for low-loss waveguides and with integration aspects in mind, a new waveguide cross-section was developed and used to probe the electro-optic (EO) properties of the BTO thin films. For the first time unambiguous proof of the Pockels effect in BTO-on-Si devices was shown in the form of an anisotropic EO response, a large EO bandwidth of 30 GHz, and a hysteresis of the EO response caused by ferroelectric switching in BTO. The measured Pockels coefficients are close to those of bulk BTO, and the r_{42} coefficient of 923 pm/V ($\lambda = 1.55$ μm) is the largest in-device coefficient reported for any material.

Having established the fundamental aspects of BTO as a material in BTO-Si waveguides, a scheme for integration with advanced silicon PICs was demonstrated: BTO modulators were fabricated in the back-end-of-line (BEOL) of PIC wafers through molecular wafer bonding. The integrated BTO modulators showed excellent performance metrics, and represent a milestone in PIC-compatible integration of Pockels modulators.

Since BTO-on-Si technology brings fundamentally new properties to silicon photonics, the platform was also explored beyond conventional EOMs. First, plasmonic BTO modulators were investigated. A novel fabrication process was developed to fabricate nano-scale plasmonic BTO modulators. Excellent thermal stability of the devices was shown, and their high-speed performance was demonstrated by data transmission experiments of 72 and 116 Gbps. Second, the potential for BTO to impact cryogenic PICs was explored. For the first time, the structural and EO properties of BTO-on-Si were measured at cryogenic temperatures. Crystalline phase transitions in the BTO were found to differ from those of bulk BTO crystals. The presence of a strong Pockels effect at 4 K was demonstrated, and the potential for real applications was shown with 4-K data transmission at a record rate of 20 Gbps.

The technology developed in this thesis provides a viable path for large-scale integration of high-performance Pockels modulators with advanced silicon PICs. Along the way, fundamental aspects of BTO-on-Si thin films have been explored leading to new understanding of the material. The demonstration of efficient EO modulators for cryogenic photonics removes the largest remaining roadblock towards the development of optical quantum technologies.

ZUSAMMENFASSUNG

Bedingt durch die rasant wachsende Nachfrage nach Videostreaming, sozialen Medien, und Cloud-Computing Diensten ist die Menge des Datenverkehrs innerhalb von Grossrechenzentrum explodiert. Im Jahr 2019 wurden mehr als 10 Zetabytes an Daten innerhalb solcher Rechenzentren versandt. Um diesen steigenden Datenverkehr zu bewältigen wird heutzutage eine optische Kommunikationstechnologie innerhalb von Rechenzentren verwendet, welche ursprünglich für die Kommunikation über grosse Distanzen entwickelt wurde. Durch die Entwicklung von optischen Hochgeschwindigkeitstransceivern auf einer Silizium-basierten integrierten optischen Technologie (Photonic Integrated Circuit, PIC) konnten für die Kommunikation zwischen verschiedenen Racks innerhalb eines Servers (Distanzen >1 m) elektrische Kabel durch Glasfasern ersetzt werden. Durch die Nutzung etablierter CMOS-Technologie (Complementary Metal Oxide Semiconductor) ist Siliziumphotonik (silicon photonics) eine integrierte, kostengünstige und skalierbare Plattform für optische Transceiver. Die intrinsische Leistung von optischen Schaltkreisen aus Silizium und die Skalierung der Datenraten von Transceivern sind jedoch auf kostspielige und komplexe Multiplexverfahren angewiesen.

Heutzutage begrenzen elektrooptische Modulatoren (EOM) die Bandbreite der Siliziumphotonik. Dabei beschränkt die geringe Effizienz der in Silizium verfügbaren elektrooptischen Effekte die maximal erzielbare Leistung der Modulatoren. Um diese Einschränkung zu überwinden werden alternative Konzepte für elektrooptische Modulatoren untersucht. Einer der vielversprechendsten Ansätze ist von der optischen Technologie inspiriert, die zur Überbrückung grosser Entfernungen verwendet wird, und die auf Modulatoren setzt, welche auf einem anderen physikalischen Effekt, dem sogenannten Pockels-Effekt, beruhen. Um diesen Effekt in einer Silizium-basierten Plattform zu verwenden und somit das Beste aus beiden Welten zu kombinieren ist eine heterogene Integration neuer Materialien nötig. Obwohl viele Materialsysteme sowohl in der Vergangenheit untersucht wurden als auch gegenwärtig untersucht werden, existiert heute keine praktikable Technologie, um Pockels-Modulatoren in einer Siliziumphotonik Plattform zu realisieren.

In dieser Arbeit wurde die Integration von auf Bariumtitanat ($BaTiO_3$, BTO) basierenden Pockels-Modulatoren in eine Siliziumphotonik Plattform entwickelt. Zu diesem Zweck wurden drei grosse Herausforderungen für integrierte, BTO-basierte, optische Bauteile gelöst: i) Die Reduktion optischer Verluste in Wellenleitern, ii) der Nachweis des Pockels-Effekts in, auf Silizium integrierten, BTO-basierten Wellenleitern und iii) die monolithische Integration mit Silizium-PIC.

In vorangehenden wissenschaftlichen Arbeiten an BTO-basierten Modulatoren, die auf eine Silizium Plattform integriert wurden, wurden unerwartet hohe optische Verluste berichtet. In dieser Doktorarbeit wurde der Ursprung dieser Verluste als eine chemische Reaktion innerhalb der Materialien während der Herstellung der Bauteile identifiziert. Diese neuen Erkenntnisse erlauben eine Anpassung des Fertigungsverfahrens, das zu BTO-basierten Wellenleitern integriert auf Silizium Substraten mit geringen optischen Verlusten führt.

Basierend auf diesem Verfahren für Wellenleiter mit geringen optischen Verlusten und unter Berücksichtigung von Integrationsaspekten wurde ein neuer Wellenleiterquerschnitt entwickelt um die elektrooptischen Eigenschaften von BTO Dünnschichten zu untersuchen. Zum ersten Mal wurde ein eindeutiger Beweis des Pockels-Effekts in BTO-basierten, optischen Bauteilen in Form eines anisotropen elektrooptischen Effekts, einer grossen elektrooptischen Bandbreite von 30 GHz und einer Hysterese des elektrooptischen Effekts, bedingt durch das Umklappen ferroelektrischer Domänen in BTO, gezeigt. Die gemessenen Pockels-Koeffizenten in BTO Dünnschichten sind vergleichbar zu denen im BTO Volumenkristall. Bemerkenswert ist der Wert des r_{42} Koeffizienten von 923 pm/V ($\lambda = 1,55$ µm), der den grössten, jemals in einem elektrooptischen Bauteil gemessenen Pockels-Koeffizenten darstellt.

Nach der Untersuchung grundlegender Aspekte von BTO als Material in hybriden BTO-Silizium Wellenleitern wurde ein Verfahren für die Integration von BTO auf Silizium-basierter integrierter optischer Schaltkreise (PIC) entwickelt: BTO-basierte Modulatoren wurden während der sogenannten «Back-End-of-Line» (BEOL) Fertigungsphase von PIC-Substraten unter Ausnutzung molekularer Waferbonding-Technologie hergestellt. Die integrierten, BTO-basierten Modulatoren zeigen hervorragende Leistungskennzahlen und sind ein Meilenstein bei der PIC-kompatiblen Integration von Pockels-Modulatoren.

Die BTO-basierte, optische Technologie erweitert die Siliziumphotonik mit grundlegenden und neuen physikalischen Eigenschaften. Aus diesem Grund wurde die Plattform für neue Anwendungen und Bauteile über herkömmliche elektrooptische Modulatoren hinaus untersucht. Zunächst wurden plasmonische BTO-Modulatoren untersucht. Zum einen wurde dazu ein neuartiger Herstellungsprozess entwickelt um plasmonische, BTO-basierte Modulatoren mit Abmessungen im Nanometerbereich herzustellen. Die plasmonischen Modulatoren zeigen eine exzellente thermische Stabilität und ein hervorragendes Verhalten bei der Übertragung von Daten mit extrem hohen Datenraten von 72 und 116 Gbps. Zum anderen wurde das Potenzial der BTO-Technologie für kryogene optische Anwendungen untersucht. Zum ersten Mal überhaupt wurden die strukturellen und elektrooptischen Eigenschaften von auf Silizium integrierte BTO Dünnschichten bei Tieftemperaturen untersucht. Die Resultate zeigen Unterschiede bei den kristallinen Phasenübergängen zwischen Dünnschichten und Volumenkristallen. Die Existenz eines grossen Pockels-Effekts bei 4 K und die Möglichkeit, diesen Effekt für praktische Anwendungen auszunutzen, wurden ebenfalls nachgewiesen. Insbesondere wurden die kryogenen Bauteile für eine Datenübertragung mit einer Rate 20 Gbps bei 4 K verwendet, was einen neuen Rekord in diesem Temperaturbereich darstellt.

Die in dieser Arbeit entwickelte BTO-Technologie bietet einen Weg für die Integration von Hochleistungs-Pockels-Modulatoren auf Silizium-basierten, integrierten optischen Schaltkreisen. Um dieses Ziel zu erreichen wurden grundlegende Aspekte von auf Silizium integrierten BTO Dünnschichten erforscht und ein neues Verständnis der optischen und elektrooptischen Eigenschaften des Materialsystems erlangt. Die Demonstration effizienter elektrooptischer Modulatoren für kryogene optische Anwendungen beseitigt eine der grössten Hürden für die Entwicklung einer integrierten, optischen Quantentechnologie.

CONTENTS

List of Figures xi
Acronyms xv
1 INTRODUCTION 1
1.1 Motivation . . . 1
1.2 General background . . . 2
1.2.1 Silicon photonics transceivers . . . 2
1.2.2 Silicon electro-optic modulators . . . 5
1.2.3 Pockels modulators . . . 7
1.2.4 Pockels materials . . . 9
1.2.5 Barium titanate . . . 10
1.2.6 Monolithic integration . . . 12
1.3 Challenges and goals . . . 14
1.4 Structure of this thesis . . . 14
2 BARIUM TITANATE 17
2.1 Fundamentals of barium titanate . . . 17
2.2 $BaTiO_3$ deposition . . . 17
2.3 Second harmonic generation in BTO . . . 21
2.4 Conclusion . . . 26
3 OPTICAL LOSSES IN BTO-SI DEVICES 29
3.1 Introduction . . . 29
3.2 Origin of the losses . . . 30
3.3 Reducing propagation losses . . . 33
3.4 Conclusion . . . 34
4 THE POCKELS EFFECT IN BTO-SI DEVICES 35
4.1 Introduction . . . 35
4.2 Devices to characterize EO response . . . 38
4.3 Device fabrication . . . 39
4.4 Confirmation of the Pockels effect . . . 41
4.5 High-speed modulation using Pockels effect . . . 42
4.6 Conclusions . . . 43
5 A MONOLITHICALLY INTEGRATED POCKELS MODULATOR 45
5.1 Introduction . . . 45
5.2 Integration . . . 46
5.3 Modulator characterization . . . 47

5.4 Conclusion 49
6 PLASMONIC BTO MODULATORS 51
6.1 Introduction 51
6.2 Fabrication 53
6.3 Pockels effect and stability 55
6.4 Bandwidth and data modulation 58
6.5 Conclusion 60
7 BTO FOR CRYOGENIC PHOTONIC CIRCUITS 61
7.1 Introduction 61
7.2 Low temperature electro-optic characterization 63
7.3 Device demonstrations 65
7.4 Conclusions 66
8 CONCLUSION AND OUTLOOK 67
A LOW-LOSS $BaTiO_3$-SI WAVEGUIDES FOR NONLINEAR INTEGRATED PHOTONICS 69
B LARGE POCKELS EFFECT IN MICRO- AND NANOSTRUCTURED BARIUM TITANATE INTEGRATED ON SILICON 83
C A $BaTiO_3$-BASED ELECTRO-OPTIC POCKELS MODULATOR MONOLITHICALLY INTEGRATED ON AN ADVANCED SILICON PHOTONICS PLATFORM 101
D INTEGRATED FERROELECTRIC PLASMONIC OPTICAL MODULATOR 113
E AN INTEGRATED CRYOGENIC OPTICAL MODULATOR 119

BIBLIOGRAPHY 139
ACKNOWLEDGMENTS 159
CONTRIBUTIONS TO THIS THESIS 161
PUBLICATIONS 163

LIST OF FIGURES

Figure 1.1 Overview of data center structure. 2
Figure 1.2 Silicon photonics in optical transceivers. 3
Figure 1.3 Transceiver and modulator evolution. 5
Figure 1.4 Data modulation formats. 6
Figure 1.5 Operation principle of a silicon electro-optic modulator. 7
Figure 1.6 Comparison of Pockels coefficients. 10
Figure 1.7 Cross-sections of reported BTO waveguides 12
Figure 1.8 Wafer bonding schematic. 13
Figure 2.1 reflection high-energy electron diffraction (RHEED) diffractograms of epitaxial STO and BTO 18
Figure 2.2 high-resolution scanning transmission electron microscopy (HRSTEM) of Si-STO and Si-STO-BTO. . . . 19
Figure 2.3 BTO domain structure. 20
Figure 2.4 X-ray diffraction (XRD) of BTO thin film. 20
Figure 2.5 BTO domain poling. 21
Figure 2.6 second harmonic generation (SHG) experimental setup 23
Figure 2.7 SHG in BTO. 27
Figure 3.1 Waveguides for loss measurements. 30
Figure 3.2 Propagation losses at different stages during processing. 31
Figure 3.3 XPS characterization of loss origin. 33
Figure 3.4 Reduction of propagation losses in BTO waveguides. 33
Figure 4.1 Relation between hysteresis and Pockels response. . . 37
Figure 4.2 Racetrack resonator schematic. 39
Figure 4.3 BTO device process flow. 40
Figure 4.4 Pockels effect in BTO on silicon. 42
Figure 4.5 Data transmission using BTO ring modulators. 42
Figure 5.1 Concept for BTO monolithic integration. 47
Figure 5.2 Monolithically integrated BTO modulator. 48
Figure 5.3 Data transmission using monolithic BTO Mach-Zehnder modulator. 49
Figure 6.1 Comparison of photonic and plasmonic waveguides. 52
Figure 6.2 Plasmonic modulator process flow. 54
Figure 6.3 Layout of BTO plasmonic devices. 55

Figure 6.4 Sideband modulation in BTO plasmonic modulator. . 56
Figure 6.5 Thermal stability of BTO plasmonic modulator. . . . 56
Figure 6.6 Long-term stability of BTO plasmonic modulator. . . 57
Figure 6.7 EO bandwidth of plasmonic BTO modulators. 58
Figure 6.8 Piezoelectric effect in plasmonic modulators. 58
Figure 6.9 72 and 116 Gbps data transmission using plasmonic BTO modulator. 59
Figure 7.1 Schematic over applications for cryogenic PICs. . . . 62
Figure 7.2 Temperature dependence of the Pockels effect in BTO. 64
Figure 7.3 Demonstration of high-speed data modulation with BTO-based devices at 4 K. 65
Figure A.1 Waveguide cross-sections for BTO loss evaluation. . . 72
Figure A.2 STEM cross-section of BTO slot-waveguide. 73
Figure A.3 Propagation losses at different stages during processing. 75
Figure A.4 XPS characterization of loss origin. 79
Figure A.5 Reduction of propagation losses in BTO waveguides. 80
Figure A.6 Comparison of ring resonator spectra before and after annealing. 81
Figure A.7 Comparison of reported propagation losses in BTO waveguides. 81
Figure B.1 Fabrication process and structural characterization for a hybrid crystalline-amorphous BTO-SiO_2 heterostructure. 87
Figure B.2 Layout of the photonic and plasmonic devices. 89
Figure B.3 EO response proving the presence of the Pockels effect. 91
Figure B.4 Data transmission in a photonic and plasmonic modulator. 94
Figure C.1 Concept for BTO monolithic integration. 104
Figure C.2 200 mm transfer of thin-film BTO 105
Figure C.3 Process flow for monolithic BTO integration. 106
Figure C.4 STEM cross-section of monolithic BTO integration. . 107
Figure C.5 FEOL characterization after BTO integration. 107
Figure C.6 DC characteristics of monolithic BTO modulator. . . . 109
Figure C.7 Static power consumption of BTO modulator. 110
Figure C.8 *S*-parameter measurements of monolithic BTO modulator. 111
Figure C.9 Data transmission using monolithic BTO Mach-Zehnder modulator. 111

Figure D.1 BTO plasmonic modulator. 115
Figure D.2 Thermal and long-term stability of BTO plasmonic modulator. 116
Figure D.3 Schematic of data transmission experimental setup. . 117
Figure E.1 $BaTiO_3$ electro-optic device concept. 122
Figure E.2 Electro-optic and electrical response of $BaTiO_3$-based optical switches at 4 K. 123
Figure E.3 Temperature dependence of the Pockels effect in $BaTiO_3$. 125
Figure E.4 Demonstration of low-power switching and high-speed data modulation with $BaTiO_3$-based devices at 4 K. 126
Figure E.5 Cut-back loss-measurements of a SiN and SiN-$BaTiO_3$ and Si-$BaTiO_3$ waveguides at 300 K and 4 K. 130
Figure E.6 Fitted NLO hysteresis measured in a $BaTiO_3$-SiN device at 300 K. 131
Figure E.7 Leakage current through $BaTiO_3$ at various temperatures. 132
Figure E.8 Change in polarisation and resulting electrical current in $BaTiO_3$ capacitors. 133
Figure E.9 Induced resonance shift at various temperatures from 10 to 100 K. 134
Figure E.10 Temperature dependence of $BaTiO_3$ permittivity at different electric-field strengths. 135
Figure E.11 *S*-parameter measurements of the transmission through the cryogenic probe station. 136
Figure E.12 Characterisation of modulation voltage in cryogenic probe station. 137

ACRONYMS

ALD	atomic layer deposition
BEOL	back-end-of-line
BER	bit-error ratio
BTO	barium titanate
CMOS	complementary metal-oxide-semiconductor
CTR	crystal truncation rod
CVD	chemical vapor deposition
DSP	digital signal processing
EBL	electron beam lithography
EO	electro-optic
EOM	electro-optic modulator
FEC	forward error correction
FEOL	front-end-of-line
HRSTEM	high-resolution scanning transmission electron microscopy
HSQ	hydrogen silsesquioxane
IBE	ion beam etching
ICP-RIE	inductively coupled plasma reactive ion etching
ILD	inter layer dielectric

IP	in-plane
LN	lithium niobate
MBE	molecular beam epitaxy
MIM	metal-insulator-metal
ML	monolayer
MZI	Mach-Zehnder interferometer
OOK	on-off keying
OOP	out-of-plane
PAM	pulse-amplitude modulation
PDM	polarization division multiplexing
PECVD	plasma-enhanced chemical vapor deposition
PIC	photonic integrated circuit
PLD	pulsed laser deposition
PRBS	pseudo-random bit sequence
QAM	quadrature amplitude modulation
RF	radio frequency
RHEED	reflection high-energy electron diffraction
SDM	space division multiplexing
SHG	second harmonic generation
SISCAP	semiconductor-insulator-semiconductor capacitor
SOI	silicon-on-insulator
SPP	surface plasmon polariton
STEM	scanning transmission electron microscopy

TE	transverse electric
TM	transverse magnetic
UHV	ultra-high vacuum
WDM	wavelength division multiplexing
XPS	X-ray photoelectron spectroscopy
XRD	X-ray diffraction
ZB	zettabyte

1

INTRODUCTION

1.1 MOTIVATION

We are living in the zettabyte (ZB) era. Driven by the rise of cloud computing, hyperscale data centers have grown to dominate global data traffic. By the year 2021, global data center traffic is predicted to reach more than 20 ZB annually, up from 6.8 ZB in 2016 [1]. The majority of this traffic ($\sim$15 ZB) occurs within data centers. As a consequence of this enormous amount of data moving within data centers, new technologies have emerged to handle the increased traffic. The development of novel optical transceiver (transmitter-receiver) technology has allowed optical communication to replace electrical communication down very short distances (<1 m). In order to make the transceiver smaller and cheaper, the industry has turned to the most advanced large-scale technology platform available: silicon. By leveraging the maturity of silicon CMOS technology, optical transceivers have been miniaturized and made cheap and efficient. However, as the bandwidth requirements continue to grow, further innovation of the silicon photonics platform is needed.

An optical transceiver consists of many components, but perhaps the most crucial ones are the light source, the EOM, and the photo detector (Figure 1.1). The light source in Si photonics is a continuous wave laser, which provides the optical carrier for the link. The EOM takes an electrical input signal and encodes it on the optical carrier. At the receiver the optical signal is converted back to the electrical domain by a photo detector. Out of these three components, the one which is currently limiting the bandwidth of silicon photonic transceivers is the modulator. For this reason, the improvement of silicon EOMs is pursued by many research groups and companies around the world.

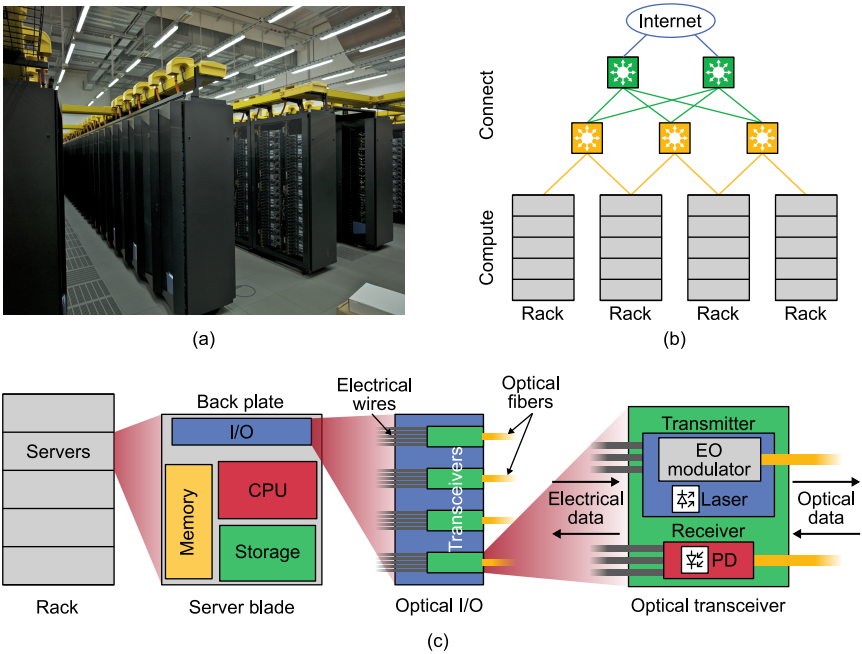

FIGURE 1.1: (a) Photo showing server racks in a data center for high performance computing (credit IBM Research). (b) Schematic drawing of a typical data center architecture showing the connections from server racks through the interconnect levels to the internet. (b) Schematic illustrations of the a server rack down to the electro-optic transceivers.

1.2 GENERAL BACKGROUND

In the following sections silicon photonics will be introduced in more detail, followed by a discussion on the state-of-the-art of silicon modulators and their limitations. Finally a way to overcome the limitations of the current technology by integration of Pockels modulators will be discussed.

1.2.1 *Silicon photonics transceivers*

Silicon as a platform for PICs was proposed as a concept more than three decades ago [2, 3], but it is only recently that the technology has become mature enough for large scale commercialization. The main application of silicon photonics is in high-speed optical transceivers (Figure 1.2), where

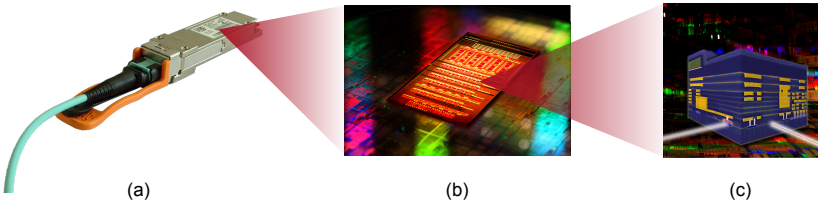

FIGURE 1.2: Silicon photonics in optical transceivers. (a) A pluggable optical transceiver module used in data centers. (b) Silicon photonic chip performing the main functions of the transceiver (credit IBM Research). (c) Cross-section of silicon photonics chip showing multiple metal levels and silicon waveguides in the front-end-of-line (FEOL) (credit IBM Research).

it is becoming the leading technology for intra-data center interconnects. Perhaps the main advantage of silicon-based transceivers over other technologies, such as InP, is the possibility to leverage existing technology infrastructure in the CMOS industry, which enables low cost, high yield, and large volume production. Silicon photonics offers most of the required components of an optical link, such as modulators, detectors, and wavelength filters, highly integrated on a single chip. The only component that needs to be heterogeneously integrated or co-packaged is the light source. Silicon photonics also enables the miniaturization of optical waveguides (Figure 1.2). Because of the large refractive index contrast between the silicon waveguide core and the silicon oxide cladding surrounding the waveguides fabricated from silicon-on-insulator (SOI) wafers, silicon photonics can be made extremely compact. Silicon waveguides typically have a cross-section of $\sim$0.1 μm^2, two orders of magnitude smaller than the cross-section of an optical fiber of $\sim$25 μm^2.

The data rate of a transceiver is specified as the net rate of the bits leaving or arriving through the optical fiber(s). This data rate can be distributed across several lanes in the form of multiple fibers (space division multiplexing (SDM)), multiple wavelengths in a single fiber (wavelength division multiplexing (WDM)), or even two polarizations at the same wavelength in a single fiber (polarization division multiplexing (PDM)). On each lane data is transmitted or received at a lower bit rate, the sum of which is the transceiver bit rate. It is also common to use higher-order modulation formats to transmit more than one bit at each symbol, or pulse, leading to a higher bit rate than symbol rate (Baud, Bd).

While state-of-the-art silicon photonic transceivers are capable of transmission of data at rates up to 400 Gbps, the symbol rate is limited to 50 GBd because of the limited bandwidth of silicon EOMs (Figure 1.3). Instead, the high data rate is achieved through the use of WDM and the use of higher order modulation formats. WDM utilizes multiple wavelengths in parallel to increase the data rate transmitted through a single fiber. Higher modulation formats such as pulse-amplitude modulation (PAM) increase the data rate by encoding multiple bits per symbol (Figure 1.4a), this is achieved by using more than two pulse levels. The number of bits that are encoded per symbol, $\#_{\text{bits}}$, is determined by number of pulse levels, n:

$$\#_{\text{bits}} = \log_2(n) \tag{1.1}$$

As an example, the commonly used format PAM4 uses four amplitude levels to transmit 2 bits per symbol.

The measures required to scale the transceiver data rate (Figure 1.3) significantly increases the complexity, power consumption and cost of of transceivers. Using higher symbol rates and a simple on-off keying (OOK) modulation format, where only one bit is transmitted per symbol (Figure 1.4a), would result in more power efficient transceivers. A higher symbol rate would also simplify the transition to future transceiver standards with even higher data rates (800 Gbps followed by 1.6 Tbps).

Beyond data center interconnects, silicon photonics is also being pursued for coherent optical transceivers. The use of coherent detection allows for high-data rate transmission also over larger distances (>2 km) by enabling the use of more complex modulation formats where information is encoded in both phase and amplitude, such as quadrature amplitude modulation (QAM) (Figure 1.4b) where both multiple amplitude and phase levels are used to increase the bit rate. For such transceivers, linear modulation of the phase with the applied voltage to the modulator is critical and it is desirable to have modulators capable of modulating the phase only. Silicon modulators have non-ideal linearity and pure phase modulation is impossible. Therefore additional digital signal processing (DSP) is required to compensate for the modulator limitations, which increases the power consumption of the transceiver. The limitations of silicon modulators are intrinsic to the operating mechanism of the devices.

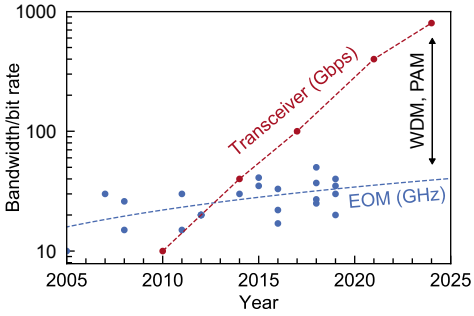

FIGURE 1.3: Evolution of transceiver data rate and silicon modulator bandwidth over time [4–26]. The modulator bandwidth has increased linearly over time, whereas the transceiver data rate is growing exponentially.

1.2.2 *Silicon electro-optic modulators*

To make an EOM, one needs a mechanism to tune the optical transmission, the complex refractive index, of a waveguide by application of an electrical signal. In silicon, modulation of the refractive index achieved through free-carrier modulation, also called the plasma dispersion effect [27]. To efficiently exploit this effect in a waveguide, a pn-junction is formed in the waveguide by doping implantation (Figure 1.5a). When applying a voltage across the junction, the carrier concentration changes resulting in a modulation of the refractive index. Modulating the refractive index in a section of waveguide can be used to induce a phase shift of the transmitted light. Because the index change arises from a change in free-carrier concentration, not only the real part but also the imaginary part of the refractive index changes. This is an undesired side-effect causing simultaneous modulation of both phase and amplitude. To be able to use a phase shifter for intensity modulation, it is embedded in Mach-Zehnder interferometer (Mach-Zehnder interferometer (MZI), Figure 1.5b). Incoming laser light is split equally in two paths (arms), and then recombined at the output. By modulating the phase in one arm of the MZI, the output intensity is modulated through constructive or destructive interference when the light is recombined at the output.

To fully switch between "on" and "off" states, a phase shift of π needs to be induced between the two arms of the MZI. The voltage needed for a π phase shift, V_π, is the basis for one of the most important figures of

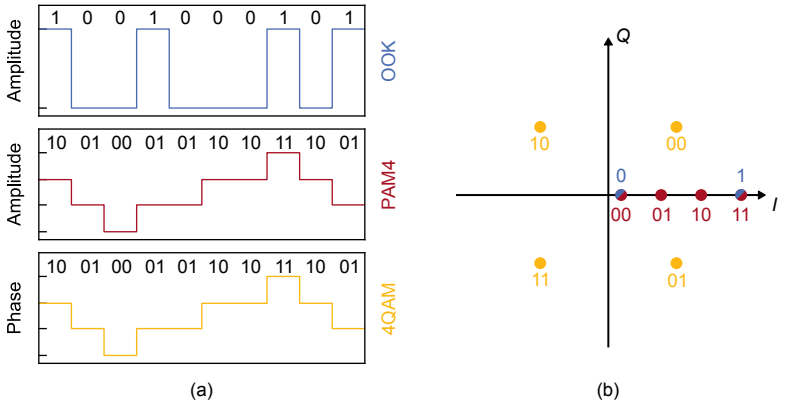

FIGURE 1.4: (a) Symbol patterns for data transmission using different modulation formats. OOK modulation (top) sends one bit per symbol whereas PAM4 (middle) uses four amplitude levels to transmit 2 bits per symbol resulting in a doubling of the data rate at the same symbol rate. 4QAM (bottom) encodes data in the phase information. (b) Constellation diagrams of OOK, PAM4 and 4QAM showing the distribution of the symbols (poles) in the complex plane. The number of poles determines the number of bits that are transmitted per symbol (eq. 1.1). In formats using amplitude modulation (OOK and PAM) all poles are on the intensity, I, axis, whereas for QAM the poles are distributed in the IQ plane.

merit to compare electro-optic modulators: the voltage-length product, $V_\pi L$. $V_\pi L$ is the product of V_π and the phase shifter length, L, most often given in units of V·cm. In silicon EOMs optimized for high bandwidth, $V_\pi L$ is typically around 2-3 V·cm [15, 28, 29]. Since driving voltages are limited to a few volts, the phase shifter in a silicon modulator needs to be several millimeters long. The size of the modulator does not only have an impact on the footprint, which is one important aspect, but also has large implications for high-speed operation.

The modulating radio frequency (RF) signal is transmitted through the electrodes and then terminated over a resistor matched to the driver impedance. Because the signal travels through the electrodes, the propagation constant of the RF mode must be matched to that of the optical mode. This requires careful engineering to achieve dispersion-free matching in order to reach a high electro-optic bandwidth. The impact of any mismatch increases with the length of the modulator. It has been possible to achieve a bandwidth of 40 GHz [15] by optimizing every aspect of the device design. It has

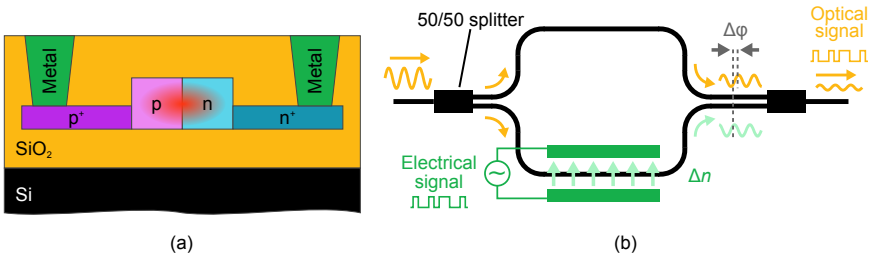

FIGURE 1.5: Operation principle of a silicon electro-optic modulator. (a) The basic structure of a phase shifter based on the plasma-dispersion effect. The guided optical mode is shown schematically in the waveguide core. By applying a voltage across the pn-junction, the refractive index changes resulting in a phase shift of the propagating optical mode. (b) A phase shifter embedded in a Mach-Zehnder interferometer. Modulation of the phase in one arm of the interferometer results in intensity modulation at the output.

been extended further to 50 GHz only though extraordinary measures such as substrate under-etching of the device [20]. The use of hybrid devices combing silicon with III-V materials has also been investigated in order to make more efficient plasma-dispersion modulators resulting in highly efficient modulators, but with a bandwidth limited to a few GHz [30, 31].

It therefore seems that silicon EOMs based on the plasma-dispersion effect are approaching the ultimate limit in terms of bandwidth, which means that also the limit in symbol rate of silicon photonic transceivers. To keep increasing the bandwidth, new types of EOMs need to be implemented in the silicon photonics platform, based on a different modulation mechanism. The answer to what physical effect can be exploited can perhaps be found by looking at the most mature optical communication technology: long-haul telecommunications.

1.2.3 *Pockels modulators*

The EOMs used in long-distance optical (telecom) links are made from lithium niobate ($LiNbO_3$, LN) and are operating based on the Pockels effect. The Pockels effect is a second-order ($\chi^{(2)}$) nonlinear effect which describes a linear change in the refractive index induced by the presence of a quasi-static (low frequency compared to optical frequencies) electric field. The magnitude of the induced refractive index change is determined by the

Pockels coefficients of the material. In reduced notation the refractive index changes according to:

$$\begin{pmatrix} \Delta(1/n^2)_1 \\ \Delta(1/n^2)_2 \\ \Delta(1/n^2)_3 \\ \Delta(1/n^2)_4 \\ \Delta(1/n^2)_5 \\ \Delta(1/n^2)_6 \end{pmatrix} = \begin{pmatrix} r_{11} & r_{12} & r_{13} \\ r_{21} & r_{22} & r_{23} \\ r_{31} & r_{32} & r_{33} \\ r_{41} & r_{42} & r_{43} \\ r_{51} & r_{52} & r_{53} \\ r_{61} & r_{62} & r_{63} \end{pmatrix} \begin{pmatrix} E_x \\ E_y \\ E_z \end{pmatrix} \tag{1.2}$$

where n is the real-part of the refractive index, E is the applied electric field, and r_{ij} are the Pockels coefficients. Which Pockels coefficients are non-zero is a consequence of the structural symmetry of the material, and the magnitude of those coefficients is material-dependent. In the case of a centrosymmetric material (such as silicon), all coefficients are zero, meaning such materials do not posses any second-order nonlinearity. A key aspect of the Pockels effect is the fact that only the real-part of the refractive index is affected, making it possible to modulate phase without changing absorption, something which is impossible in plasma-dispersion modulators.

The efficiency of a Pockels modulator is determined by the change of the effective index of the optical mode which is dependent on several factors, one of which is the magnitude of the Pockels coefficients. The Pockels coefficients determine the change of the refractive index of the material, but the tensorial nature means that the index change perceived by the optical mode is dependent on the crystal orientation, the propagation direction and the orientation of both the optical and static electric fields. These geometric factors are often combined and expressed as an effective Pockels coefficient, r_{eff}, which is valid for a specific configuration. The change in the effective index of the optical mode is proportional to the change of the material refractive index, Δn_{m}, and the fraction of the optical power that is confined in the material (the optical overlap, Γ_{m}):

$$\Delta n_{\text{eff}} \propto \Delta n_{\text{m}} \times \Gamma_{\text{m}} \tag{1.3}$$

All of these factors, combined with the electrode geometry, determines the $V_\pi L$ of a Pockels modulator. This value also depends on the operating

wavelength, as the magnitude of the Pockels coefficients is wavelength dependent. EOMs typically operate at wavelengths in the range from 1250 to 1625 nm. For this reason any values of Pockels coefficients discussed here are for this wavelength window.

In the case of lithium niobate (LN) modulators, the waveguides are formed with a small index contrast in bulk crystals, and the Pockels coefficients are relatively small ($\sim$30 pm/V) which means that the phase shifters need to be $\sim$5 cm long [32]. Because of the long phase sections, traveling wave electrodes are a necessity to increase the RF bandwidth, with typical bandwidths being $\sim$35 GHz. Despite the limited bandwidth (and with it symbol rate), LN modulators can be used to transmit more than 200 Gbps on a single carrier. This is largely thanks to the pure phase modulation and linearity of the modulation which enables the encoding of information in both amplitude and phase to send multiple bits per symbol in coherent transmission systems.

If Pockels modulators could be made more efficient to reduce the size and enable higher bandwidths their potential in a silicon photonics platform is immense. However, as the Pockels effect is not present in silicon due it to having a centrosymmetric structure, heterogeneous integration of new materials is needed to bring Pockels modulators to the silicon platform.

1.2.4 *Pockels materials*

There are many aspects to consider when looking to integrate a material with the Pockels effect in a silicon platform. The first question is which material is the best candidate. To make efficient modulators, the material should have a large Pockels coefficient, but that alone is not sufficient. The material should be transparent in the optical communication wavelength window (1250-1625 nm) to avoid absorption losses. It should be scalable to large substrates to benefit from advanced silicon process technology, and it should be compatible with standard processing and packaging technologies to not degrade during fabrication. There are many materials which exhibit the Pockels effect, but the values of the coefficients of span several orders of magnitude. Figure 1.6 provides an overview of the Pockels coefficients of the most technologically relevant Pockels materials. While LN has been used with great success for bulk modulators, the relatively low Pockels coefficient makes it difficult to scale the device footprint. Additionally, LN wafer diameters are limited to 6" or smaller, while silicon photonic plat-

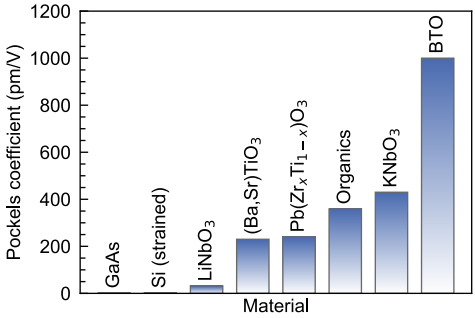

FIGURE 1.6: Comparison of Pockels coefficient in some technologically relevant materials. The numbers correspond to the largest values reported for thin film or bulk material at wavelengths between 1 and 1.5 μm. [33, 34, 37–43]

forms are generally produced on 200 or 300 mm substrates. An interesting alternative to LN are electro-optic organic materials, where Pockels coefficients of almost 400 pm/V have been reported [33]. However, the active material is absorbing which leads to increases losses. Organic materials also suffer from poor thermal stability and photo-chemical degradation, which creates additional hurdles for fabrication and packaging. It is worth noting that the Pockels effect is present in compound semiconductors such as GaAs, but with a very small magnitude (∼1 pm/V). There have also been reports of strain-induced Pockels effect in silicon with a small magnitude (2 pm/V) [34, 35], however the true origin of the observed Pockels effect has been questioned [36]. A class of materials which offer chemical and thermal stability as well as large Pockels coefficient are ferroelectric perovskites such as $Pb(Zr_xTi_{1-x})O_3$ (PZT), $KNbO_3$, $(Ba,Sr)TiO_3$ (BSTO), and $BaTiO_3$ (BTO) [37]. Among the perovskites, PZT, BSTO, and $KNbO_3$ show relatively large Pockels coefficients (200-400 pm/V) compared to LN, but are dwarfed by the Pockels coefficients of barium titanate (BTO), which are as high as 1′000 pm/V [38]. As will be discussed below, BTO is an excellent candidate for Pockels modulators, also from an integration and scaling perspective.

1.2.5 *Barium titanate*

BTO is a well-studied ferro- and piezoelectric material, but has only recently been explored for integrated electro-optic applications. Bulk BTO has one of the largest known Pockels coefficients, but that is not the only property

which makes it suitable for use in EOMs. Another highly attractive aspect of BTO is that it high quality crystalline thin films can be deposited by epitaxy on silicon substrates [44] (a more detailed discussion can be found in Chapter 2). This enables the use of low-cost, large-diameter silicon substrates, a key aspect for a competitive scalable technology. However, the first demonstrations of BTO-based EOMs did not use silicon substrates, but was based on BTO epitaxially deposited on MgO substrates [45, 46]. More recently, there have been reports of devices based on BTO deposited on silicon substrates [47–49]. In both cases, the BTO waveguides have not been formed by patterning the BTO itself, as this is a challenging task, and can cause damage to the material. Instead, the devices are based on alternative waveguide geometries.

The BTO-MgO devices are based on a strip-loaded waveguide geometry, where the optical mode is guided by a strip of silicon nitride (SiN, Si_xN_y) fabricated on top of a blanket BTO layer (Figure 1.7a). Since the BTO has a higher refractive index ($n = 2.3$) than MgO ($n = 1.7$), the optical mode is vertically confined in the BTO layer. The SiN-strip on top of the BTO ensures guiding of the mode also in the horizontal direction. The use of a relatively thick BTO layer (500-600 nm) results in a large optical overlap, Γ_{BTO}, of $\sim$60 %. As discussed above, the optical overlap is critical, as the modulation efficiency is directly proportional to Γ_{BTO}. Lateral electrodes situated on top of the BTO are used to apply an in-plane electric field for modulation of the BTO refractive index through the Pockels effect. BTO-MgO is an attractive research platform as the BTO deposition process is made simpler by having a crystalline oxide substrate compared to deposition on silicon substrates. However, MgO wafers are expensive compared to silicon, and are limited to 2″ diameter, which is why BTO-Si is required for large-scale integration with silicon photonics.

Devices based on BTO-Si use a different waveguide geometry. First, the BTO is deposited on an SOI substrate to ensure vertical confinement of the optical mode. By the addition of a silicon strip on top, the BTO layer is sandwiched between the two silicon layers forming a slot-waveguide structure (Figure 1.7b). The slot structure allows the formation of a waveguide without the need for patterning the BTO. The combination of the slot-waveguide structure and the use of thinner BTO layers (50-80 nm) results in a lower optical overlap of $\sim$20 % for the transverse electric (TE) mode [48, 49].

Using BTO-Si devices, electro-optic bandwidth in the GHz range as well as low-power tuning have been demonstrated. However, the devices suffer

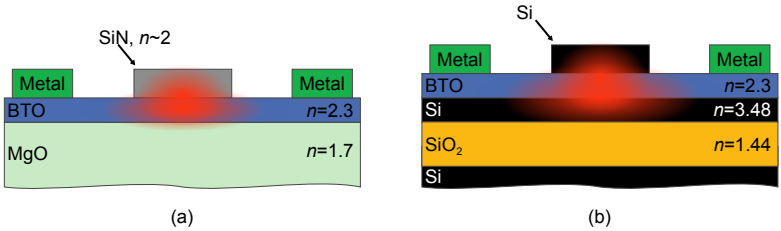

FIGURE 1.7: Waveguide cross-sections of reported (a) BTO-MgO and (b) BTO-Si devices. The fundamental waveguide TE mode is illustrated schematically in red.

from large propagation losses in the waveguides. The losses are >40 dB/cm, which are significantly higher than the 1-3 dB/cm in state-of-the-art silicon photonic platforms [50], and 4 dB/cm in BTO-MgO waveguides [45]. The propagation losses need to be reduced for BTO-Si to become a useful technology. Additionally, the reported Pockels coefficients range from 150-250 pm/V [48, 49, 51], which is significantly lower than the 800 pm/V of bulk BTO. There is also a lack of definite proof that the Pockels effect is really the source of the phase shift in the devices. Some of the reported results, such as hysteresis curves which do not match the expected behavior of a ferroelectric material like BTO [49], are inconsistent with the Pockels effect, and critical properties of the Pockels effect remain to be demonstrated (see Chapter 4 for further discussion). There is therefore a need to resolve these challenges of BTO-Si devices in order to make it a viable technology for EOMs in silicon photonic transceivers.

1.2.6 *Monolithic integration*

In addition to the challenges on the material level, the large-scale integration of BTO with silicon photonics has yet to be addressed. BTO can be deposited on silicon substrates, which allows for cheap, large diameter wafers. However, it does not necessarily provide a direct path for integration with silicon photonics on the same substrate – monolithic integration. To combine BTO modulators with standard silicon photonic devices, the BTO needs to be integrated after the fabrication of silicon waveguides, photo detectors, and other FEOL components. At that stage, the crystalline silicon substrate has been processed and cladded with an inter layer dielectric (ILD). This means that there is no planar silicon substrate available for epitaxial growth. Even if direct growth would have been possible, the typical

deposition temperature of BTO is ∼600°C, which is above the temperature limit, or thermal budget, of a BEOL process. There is therefore a need to find an alternative path to bring BTO into a silicon photonics platform without compromising the PIC performance.

Recently, a similar challenge has been tackled in the field of CMOS electronics. The integration of III-V materials, such as InGaAs, together with silicon has the potential to enhance the performance of CMOS circuits, however the thermal budgets in processing, as well as challenges in direct epitaxy of InGaAs on silicon, pose a similar challenge to that of BTO integration. A recently demonstrated solution uses molecular wafer bonding to transfer an InGaAs thin film onto a pre-processed wafer with silicon transistors [52]. The wafer bonding process uses thin adhesion layers which fuse resulting

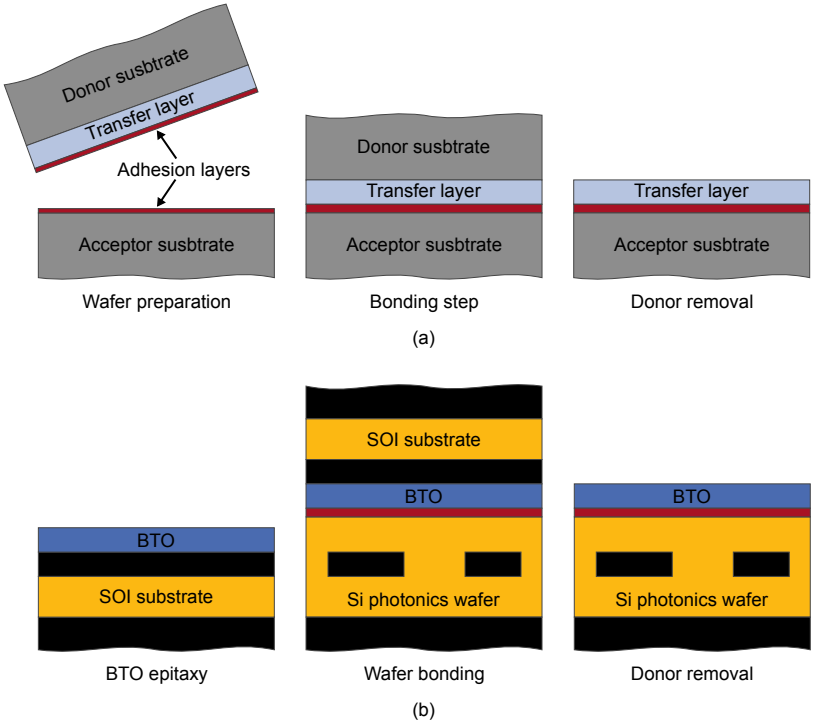

FIGURE 1.8: (a) Schematic of thin film transfer through direct wafer bonding. (b) Schematic of how a BTO layer can be transferred to a silicon photonics wafer through a low-temperature wafer bonding process.

in a bonding of two wafers (Figure 1.8a). After the bonding, the donor wafer can be removed by chemical and/or mechanical means to leave only a thin layer transferred onto the acceptor wafer. Wafer bonding can be optimized to allow for a low-temperature process, making it compatible with thermal budget limitations in the case of a pre-processed acceptor wafer [53, 54]. Using such a process, BTO could be deposited on an unprocessed silicon substrate and then integrated through wafer bonding on a pre-processed silicon photonics wafer (Figure 1.8b). This integration approach will be discussed in further detail in Chapter 5.

1.3 CHALLENGES AND GOALS

While BTO-on-Si technology holds great promise for use in silicon photonic transceivers, there are significant challenges to overcome before it can be considered a viable technology. On a fundamental level, first the issue of propagation losses must be solved, and second, large Pockels coefficients demonstrated. Without these aspects, BTO cannot compete with alternative technologies. Resolving these issues to show that BTO can indeed deliver the expected performance is the first goal of this thesis. Having overcome the fundamental challenges of the material itself, the third aim is to prove that BTO devices are compatible with silicon photonics, by demonstrating a monolithically integrated BTO modulator on an advanced silicon platform. The first part of the thesis tackles these three challenges in turn.

The second part of this thesis aims to demonstrate the potential of the BTO platform to bring silicon photonics into entirely new territory, beyond conventional devices and applications. While the discussion so far has been focused on photonic EOMs for optical transceivers, the development of a novel technology platform based on BTO has much more far reaching implications. BTO brings fundamentally new properties and functions to silicon photonics, which can be exploited for novel device architectures such as plasmonic EOMs. It can also be used in entirely new applications, such as cryogenic photonic, where BTO can provide the last missing component for photonic quantum computers and quantum interconnects.

1.4 STRUCTURE OF THIS THESIS

After the introduction to the topic in this Chapter 1,

Chapter 2, "Barium titanate", provides an introduction to BTO from a materials perspective. The deposition of the material and the associated challenges are discussed in more detail, as are studies performed on blanket BTO thin films using second harmonic generation.

In Chapter 3, "Optical losses in BTO-Si devices", the issue of large propagation losses in previous work is tackled, and an explanation and solution to the problem is presented.

In Chapter 4, "The Pockels effect in BTO-Si devices", unambiguous proof of Pockels effect in BTO-on-Si thin films and quantification of the Pockels coefficients is discussed.

Chapter 5, "A monolithically integrated Pockels modulator", reports the fabrication and demonstration of a BTO modulator monolithically integrated on and advanced silicon photonics platform.

Chapter 6, "Plasmonic BTO modulators", discusses the fabrication and characterization of a new type of BTO plasmonic modulator for ultra-high bandwidth data transmission.

In Chapter 7, "BTO for cryogenic photonic circuits", the potential for BTO to be used in cryogenic photonic circuits is investigated. Potential applications in quantum- and supercomputing are discussed, and the previously unexplored low-temperature Pockels response are discussed.

Finally, in Chapter 8 a conclusion and outlook of the work is given, highlighting the main achievements and outlining some of the future challenges on the topic.

Chapters 3-7 mainly discuss results which have been presented in various papers. The results are summarized in each chapter, and the full manuscripts are included in Appendices A-E respectively.

Many of the results presented in this thesis are the outcome of scientific collaborations. For transparency, the individual contributions are clarified in the section "Contributions to this thesis".

2

BARIUM TITANATE

2.1 FUNDAMENTALS OF BARIUM TITANATE

BTO is a well know ferroelectric material with a perovskite crystal structure. The room temperature phase of BTO has a tetragonal unit cell (space group P4mm). The lack of centrosymmetry arises from the displacement of the titanium atom from the center of the unit cell due to a double-well energy potential [55]. This displacement gives rise to a polarization of the unit cell, which can be reversed by shifting the titanium atom to the opposite site in the double-well potential. The displacement of the titanium atom is what gives BTO its ferroelectric properties.

2.2 $BaTiO_3$ DEPOSITION

As described in Chapter 1, BTO can be epitaxially deposited on silicon substrates. This offers a significant benefit in terms of scaling and integration, as the use of silicon substrates allows for deposition on large diameter wafers, unlike many other Pockels materials. Epitaxy requires nucleation from an atomically ordered surface, and the amorphization of the surface of silicon in presence of oxygen is a challenge to grow oxide material on such surfaces. Direct epitaxy of BTO on silicon is possible [44], but a more stable process is available for epitaxy of $SrTiO_3$ (STO), due to the possibility to create a monolayer of the compound $SrSi_2$. [56–58]. A thin layer of STO can then be deposited without oxidation of the Si substrate (Figure 2.2a) and used as a seed layer to enable growth of high-quality BTO. Epitaxial deposition of STO on silicon requires highly controlled deposition under ultra-high vacuum (UHV). These requirements make molecular beam epitaxy (MBE) the most suitable deposition technique. MBE allows for highly controlled deposition rates, enables deposition at low temperature and is compatible with a wide pressure range from UHV to 10^{-4} Torr of oxygen. Recently, successful deposition of STO on silicon has been demonstrated using pulsed laser deposition [59], but the same crystal quality as with MBE [58, 60] has not yet been achieved.

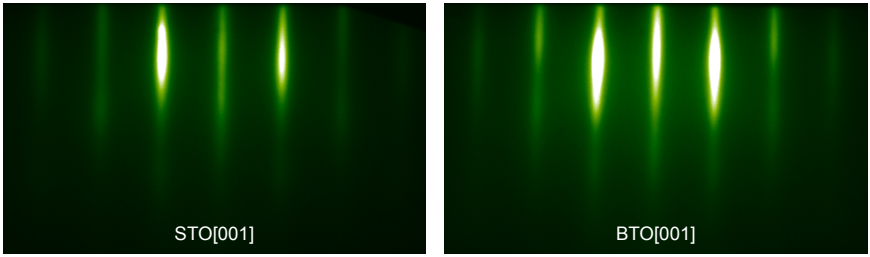

(a) (b)

FIGURE 2.1: RHEED diffractograms of epitaxial (a) STO and (b) BTO on Si substrates. The low modulation of the crystal truncation rods (CTRs) indicate a high-quality layer with low roughness [63].

The process for MBE of STO on Si starts with the deposition of 0.5 monolayers (MLs) of Sr on an oxide-free Si(100) substrate [61]. This step requires that the native oxide present on all silicon substrates has first been removed. Oxide removal can be performed either *ex-situ*, e.g. by selective etching using HF, or *in-situ* using Sr-assisted oxide removal [62]. After deposition of 0.5 MLs Sr at a temperature of ∼600-700°C, the substrate is cooled to 50°C at which point the Sr layer is oxidized using molecular oxygen. Amorphous STO is then deposited at the same temperature, under molecular oxygen at a pressure of $\sim 5 \times 10^{-7}$ Torr. To crystallize the amorphous STO, the substrate is heated to 400-500°C under UHV. In this thesis, 4-nm-thick STO layers were used as seed-layers for BTO growth.

After deposition of STO, crystalline BTO is deposited in a growth process at 500-600°Cand under atomic oxygen. A plasma source is used to generate atomic oxygen at a pressure of $\sim 5 \times 10^{-6}$ Torr. During the growth of both STO and BTO, the crystallinity of the surface is monitored using RHEED. The observed diffraction pattern clearly shows epitaxial growth of both STO (Figure 2.1a) and BTO (Figure 2.1b).

During the BTO deposition the Si substrate is oxidized by oxygen diffusion through the deposited BTO/STO layer, resulting in the formation of a 2-5 nm SiO_2 layer at the interface between Si and STO (Figure 2.2b). The BTO layer can be grown using various deposition methods, e.g. pulsed laser deposition (PLD), chemical vapor deposition (CVD) [64, 65], but as is the case for STO deposition, MBE has so far proven the best method to produce the high-quality layers needed to reach large Pockels coefficients [66].

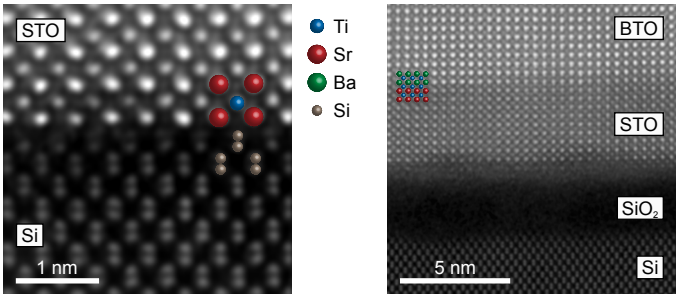

FIGURE 2.2: Electron micrographs of STO and BTO deposited using the methods described above. (a) Filtered HRSTEM image of the epitaxial Si/STO interface along STO(001) direction. The MBE deposition results in an SiO_2-free interface. (b) Filtered HRSTEM image of BTO deposited on a STO-buffered Si substrate. A thin SiO_2 layer is formed during BTO deposition.

Because of the lattice mismatch to the substrate of 4 % at room temperature, in the first 20-30 nm the BTO lattice is oriented with the long *c*-axis of the tetragonal unit cell out-of-plane (OOP). Beyond this critical thickness, the crystal relaxes with the *c*-axis in-plane (IP) leaving the short *a*-axis in the OOP direction (Figure 2.3a) [67]. When the *c*-axis of BTO is oriented IP, it breaks the 4-fold symmetry of the Si(100) substrate. This is mitigated by the formation of crystalline domains with the *c*-axis in orthogonal directions (Figure 2.3b) [51]. The microstructure of such domains and its impact on ferroelectric poling will have significant implications on device performance and needs to be understood to design efficient modulators.

The epitaxial relationship between the Si substrate and BTO can be observed using XRD (Figure 2.4). If the BTO was not epitaxial other reflections than *h*00 would be visible in the OOP $\theta - 2\theta$ scan. Also the presence of *c*-axis OOP and IP orientations appears as two convoluted peaks in the *h*00 reflections. The convoluted peaks are the most distinguishable in the BTO 400 reflection, where a clear asymmetry is visible.

For oppositely polarized ferroelectric domains the nonlinear optical response cancels, resulting in an effective Pockels coefficient of 0 [51]. To avoid such a situation the BTO layer needs to be electrically poled. The domain structure of the layer means that poling along the *c*-axis of one orientation will not pole the orthogonally oriented ferroelectric domains (Figure 2.5a). The most efficient way to pole all domains is to apply the

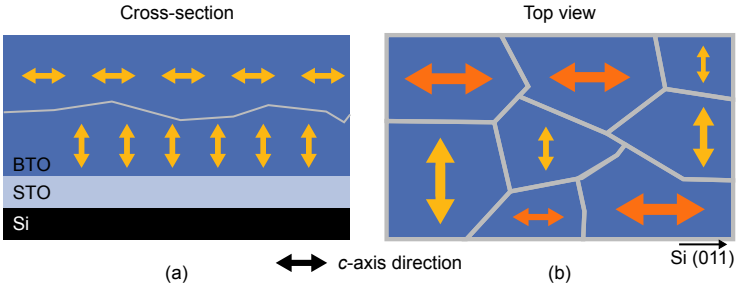

FIGURE 2.3: Schematic illustration of domain structure in thin film BTO. (a) At the epitaxial interface the BTO is oriented with the *c*-axis OOP. Once the thickness exceeds 20-30 nm the *c*-axis relaxes to IP. (b) Because of the cubic substrate, the IP *c*-axis domains will be oriented along orthogonal directions, resulting in a microstructure with four possible ferroelectric polarization directions.

poling field 45° rotated from the *c*-axis orientations (Figure 2.5b). It is then possible to exploit the Pockels response of all the ferroelectric domains in the material. The IP domain structure and poling behavior are essential aspects in order to design efficient EOMs. To ensure that the EOM exploits the largest possible Pockels response, the ferroelectric domain structure and poling thereof needs to be considered [69, 70].

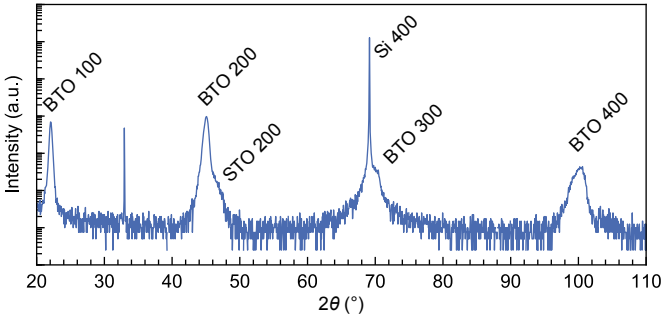

FIGURE 2.4: OOP XRD of BTO thin film. The lack of reflections besides *h*00 is consistent with an epitaxial relationship to the substrate Si, confirmed by azimuthal scans as well as by RHEED. The asymmetry of the BTO peaks show the presence of *c*-axis OOP and IP orientations in the BTO layer. The peak at $2\theta \sim 33°$ is the forbidden Si 200 reflection which appears due to multiple diffraction [68].

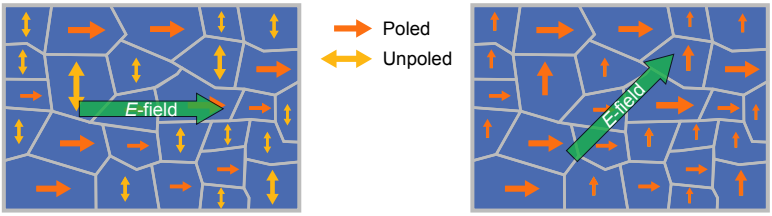

FIGURE 2.5: Schematic of the resulting ferroelectric domain structure in BTO thin film when poling (a) along one of the *c*-axis orientations (0°-direction) or (b) at an angle between two orthogonal directions (45°-direction)

2.3 SECOND HARMONIC GENERATION IN BTO

To verify the micro-domain structure and the poling behavior of BTO we performed SHG characterization of BTO thin films. Like the Pockels effect, SHG depends on the $\chi^{(2)}$ susceptibility of BTO. SHG is the generation of light with double the frequency of the incident light. The electric field of the incident light, $\mathbf{E}(\omega)$, induces a polarization, $\mathbf{P}(2\omega)$, which acts as a source of frequency doubled light with an intensity $I(2\omega) \propto |\mathbf{P}(2\omega)|^2$. The induced polarization is determined by the $\chi^{(2)}$ tensor of the material according to eq. 2.1 [71, 72].

$$\mathbf{P}(2\omega) = \epsilon_0 \chi^{(2)} \mathbf{E}(\omega)\mathbf{E}(\omega) \tag{2.1}$$

Because of permutation symmetry, the third-rank tensor $\chi^{(2)}$ can be expressed as a reduced susceptibility tensor d_{ij} [71], leading to eq. 2.2 to express the SHG.

$$\mathbf{P}(2\omega) = \epsilon_0 \begin{pmatrix} d_{11} & d_{12} & d_{13} & d_{14} & d_{15} & d_{16} \\ d_{21} & d_{22} & d_{23} & d_{24} & d_{25} & d_{26} \\ d_{31} & d_{32} & d_{33} & d_{34} & d_{35} & d_{36} \end{pmatrix} \begin{pmatrix} E_x(\omega)^2 \\ E_y(\omega)^2 \\ E_z(\omega)^2 \\ 2E_y(\omega)E_z(\omega) \\ 2E_x(\omega)E_z(\omega) \\ 2E_x(\omega)E_y(\omega) \end{pmatrix} \tag{2.2}$$

In the case of BTO the P4mm symmetry results in a reduced susceptibility tensor where only 5 non-zero elements remain, of which 3 are independent, leading to an induced polarization:

$$\mathbf{P}(2\omega) = \epsilon_0 \begin{pmatrix} 0 & 0 & 0 & 0 & d_{15} & 0 \\ 0 & 0 & 0 & d_{15} & 0 & 0 \\ d_{31} & d_{31} & d_{33} & 0 & 0 & 0 \end{pmatrix} \begin{pmatrix} E_x(\omega)^2 \\ E_y(\omega)^2 \\ E_z(\omega)^2 \\ 2E_y(\omega)E_z(\omega) \\ 2E_x(\omega)E_z(\omega) \\ 2E_x(\omega)E_y(\omega) \end{pmatrix} =$$

$$\epsilon_0 \begin{pmatrix} d_{15}2E_x(\omega)E_z(\omega) \\ d_{15}2E_y(\omega)E_z(\omega) \\ d_{31}E_x(\omega)^2 + d_{31}E_y(\omega)^2 + d_{33}E_z(\omega)^2 \end{pmatrix} \quad (2.3)$$

where the z-direction is along the c-axis of the unit cell.

It is possible to study the SHG in ferroelectric thin films using various methods such as scanning SHG microscopy, SHG interference contrast imaging or near-field SHG microscopy [72]. These techniques allow for the determination of several important material properties such as crystal symmetry, Curie temperature, domain structure. We used a technique based on SHG by high-intensity laser pulses [73] to probe the domain structure and poling behavior of BTO thin films. In the experimental setup the pump laser incidence angle is along the surface-normal of the BTO thin films and the generated second harmonic signal is detected along the same propagation direction (Figure 2.6). In the experiment a polarizer is used to vary the incident polarization and an analyzer is used to select the detected polarization.

The SHG contribution of BTO domains with the c-axis oriented OOP corresponds to an incident polarization with $E_z(\omega) = 0$ (eq. 2.4). The resulting polarization lies in the plane of the BTO meaning no second harmonic can be detected in the experiment.

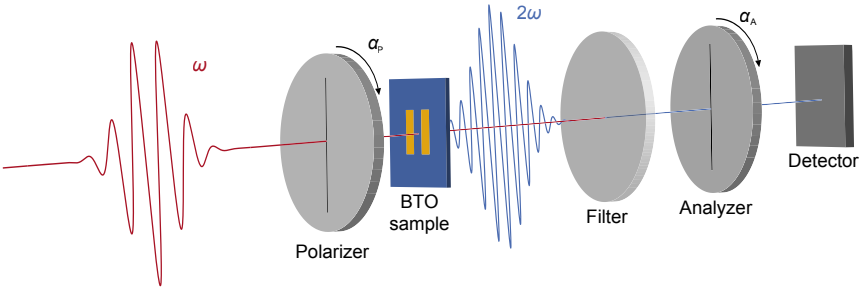

FIGURE 2.6: Schematic drawing of the experimental setup for SHG measurements. A pulsed laser at wavelength ω is used to generate second harmonics, at wavelength 2ω, in the BTO sample. The polarization of the incident light is set using a polarizer. After the sample, a filter is used to remove the pump frequency. Before the detector, an analyzer is used to select the polarization component to be measured. Not all optical elements in the optical path are shown.

$$\mathbf{P}(2\omega) = \epsilon_0 \begin{pmatrix} 0 \\ 0 \\ d_{31}E_x(\omega)^2 + d_{31}E_y(\omega)^2 \end{pmatrix} \tag{2.4}$$

The SHG of BTO with the c-axis is oriented IP can be described by an incident field with $E_x(\omega) = 0$:

$$\mathbf{P}(2\omega) = \epsilon_0 \begin{pmatrix} 0 \\ d_{15}2E_y(\omega)E_z(\omega) \\ d_{31}E_y(\omega)^2 + d_{33}E_z(\omega)^2 \end{pmatrix} \tag{2.5}$$

The expression in eq. 2.5 describes the SHG from a single IP domain. It accurately describes the case when the BTO is poled only in one direction (0° poling, Figure 2.5a), as unpoled domains will have zero net-contribution. When domains with orthogonal orientation are poled (45° poling, Figure 2.5b) the SHG contribution of both domain orientations (0° and 90°) must be considered. The SHG of the 90° domains can be described by introducing a rotation of the $\chi^{(2)}$ tensor in eq. 2.1. In a more intuitive way, it can also be described by a rotation of the reference frame of incident electric field:

$$\begin{pmatrix} E_{x'}(\omega) \\ E_{y'}(\omega) \\ E_{z'}(\omega) \end{pmatrix} = \begin{pmatrix} 1 & 0 & 0 \\ 0 & 0 & -1 \\ 0 & 1 & 0 \end{pmatrix} \begin{pmatrix} E_x(\omega) \\ E_y(\omega) \\ E_z(\omega) \end{pmatrix} = \begin{pmatrix} E_x(\omega) \\ -E_z(\omega) \\ E_y(\omega) \end{pmatrix} \tag{2.6}$$

resulting in a polarization:

$$\mathbf{P'}(2\omega) = \epsilon_0 \begin{pmatrix} 0 \\ d_{15} 2 E_{y'}(\omega) E_{z'}(\omega) \\ d_{31} E_{y'}(\omega)^2 + d_{33} E_{z'}(\omega)^2 \end{pmatrix} = \epsilon_0 \begin{pmatrix} 0 \\ -d_{15} 2 E_y(\omega) E_z(\omega) \\ d_{31} E_z(\omega)^2 + d_{33} E_y(\omega)^2 \end{pmatrix} \tag{2.7}$$

which is then then rotated back to the original frame of reference:

$$\mathbf{P}_{90}(2\omega) = \begin{pmatrix} 1 & 0 & 0 \\ 0 & 0 & 1 \\ 0 & -1 & 0 \end{pmatrix} \mathbf{P'}(2\omega) \tag{2.8}$$

The contributions from 0°- and 90°-domains is then summed to the total induced polarization ($\mathbf{P}_{\text{sum}}(2\omega)$):

$$\mathbf{P}_{\text{sum}}(2\omega) = \mathbf{P}_0(2\omega) + \mathbf{P}_{90}(2\omega) \tag{2.9}$$

In the experiment, the incident electric field is determined by the angle of the polarizer (α_{P}):

$$\mathbf{E}(\omega) = \begin{pmatrix} 0 \\ \cos(\alpha_{\text{P}}) \\ \sin(\alpha_{\text{P}}) \end{pmatrix} \tag{2.10}$$

The analyzer in the experiment is used to select the polarization of the detected second harmonic (P_{det}). This corresponds to a projection of the induced polarization onto a unit vector in the analyzer orientation ($\mathbf{u}_{\text{A}}$):

TABLE 2.1: Measurement configurations of polarizer (α_P) and analyzer (α_A) angles used to characterize BTO thin films using SHG.

Measurement	α_P (°)	α_A (°)
Anisotropy (0°)	0 to 360	0 to 360
Anisotropy (90°)	−90 to 270	0 to 360
Polarizer (0°)	0 to 360	0
Polarizer (90°)	0 to 360	90

$$\mathbf{P}_{\text{sum}}(2\omega) = \mathbf{P}_{\text{sum}}(2\omega) \cdot \mathbf{u}_A \mathbf{u}_A, \quad \mathbf{u}_A = \begin{pmatrix} 0 \\ \cos(\alpha_A) \\ \sin(\alpha_A) \end{pmatrix} \tag{2.11}$$

The measured intensity of the SHG is then:

$$I(2\omega) \propto |\mathbf{P}_{\text{sum}}(2\omega)|^2 \tag{2.12}$$

In the experiment four different polarizer-analyzer configurations (Table 2.1) were used to probe the SHG anisotropy.

For the experiments, a 50-nm-thick BTO layer was deposited on a STO-buffered Si substrate. An intrinsic silicon substrate was used in order to reduce the optical absorption of the second harmonic ($\lambda_{2\omega} = 650$ nm) and to enable the application of an electric field oriented in-plane across the BTO. Pairs of metal electrodes were deposited on top of the BTO to allow for ferroelectric poling as discussed above. An electric field of 5 MV/m was applied for 10 minutes to pole the BTO before SHG measurements. Using electrodes oriented along specific crystalline directions additionally allowed us to verify the micro-domain structure and poling behavior illustrated in Figures 2.3 and 2.5. We measured the SHG with poling electrodes rotated 0, 45, 90 and 135 degrees relative to the BTO<001> direction (Figure 2.7).

Because the generated second harmonic intensity depends on the excitation volume, absorption coefficients, and phase matching as well as on $\mathbf{P}_{\text{sum}}(2\omega)$ the experiment does not allow for determination of the absolute values of the tensor elements. However, the relative magnitudes can be determined and compared to literature values. To determine the relative tensor elements, we fitted the measured experimental data using an analytical model

TABLE 2.2: Comparison of d_{ij} measured in BTO thin films to values for bulk BTO. Ratios between the tensor elements are used for comparison since absolute values can not be determined in the experiment. The uncertainty given is the standard deviation of the ratios determined from different poling-directions.

	Bulk [74]	thin film
d_{15}/d_{31}	1.08	1.37 ± 0.26
d_{35}/d_{31}	0.43	0.41 ± 0.12

based on eqs. 2.5-2.12. We see that the experimental data can be accurately reproduced using the tensorial model described above and taking into account the two orthogonal domain orientations in BTO thin films. Based on this result, we can assume the microstructure of BTO and the poling behavior described in Figure 2.5. To analyze the fitted susceptibility tensor we compare it to literature values for bulk BTO crystals [74]. Because absolute values could not be determined, we compared the ratios between the individual tensor elements. We found that the ratios are very similar to those in bulk BTO (Table 2.2), an indication of the high structural quality of the thin film BTO.

2.4 CONCLUSION

The fabrication of high structural quality BTO is crucial to make efficient EOMs. To this end, MBE has been used to epitaxially deposit BTO on silicon substrates. It is necessary to understand the domain and poling behavior of thin film BTO in order to design efficient EOMs [70]. We used SHG to experimentally characterize these aspects of BTO thin films, providing valuable insight for device design. We verified that the BTO-on-Si is polar, and has an IP-oriented orthogonal domain structure. To the best of our knowledge, the experiment also constitutes the first demonstration of SHG in BTO thin films deposited on silicon substrates. The expanded understanding of the structural and ferroelectric behavior of BTO-on-Si can be used for designing efficient integrated devices.

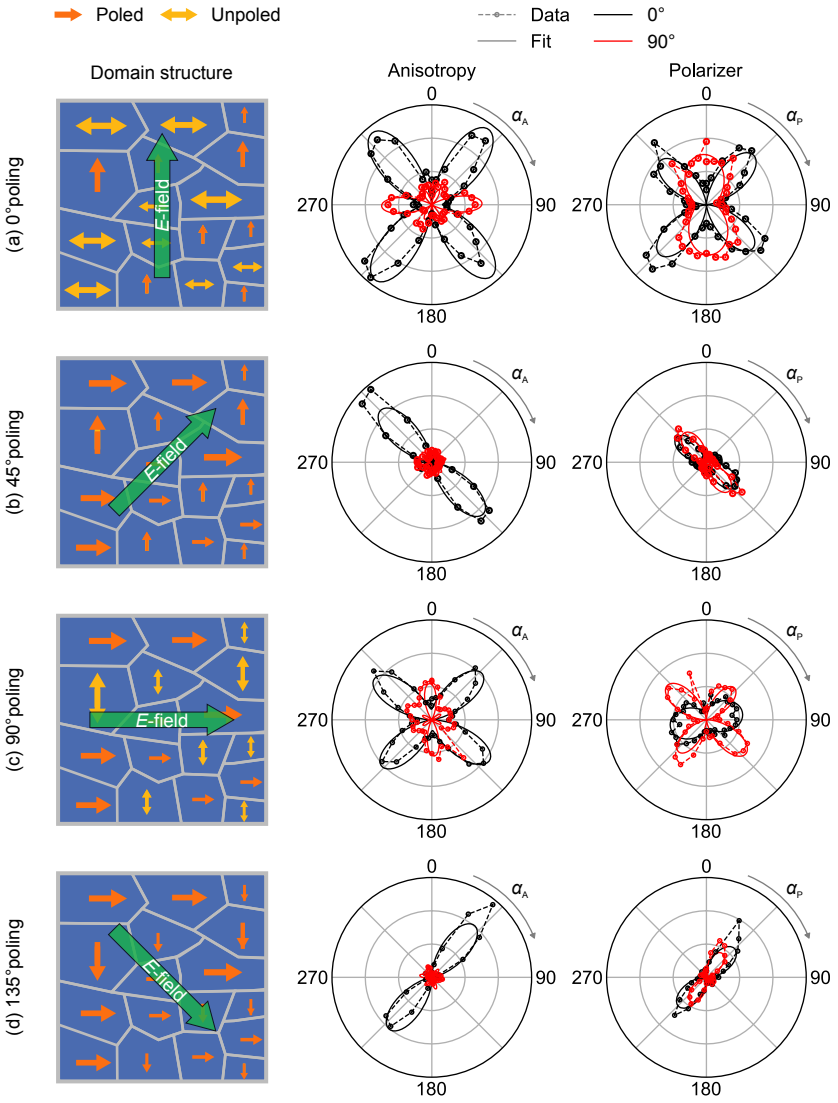

FIGURE 2.7: SHG in BTO poled along (a) 0°, (b) 45°, (c) 90°, (d) 135° directions.

3

OPTICAL LOSSES IN BTO-SI DEVICES

This chapter discusses the challenge of large optical losses in BTO devices, detailing a thorough investigation into the origin of the losses, and providing a solution. The chapter constitutes a summary of the results published in

Eltes, F., Caimi, D., Fallegger, F., Sousa, M., O'Connor, E., Rossell, M. D., Offrein, B., Fompeyrine, J. & Abel, S. *Low-loss $BaTiO_3$-Si waveguides for nonlinear integrated photonics*. ACS Photonics (2016).

The accepted version of the manuscript, containing all the technical details of the study, can be found in Appendix A.

3.1 INTRODUCTION

As discussed in Chapter 1, large propagation losses have been one of the main challenges in previous work on BTO-Si devices. In order to be competitive with with silicon-based modulators, and to bring the full benefits of Pockels modulators, the devices must provide propagation losses comparable to passive silicon waveguides. The occurrence of large propagation losses in BTO-based devices is unexpected, since bulk BTO is transparent in the optical communication wavelength range (1250-1625 nm) [75]. Propagation as low as 1 dB/cm have been reported in BTO-MgO devices [45, 76], confirming that this holds also for thin film BTO. In BTO-Si devices, the reported propagation losses have been in the range from 40 to >500 dB/cm [48, 49, 77]. In state-of-the-art silicon photonics platforms, propagation losses are less than 1 dB/cm [50] in passive waveguides, and ∼10-20 dB/cm in silicon EOMs [4–24, 78]. Since propagation losses contribute directly to the power consumption of optical interconnects, it is imperative to reduce the loss as much as possible.

To investigate the cause of the large propagation losses in BTO-Si devices, we used a simplified waveguide geometry (Figure 3.1a). By directly fabricating SiO_2 strip-loaded waveguides using electron beam lithography, it is possible to probe the propagation losses of thin films without any influence from

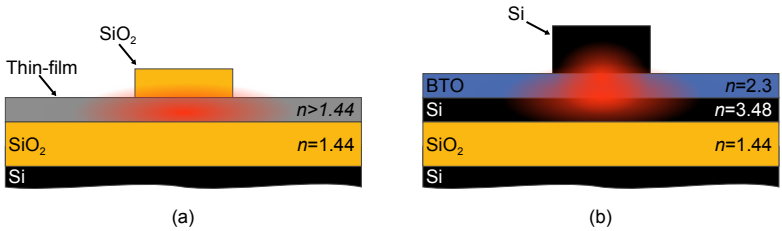

FIGURE 3.1: (a) Simplified SiO_2 waveguide used to probe losses in thin films without any processing influence. (b) BTO-Si slot-waveguide cross-section reported in [49].

the waveguide fabrication process. Using this technique, we measured the propagation losses at each step in the fabrication process of the BTO-Si waveguides reported in [49] (Figure 3.1b).

To extract the propagation loss we used the cut-back method where waveguides of varying lengths are measured. The propagation loss is acquired by fitting the transmitted power as a function of waveguide length.

3.2 ORIGIN OF THE LOSSES

There are three possible mechanisms that can cause propagation losses: (1) absorption of light in a material, (2) scattering from roughness (at sidewalls, interfaces, or material defects), and (3) optical leakage. Since scattering is usually dominated by sidewall roughness from waveguide etching, using the simplified waveguide describe above allows us to distinguish between absorption and scattering. Optical leakage occurs when the waveguide does not fully guide the optical mode and some of the optical power is lost to the surrounding materials. This can be avoided by performing simulations of the waveguide cross-section to ensure that the mode is guided.

To find the origin of the propagation losses we used the simplified waveguide structure (Figure 3.1a) to measure losses at intermediate steps through the fabrication process of BTO-Si waveguides. The process flow for waveguide fabrication starts with BTO epitaxy on a SOI wafer, after which the BTO layer and device silicon layer are transferred through wafer bonding onto a SOI acceptor wafer. The wafer bonding contains several steps, starting with deposition of Al_2O_3 adhesion layers using atomic layer deposition (ALD). After deposition of adhesion layers, the wafers are bonded with a thermal

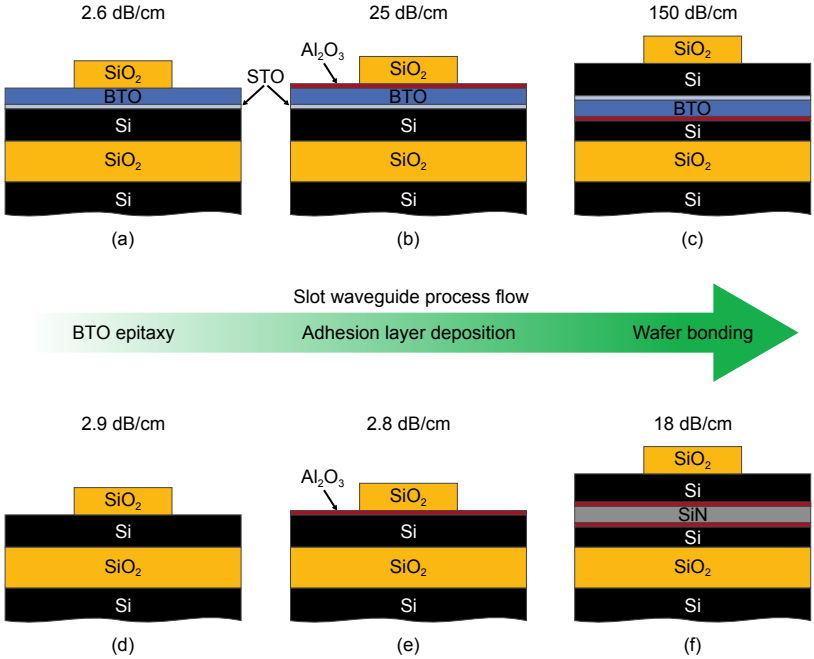

FIGURE 3.2: Schematics of waveguide cross sections and propagation losses at different stages during the processing. The final waveguide geometry matches that of previously reported BTO-Si devices [47–49].

annealing at 250°C to enhance the bonding energy. After the annealing step the donor wafer is removed by a combination of mechanical lapping and wet etching, leaving the top silicon and BTO layers on the acceptor wafer. To form the final Si-BTO waveguide, the top silicon layer is etched using inductively coupled plasma reactive ion etching (ICP-RIE).

We measured the propagation losses after BTO epitaxy, adhesion layer deposition, and after wafer bonding to find at which point the large propagation losses appear. To determine whether any losses we measured were caused by the presence of BTO, or by the processing steps themselves, we also characterized reference samples with no BTO present. As a reference sample for the slot waveguide structure, BTO was replaced by a silicon nitride layer with a refractive index similar to that of BTO.

We found that the BTO has negligible propagation losses directly after deposition (Figure 3.2a). Losses were induced when depositing the Al_2O_3 adhesion layers (Figure 3.2b) and in the wafer bonding step (Figure 3.2c). That these losses are associated with the presence of BTO was confirmed by comparing the losses to those of the reference waveguides (Figure 3.2e-f). Together, these results show that the processing induces absorption in the BTO or in the STO seed-layer.

The appearance of optical absorption indicates a chemical reaction takes place in the BTO or STO layers. A possible reactant in this process flow is hydrogen, which is released during decomposition of H_2O in the Al_2O_3 deposition process [79], as well as in the bonding process where it is a by-product of the bonding reaction [53, 80]. To investigate whether reaction with hydrogen can cause optical absorption in BTO or STO, we intentionally exposed an unprocessed (low-loss) BTO film to hydrogen plasma and found that it did indeed induce significant losses. We found that the optical losses increased with process time, and could confirm that no losses were induced on a silicon reference sample. Losses induced by hydrogen exposure is also consistent with large propagation losses in BTO-Si waveguides based on amorphous silicon (α-Si) [48, 49]. In the α-Si deposition process, an over-pressure of hydrogen is typically used to reduce absorption in the deposited silicon layer [81].

To understand how hydrogen exposure influences BTO and STO we performed X-ray photoelectron spectroscopy (XPS) on both BTO and STO layers before and after hydrogen exposure. We primarily studied at the titanium 2p peak, as it is highly sensitive to the oxidation state of titanium [82, 83], which is likely to be influenced by a reaction with a reducing species such as hydrogen. The XPS data revealed a chemical change in STO but not in BTO (Figure 3.3). In STO the fraction of Ti in a reduced state (Ti^{3+}) increased significantly after hydrogen exposure, whereas the spectrum of the BTO was unaffected. To confirm that the STO is the primary source of induced optical absorption, we compared the hydrogen-induced propagation losses in waveguides with BTO and STO present to waveguides with only the STO layer. The waveguides showed similar losses, indicating that indeed the STO is the main source of the losses, as absorption in BTO would have caused much larger losses due to the larger optical overlap. Through comparative annealing experiments in ultra-high vacuum, we could show that the absorption in STO is caused by hydrogenation, rather than by the creation of oxygen vacancies. It was also revealed that it is possible to outgas the hydrogen to reduce the propagation losses.

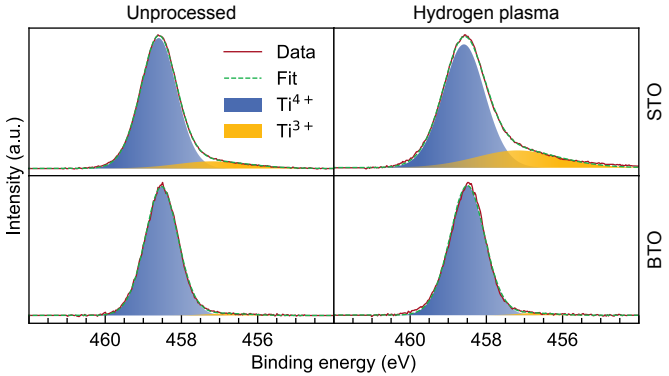

FIGURE 3.3: XPS spectra of the Ti 2p 3/2 peak in BTO and STO before and after exposure to hydrogen plasma. The fraction of Ti^{3+} in STO increases significantly after hydrogen exposure indicating a reduction of Ti in STO [82, 83], whereas there is no significant change in BTO.

3.3 REDUCING PROPAGATION LOSSES

Finally, we applied the insights into the origin of the absorption in BTO-Si waveguides, to fabricate BTO-Si slot waveguides with reduced propagation losses. Knowing that hydrogenation of STO was the cause, we included an additional annealing step after etching of the top silicon layer, to outgas hydrogen from the STO. Before the annealing step, the fabricated waveguides showed ~150 dB/cm of loss. After annealing in oxygen at 350°C for 60 min-

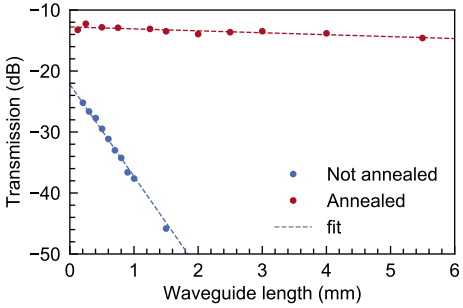

FIGURE 3.4: Cut-back measurements of slot waveguides of varying lengths before and after annealing, showing the reduction of propagation losses.

utes, the propagation losses were reduced to just 6 dB/cm (Figure 3.4). These results show that low-loss BTO-Si waveguides can be fabricated by the addition of an annealing step to degas hydrogen in the STO seed-layer, paving the way for functional electro-optic devices.

3.4 CONCLUSION

Previous works on BTO-Si waveguides reported high propagation losses, taking away any competitive advantage of the technology. We have identified processing-induced hydrogenation of the STO seed-layer as the cause of these high propagation losses. Based on this understanding, we developed annealing procedures to degas the hydrogen and recover the low-loss of the as-deposited state of the material. We could show that the losses in BTO-Si waveguides can be reduced to 6 dB/cm. Further reductions are expected with an improved fabrication process. These results overcome one of the main barriers for the exploration of BTO-Si devices and their application in optical transceivers. Using low-loss BTO-Si waveguides it is now possible to explore the functional properties of BTO for various applications.

4

THE POCKELS EFFECT IN BTO-SI DEVICES

The demonstration of large Pockels coefficients in BTO-Si devices is a missing piece in order to make BTO a suitable material for integration in silicon photonic transceivers. This chapter summarizes the detailed analysis and unambiguous proof of large Pockels coefficient in BTO-Si electro-optic devices reported in

Abel, S., Eltes, F., Ortmann, J. E., Messner, A., Castera, P., Wagner, T., Urbonas, D., Rosa, A., Gutierrez, A. M., Tulli, D., Ma, P., Baeuerle, B., Josten, A., Heni, W., Caimi, D., Czornomaz, L., Demkov, A. A., Leuthold, J., Sanchis, P., & Fompeyrine, J. *Large Pockels effect in micro- and nanostructured barium titanate integrated on silicon*. Nature Materials (2019).

The publication also discusses results on plasmonic devices. These results will be discussed in Chapter 6. For the full technical details, please refer to the full accepted manuscript in Appendix B.

4.1 INTRODUCTION

The modulation efficiency of an EOM is directly proportional to the magnitude of the refractive index change in the active material. For a modulator based on the Pockels effect the refractive index change is determined by the Pockels coefficients of the material according to eq. 1.2. In the case of BTO, the crystal symmetry (space group P4mm) results in the Pockels tensor [84]:

$$r_{ij} = \begin{pmatrix} 0 & 0 & r_{13} \\ 0 & 0 & r_{13} \\ 0 & 0 & r_{33} \\ 0 & r_{42} & 0 \\ r_{42} & 0 & 0 \\ 0 & 0 & 0 \end{pmatrix} \tag{4.1}$$

In bulk BTO crystals r_{42} is the largest coefficient with a magnitude of $\sim$800 pm/V at optical communication wavelengths [37] while the r_{13} and r_{33} are both around 100 pm/V [40]. We have seen in Chapter 2 that BTO deposited on silicon substrates seems to have $\chi^{(2)}$ properties similar to those of bulk crystals, however the SHG experiments does not allow quantitative measurements. Previous work has reported Pockels coefficients much smaller than those of bulk crystals. Based on free-space electro-optic measurements, $r_{42} = 105$ pm/V have been reported. In integrated BTO-Si electro-optic devices, larger Pockels coefficients have been claimed [48, 49]. However, the observed electro-optic behavior is not fully consistent with Pockels-based electro-optic modulation, wherefore it cannot be excluded that spurious effects such as charge migration, plasma dispersion effect, or ionic conduction are contributing to the electro-optic response. A device where the electro-optic response is caused only by the Pockels effect would show certain characteristic features.

First, the Pockels effect is an extremely fast effect, with the frequency response of both ionic and electronic contributions extending into the THz range [85], while the response of potential spurious effects, such as ion diffusion, and thermo-optic effects, is much slower. This means that for a device based on the Pockels effect, the frequency response should be flat up to tens of GHz, where other bandwidth limitations (e.g. *RC* time delay) start to apply. In BTO-Si devices the largest reported bandwidth so far was $\sim$5 GHz [48].

Second, because of the tensorial nature of the Pockels effect, the electro-optic response should depend strongly on the device geometry, specifically the relative orientations of: (1) the propagation direction of the optical mode, (2) the polarization of the optical mode, (3) the modulating electric field, and (4) the crystal axes of BTO. Altogether, this should result in a strong anisotropy of the electro-optic response. In the case of a BTO-Si waveguide with lateral electrodes, the modulating electric field is always in-plane and orthogonal to the propagation direction. However, the propagation direction relative to the crystal axes can be varied, as well as the polarization of the optical mode. Because of the shape of the Pockels tensor of BTO, and the relative magnitudes of the Pockels coefficients, combined with the ferroelectric domain structure (as discussed in Chapter 2), a four-fold rotational symmetric response is expected, with the largest refractive index modulation when the mode propagates along a BTO<011>-type direction [70]. The electro-optic response is also expected to be larger for a TE than a transverse magnetic (TM) mode [69]. The anisotropy in the electro-optic response is something

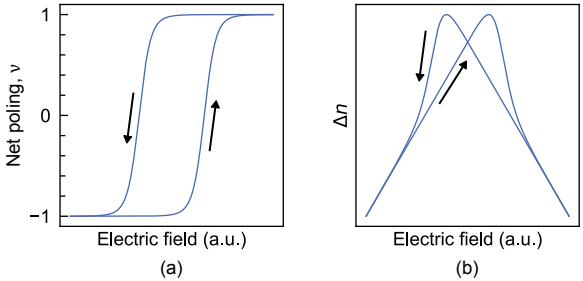

FIGURE 4.1: (a) Example hysteresis curve of ferroelectric material showing the fraction of poled domains versus electric field. (b) Induced refractive index change (Δn) from the Pockels effect in a material with hysteresis curve shown in (a). The arrows indicate the electric field sweep direction.

which has not been shown in previous reports on BTO-Si devices, and which is necessary for accurate extraction of the individual coefficients in the Pockels tensor.

Third, the ferroelectric nature of BTO means that the electro-optic response of the Pockels effect will be convoluted with the effects of ferroelectric domain switching. When the ferroelectric polarization is reversed, so is the electro-optic response. This means that for two ferroelectric domains with opposite polarization, the electro-optic response will cancel (in same way as for the SHG experiments discussed in Chapter 2). The cancellation results in a hysteretic behavior of the electro-optic response as a function of the net poling fraction of the ferroelectric domains (ν). The change in refractive index is proportional to ν as described by eq. 4.2. The relation between domain poling and refractive index change is illustrated schematically in Figure 4.1. The electro-optic hysteresis has been probed in previous work on BTO-Si devices, but has not shown the expected behavior [48, 49].

$$\Delta n = -\frac{1}{2} r_{\text{eff}} \nu n_0^3 E \tag{4.2}$$

These three characteristic features need to be shown to definitely prove the Pockels effect in BTO-Si devices.

4.2 DEVICES TO CHARACTERIZE EO RESPONSE

To probe the electro-optic properties of our BTO-Si waveguides, we used racetrack resonators. It would be possible to use Mach-Zehnder modulators, but due to the large number of device permutations needed, resonant devices were chosen because of their small footprint.

Ring resonators are a common building block in silicon photonics. They can be used as optical filters, switches, and even electro-optic modulators [86]. A ring resonator consists of a ring waveguide evanescently coupled to a straight bus waveguide. The ring will have resonances at certain wavelengths

$$\lambda_{\text{res}} = \frac{n_{\text{eff}} L}{m}, \quad m = 1, 2, 3... \tag{4.3}$$

where n_{eff} is the effective index of the optical mode, and L is the length of the resonator. At the resonant wavelength, the light propagating in the ring interferes constructively with itself, and destructively with the transmitted light in the bus waveguide. The optical power that is coupled into the ring can be tuned to achieve critical coupling, where no light is transmitted through the bus waveguide. If the refractive index of the ring changes, the resonant wavelengths also change. It is therefore possible to switch the transmission of a specific wavelength off or on by tuning the refractive index of the ring. By introducing a pn-junction in a silicon ring resonator, one can make a ring modulator that can be used for high speed data transmission [87, 88]. Ring modulators have limited usefulness in data center transceivers as their resonant nature is intrinsically narrowband, and the strong thermo-optic effect in silicon makes them highly sensitive to temperature fluctuations [89]). However, the high sensitivity of the resonance wavelength to the refractive index in the ring can be used to sensitively measure refractive index changes, for example in sensing applications [86]. In our case, resonators can be used to measure the refractive index change induced in BTO as a function of an applied electrical signal.

As discussed above, the refractive index change of BTO is anisotropic with regards to the crystal orientation. To be able to probe this anisotropy, instead of simple rings we used racetrack resonators, where straight sections are added in the ring structure. Using electrodes along the straight sections, we can apply an electric field across the BTO in a well-defined direction relative

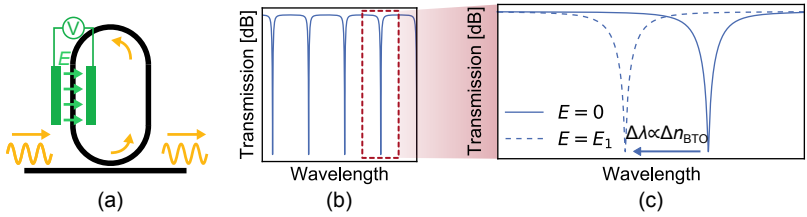

FIGURE 4.2: (a) Schematic of a racetrack resonator as used to measure the refractive index change in BTO. An electric field is applied across the waveguide in the straight section resulting in a shift of the resonance wavelengths. (b) Transmission spectrum of a resonator showing multiple resonances, and (c) induced resonance shift when applying an electrical signal to the phase shifter.

to the crystal orientation, which would not be possible using a simple ring structure (Figure 4.2a). We determine the change in refractive index by measuring the change in the resonance wavelength (Figure 4.2b,c). In order to probe the anisotropic electro-optic response, the racetrack resonators were fabricated with the straight section oriented at varying angles relative to the BTO crystal axes. The polarization dependence of the response was probed using devices designed for TE and TM mode, respectively.

4.3 DEVICE FABRICATION

The slot-waveguide geometry used in previous work, as well as in the study of BTO losses, comes with significant challenges for monolithic integration. To make a slot-waveguide, the BTO needs to be situated between two silicon layers. If integrating BTO devices in the way proposed in Chapter 1 (Figure 1.8), it is difficult to fabricate such a structure. The lack of a crystalline substrate in the BEOL means that two separate bonding steps would be required, leading to added complexity and lower yield. For this reason, we came up with a new waveguide design, exploiting the integration of BTO through wafer bonding. When bonding a BTO layer deposited on an SOI substrate, it is possible to transfer also the top silicon layer of the SOI wafer along with the BTO layer. This was exploited to make slot-waveguides as described in Chapter 3 when transferring the layers onto a SOI substrate. If the BTO and Si layers are transferred onto an oxide layer (such as an ILD), a BTO-Si strip-loaded waveguide can be fabricated by patterning the silicon layer.

The process flow is schematically illustrated in Figure 4.3. We transferred BTO and Si layers, 225- and 100-nm-thick, respectively, to a wafer terminated with a thick (>2 μm) thermal SiO_2 layer. After patterning of the Si waveguides, an annealing step was used to reduced propagation losses. We fabricated electrodes directly on the BTO, followed by deposition of a SiO_2 cladding using plasma-enhanced chemical vapor deposition (PECVD). We

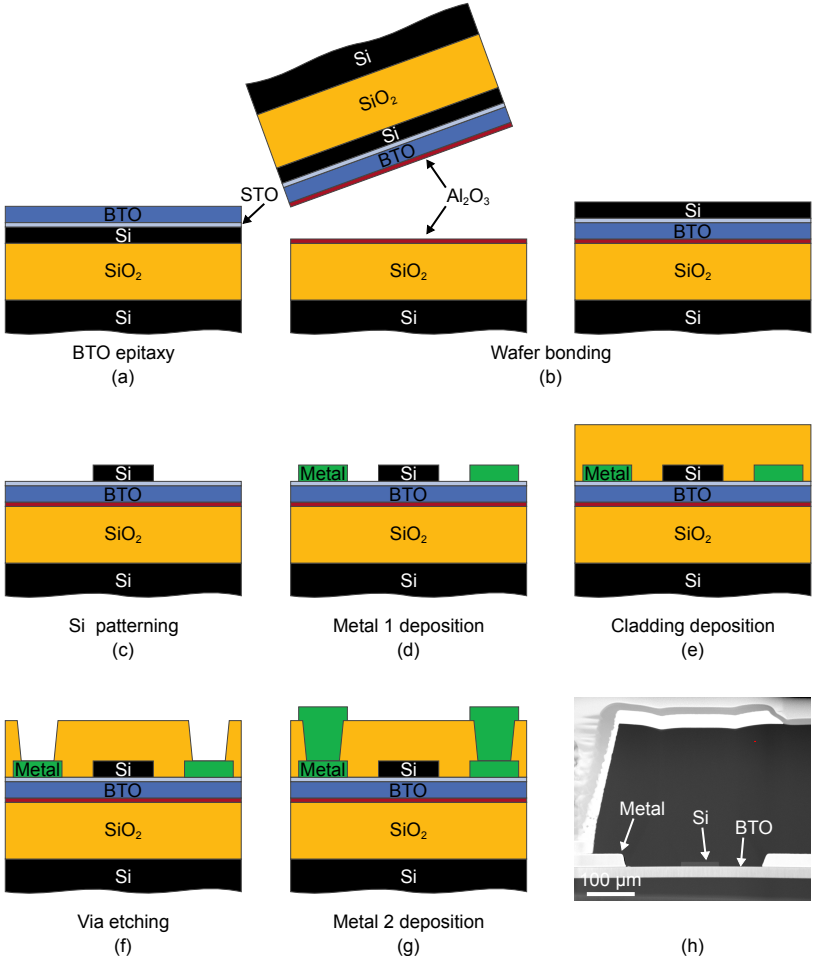

FIGURE 4.3: (a)-(g) Process flow for fabrication of BTO-Si strip-loaded waveguides. (h) Transmission electron micrograph of a fabricated device.

then patterned vias to contact the electrodes, followed by deposition of a second metal layer to make pads for probe contacts.

4.4 CONFIRMATION OF THE POCKELS EFFECT

To confirm the presence of the Pockels effect in BTO-Si devices, we characterized primarily the high-frequency response and the anisotropy of the static EO response. In addition, we also probed the signatures of ferroelectric hysteresis in the EO response.

The high-frequency response of BTO was measured through electro-optic S-parameters. We observe a flat $|S_{21}|$ response up to ~30 GHz (Figure 4.4a), at which point the response of the photo-detector cuts off. The constant response up to high frequency excludes contributions from slow effects (e.g. ionic diffusion or charge carrier accumulation) to the EO response.

We explored the anisotropy of the EO response by measuring the induced refractive index change per volt ($\mathrm{d}n/\mathrm{d}V$) in devices oriented in a range from -90 to $+90$ degrees relative to the BTO<001> axis, for both TE and TM polarization (Figure 4.4b). We observe a strong anisotropy in EO response both for different orientations and for different polarization. The 4-fold rotational symmetry of the response is expected from the domain microstructure, as discussed in Chapter 2. That the largest refractive index change occurs for devices oriented along $\pm 45^\circ$ is consistent with the predicted behavior [70]. We also observe a hysteresis of the EO response as expected from the domain poling in BTO (Figure 4.4c). These three observations unambiguously prove the presence of the Pockels effect in BTO-Si devices.

The extensive characterization of the anisotropy of the EO response allowed us to extract the individual coefficients of the Pockels tensor. We performed simulations of the devices where we varied the magnitude of the Pockels tensor elements to reproduce the experimental data. Based on these simulations, we found $r_{42} = 923 \pm 215$ pm/V and $r_{33} = 342 \pm 93$ pm/V at $\lambda = 1550$ nm. We could not accurately determine the value of r_{13} because of the small response of TM devices at 0° orientation. The value of r_{42} is comparable to that of bulk BTO, which is consistent with the bulk-like behavior observed in SHG experiments. It also represents the largest Pockels coefficient reported in an integrated EO device for any material system.

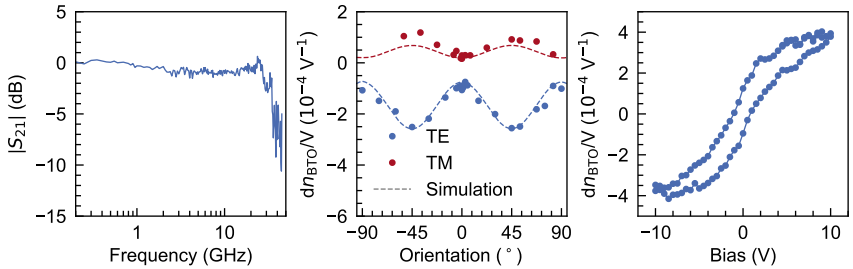

FIGURE 4.4: Characteristic EO response of the Pockels effect in BTO. (a) Frequency response of a photonic ring modulator showing a bandwidth of 30 GHz. (b) Anisotropy of the EO response of BTO-Si photonic devices with different orientations and polarization. The dashed lines correspond to the simulated response using the Pockels tensor extracted from the experiments. (c) EO hysteresis curve obtained at 1 GHz by sweeping the DC bias in a device oriented at $\alpha = 45°$.

4.5 HIGH-SPEED MODULATION USING POCKELS EFFECT

With a strong Pockels effect present in BTO-Si devices, we used ring modulators to demonstrate the potential for high-speed EOMs. We sent a pseudo-random bit sequence (PRBS) to the modulator and recorded the modulated optical signal using a photo-detector and an oscilloscope. Superimposing the repeated sampling of the signal on the oscilloscope results in an eye-diagram, which is commonly used to evaluate the performance of

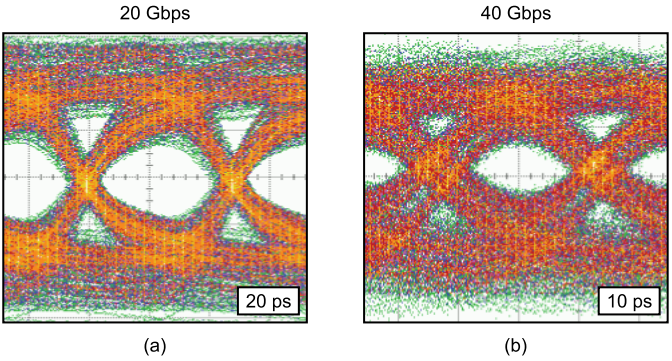

FIGURE 4.5: Eye-diagrams acquired using a BTO-Si ring modulator at data rates of (a) 20 Gbps and (b) 40 Gbps.

EOMs [90]. We were able to record eye-diagrams with open eyes at bit-rates up to 40 Gbps using a BTO-Si ring modulator (Figure 4.5). This demonstrates the potential of BTO devices for high-speed transceiver applications.

4.6 CONCLUSIONS

In this thesis we have performed a thorough study of the Pockels effect in BTO-Si devices. Prior work has reported some of the signatures of the Pockels effect in BTO, but here we unambiguously demonstrate its presence. We extract the largest reported Pockels coefficients of any thin-film materials. We also show the potential of BTO-Si devices for high-speed data modulation. The demonstration of low propagation losses (Chapter 3) and large Pockels coefficients shows the potential of BTO to revolutionize integrated EOMs. However, to fully demonstrate that potential, a viable route to integration with advanced silicon platforms is missing.

5

A MONOLITHICALLY INTEGRATED POCKELS MODULATOR

This chapter describes the integration of BTO modulators on advanced PIC platforms. The results presented here have been published in

Eltes, F., Mai, C., Caimi, D., Kroh, M., Popoff, Y., Winzer, G., Petousi, D., Lischke, S., Ortmann, J. E., Czornomaz, L., Lars, Z., Fompeyrine, J. & Abel, S. *A $BaTiO_3$-based electro-optic Pockels modulator monolithically integrated on an advanced silicon photonics platform*. Journal of Lightwave Technology (2019).

The accepted version of the manuscript, containing all the technical details of the study, can be found in Appendix C.

5.1 INTRODUCTION

Perhaps the most challenging aspect of making technologically viable Pockels modulators is ensuring integration compatibility. Since the aim is to make a modulator that can enhance the capabilities of silicon PICs, the modulator has to be compatible with monolithic integration in advanced silicon platforms. Monolithic integration with PICs imposes various restrictions on the fabrication and properties of the modulator technology, many directly related to the Pockels material itself. Since advanced PIC platforms contain many other types of devices, the integration of the Pockels material must not cause degradation of other components and at the same time the Pockels material must not be degraded by the process steps required by the PIC fabrication and packaging.

Among other things, these restrictions mean that the thermal budget required to integrate the Pockels material must remain within the limits set by the PIC process. Conversely, the Pockels modulator must be compatible with the thermal budget of the PIC processes. The integration scheme must also be compatible with scaling to the large wafer diameters used in commercial production lines (200 and 300 mm). These restrictions are the main reason that no fully PIC-compatible Pockels modulator has been demonstrated, despite multiple demonstrations of high-performance stand-alone

devices. The approach based on silicon-organic-hybrid modulators suffers from chemical and thermal instability [91], making them incompatible with BEOL processing after modulator fabrication. The reported integration of PZT modulators relies on high-temperature annealing steps (>500°C) [92] which is beyond the limits of standard Si PIC thermal budgets. In the case of LN [93, 94], the maximum wafer size is determined by the production of bulk LN crystals and is currently limited to 6".

Using BTO, it is possible to fulfill all of the requirements for successful PIC integration. BTO is thermally and chemically stable, as exemplified by the use of a standard cladding and metallization processes (Chapter 4). The wafer size for BTO thin films is determined by the silicon substrate, imposing no limitations in terms of integration. However, in a monolithic integration scheme direct deposition is not possible because of pre-processing of the silicon substrate. Integration of BTO using direct wafer bonding offers an alternative process compatible with integration in the BEOL.

5.2 INTEGRATION

To demonstrate the potential of BTO for full monolithic integration, we set out to fabricate BTO Mach-Zehnder modulators on substrates from an advanced silicon PIC process. In this first demonstration we chose to integrate the modulators in the BEOL process, after the fourth metal level with a PIC front-end (Figure 5.1a). Such a scheme results in two separate levels for transmit and receive functions. The waveguide cross-section is similar to that used in Chapter 4 but with RF signal lines formed in the top metal level of the PIC platform.

The BTO-Si waveguides were fabricated using the same process as used in Chapter 4. Vias were then etched through the BTO to the electrodes in the PIC top metal level. A final metallization step was used to extend the buried electrodes on top of the BTO to ensure good electric field overlap. Figure 5.2a shows the final cross-section of the monolithically integrated BTO modulator. To demonstrate the scalability of the wafer bonding approach, we performed a first-of-its-kind layer-transfer of BTO deposited on a 200 mm substrate to a 200 mm acceptor wafer.

As discussed above, it is critical that the modulator integration does not cause degradation of the FEOL components of the PIC. In the BTO integration scheme, the wafer bonding transfer uses a maximum temperature of 250°C. A higher temperature step is then used for the BTO waveguide loss

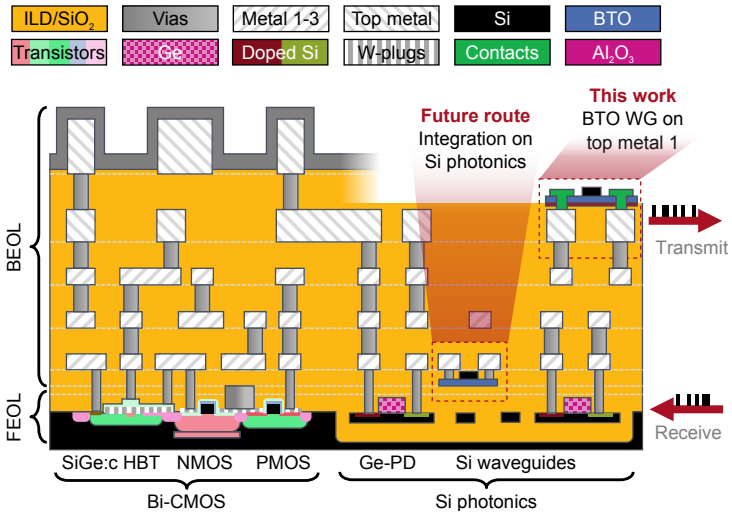

FIGURE 5.1: Scheme for monolithic integration of BTO/Si on PIC platforms. Cross-sections of PIC with electrical and optical front-end, and BTO integration in the back-end (this thesis) or front-end (future route). The RF electrodes to the modulator are fabricated in the BEOL of the PIC platform.

annealing. To ensure that these annealing steps do not negatively impact the FEOL components, we characterized the Ge photodiodes of the PIC front-end before and after BTO integration. We used photodiodes as a reference because they are the most temperature sensitive devices of the FEOL. In both DC and RF characteristics, we found no detectable degradation of the photodiode performance caused by BTO integration. This confirms that our integration approach is fully compatible with silicon PICs.

5.3 MODULATOR CHARACTERIZATION

To determine the performance of the integrated modulators we characterized them passively, under DC bias, and using RF signals. From the passive characterization we measured propagation losses of 5.8 dB/cm, showing that we can reach the same propagation losses as in stand-alone devices (Chapter 3) [95, 96]. These losses could be reduced further by improving the silicon patterning process to reduce the scattering losses of the strip-waveguide. We determined the $V_\pi L$ of the modulators by measuring the induced phase shift as a function of applied bias voltage. We found a $V_\pi L$

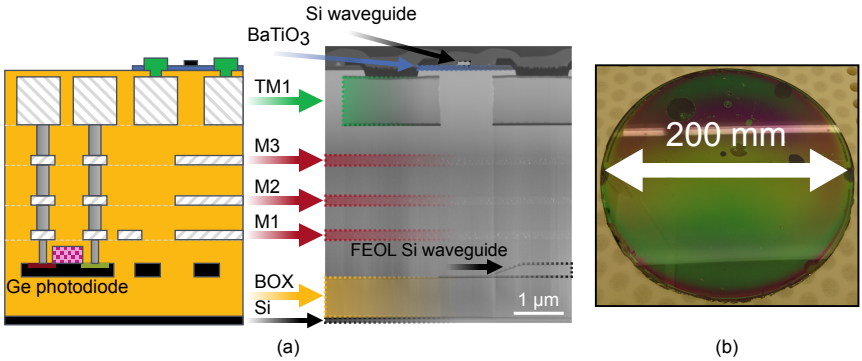

FIGURE 5.2: (a) Cross-sectional scanning transmission electron microscopy (STEM) image of BTO modulator integrated BEOL process of a Si PIC wafer. The schematic shows how the modulator was integrated in this thesis. The electron micrograph shows the successful fabrication of BTO/Si modulators. Intermediate metal levels as well as the FEOL levels can be identified (b) Photo of BTO transferred between 200 mm donor and acceptor wafers.

of just 0.2 V·cm, which is comparable to the most efficient state-of-the-art silicon-based modulators.

The RF performance was characterized by measuring the electro-optic bandwidth in small-signal *S*-parameter measurements, and by recording eye diagrams of transmitted data signals. For these high-speed measurements a 1-mm-long modulator was used. The *S*-parameter characterization revealed a limited bandwidth of ∼2 GHz. From Chapter 4 we know that the intrinsic bandwidth limitation of BTO is not the cause of the low modulator bandwidth. Instead, the reason lies in the electrode design. The electrodes were designed for traveling wave operation without full knowledge of the relevant material properties. This resulted in a mismatch between electrode and source impedance, as well as between RF and optical propagation constants. With an adapted electrode design based on thorough characterization of the material, we expect to reach data rates of more than 50 Gbps. Despite the limited EO bandwidth, we were able to perform data transmission experiments where eye diagrams could be recorded at bit rates up 25 Gbps.

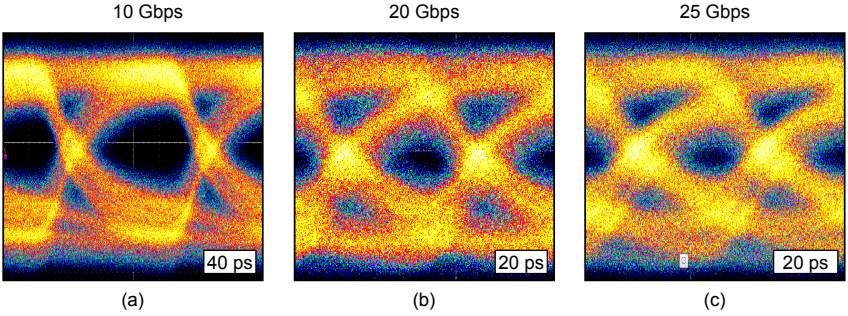

FIGURE 5.3: Data transmission using monolithically integrated BTO modulator at (a) 10 Gbps, (b) 20 Gbps, (c) 25 Gbps.

5.4 CONCLUSION

The metrics of the BTO modulator compares very favorably with state-of-the-art technologies (Table 5.1). The $V_\pi L$ of 0.2 V·cm is 10 times lower than for Si pn modulators (the most commonly used Si modulator type) and in the same range as semiconductor-insulator-semiconductor capacitor (SISCAP) modulators. The benefits of using BTO become the most apparent is in the $V_\pi L\alpha$, where BTO modulators outperform all Si devices by one order of magnitude. FEOL modulators offer a similar $V_\pi L\alpha$ to BTO but the limitation of LN technology is the lack of monolithic integration. The main achievement of BTO technology is the co-integration of Pockels modulators on a PIC platform, offering the maturity of Si PICs and the performance advantages of pure phase modulation. The main limitation of BTO modulators today is the limited EO bandwidth that has been demonstrated, but as discussed above, it is not an intrinsic limitation, and can be overcome in the future by improved electrical design.

TABLE 5.1: Modulator benchmark comparing the performance of the integrated BTO-Si modulator in this thesis to state-of-the-art devices in silicon PIC platforms and stand-alone Pockels modulators. The BTO-Si modulator compares favorably on most metrics, and is the only monolithic technology that can provide pure phase modulation.

	Plasma dispersion		Pockels		
Structure	pn	SISCAP			
Material	Si [15]	Si [97]	Organic [33]	LN [94]	**BTO**
$V_\pi L$ (V·cm)	2.8	0.2	0.06	2.8	**0.2**
$V_\pi L\alpha$ (V·dB)	27	13	2.4	1	**1.3**
BW (GHz)	40	–	20	100	**2/30**
Integration	+	+	–	–	+
Phase mod.	–	–	+	+	+

6

PLASMONIC BTO MODULATORS

This chapter will present results on plasmonic electro-optic modulators. To a large part this chapter summarizes work that was reported in

Abel, S., Eltes, F., Ortmann, J. E., Messner, A., Castera, P., Wagner, T., Urbonas, D., Rosa, A., Gutierrez, A. M., Tulli, D., Ma, P., Baeuerle, B., Josten, A., Heni, W., Caimi, D., Czornomaz, L., Demkov, A. A., Leuthold, J., Sanchis, P., & Fompeyrine, J. *Large Pockels effect in micro- and nanostructured barium titanate integrated on silicon*. Nature Materials (2019).

and

Messner, A., Eltes, F., Ma, P., Abel, S., Baeuerle, B., Josten, A., Heni, W., Caimi, D., Fompeyrine, J. & Leuthold, J. *Integrated Ferroelectric Plasmonic Optical Modulator* in 2017 Optical Fiber Communications Conference Post-deadline Papers (Optical Society of America, Los Angeles, 2017)

The full publications can be found in Appendices B and D, respectively.

6.1 INTRODUCTION

The previous chapters have focused on demonstrating that BTO can be used to make integrated electro-optic modulators, that are compatible with advanced silicon photonic platforms. Despite the progress, there are still challenges remaining, especially demonstrations of high-bandwidth Mach-Zehnder modulators. As discussed in Chapter 5, designing high-speed BTO modulators is not trivial, and will require careful engineering of the device structure, as is the case for all photonic EOMs.

Recently, plasmonic EOMs have emerged as a new device concept which intrinsically overcomes the bandwidth challenges of conventional modulators. Plasmonic modulators build on a metal-insulator-metal (MIM) slot-waveguide, where a surface plasmon polariton (SPP) mode is guided. A SPP is a mode guided at the interface between a metal and a dielectric. In a plasmonic modulator, the dielectric is a material with a Pockels effect. Because the SPP mode is bound to the metal-insulator interface, it can

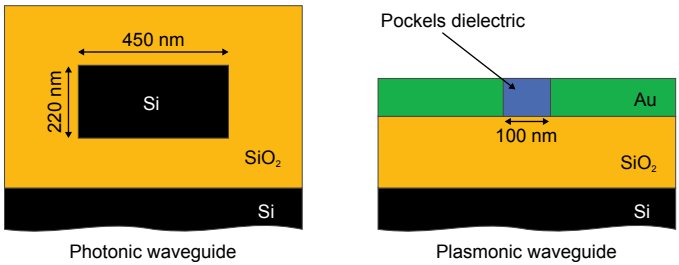

FIGURE 6.1: Schematic illustration of typical silicon photonic waveguide and a plasmonic waveguide used in plasmonic modulators.

be confined in an extremely small volume: the cross-section of plasmonic slot-waveguides is typically around 100 nm by 100 nm (Figure 6.1), less than a one tenth of the vacuum wavelength. The high confinement comes at the coast of optical absorption in the metal (discussed below). The reason plasmonic modulators can operate at extremely high speed is because of the very high modulation efficiency. The very efficient modulation comes from the fact that the optical mode is highly confined between two metal surfaces which also function as electrodes. This means that the electric field overlaps very well with the optical mode, and because of the small distance between the electrodes the electric field strength is very high. $V_\pi L$ values of 0.005 V·cm have been reported [98].

The high modulation efficiency enables the use of extremely short phase shifters, typically in the range of 10-15 μm. Because they are so short, they can operate as a lumped element up to very high frequencies, and therefore are not dependent on the design of traveling wave electrodes. The compact size results in a very high *RC* bandwidth. Plasmonic modulators have been reported to have a bandwidth of more than 500 GHz [99]. A drawback of plasmonic waveguides, which was long considered a show-stopper, is the high propagation losses associated with an optical mode propagating at a metal interface. Typical propagation losses in a plasmonic slot-waveguide are >0.5 dB/μm (>5′000 dB/cm) [100, 101]. However, because the plasmonic modulators can be made extremely short, the use of silicon access waveguides can reduce the insertion loss to less than 8-10 dB [100, 101].

So far, plasmonic modulators have relied on organic materials as the Pockels dielectric with reported in-device Pockels are of ∼200 pm/V. Since nonlinear organic materials suffer from thermal and chemical instability, they

have not been successfully implemented in a full silicon photonics flow, but single device demonstrations of organic plasmonic modulators show great promise. Besides the extremely high bandwidth, data transmission using 120 GBd OOK has been demonstrated [102], as well as 16QAM at 100 GBd to transmit data at 400 Gbps [103].

To fully realize the potential of plasmonic modulators, the organic material needs to be replaced by a stable dielectric with a large Pockels coefficient, such as BTO. The nanometer-scale dimensions of plasmonic waveguides make them very challenging to fabricate. A metal slot filled with a Pockels dielectric needs to be fabricated. When using organic Pockels material, the metal slot can be pre-fabricated using two-step patterning, and then filled with the organic material using a simple spin-coating step [104]. The fabrication becomes more challenging when using a solid-state material such as BTO. As plasmonic BTO waveguides need to be fabricated from an epitaxial thin film, a process based on filling of a pre-fabricated slot is not possible. Therefore the BTO has to be patterned into a fin, followed by metal deposition. Because BTO has a high permittivity, any gap between the electrode and the BTO fin will cause the electric-field to drop across the gap rather than across the BTO, resulting in poor modulation efficiency. For this reason, a novel fabrication method had to be developed in order to successfully fabricate BTO plasmonic waveguides.

6.2 FABRICATION

To make BTO-based plasmonic devices, MIM slot-waveguides with a gap of less than 100 nm need to be fabricated, which poses a significant challenge. First, BTO needs to be patterned into a very narrow fin. Since there is no established chemical dry-etch process available for BTO etching, we relied on physical dry-etching using ion beam etching (IBE). Second, the metal electrodes have to be in direct contact with the sidewalls of the BTO fin, to confine the modulating electric-field inside the BTO. The alignment accuracy of lithography in a research environment is typically limited to >25 nm. This limit makes an lithographically aligned electrode fabrication process impossible, wherefore a process where the alignment is independent of the lithography, a self-aligned process, had to be developed. BTO was etched using argon IBE with a SiO_2 hardmask (Figure 6.2a). The SiO_2 mask was directly patterned using electron beam lithography (EBL) to cross-link hydrogen silsesquioxane (HSQ) to form SiO_2. Direct patterning of SiO_2 enables high aspect ratios of the mask, which is needed because of the

poor etch selectivity of SiO_2 to BTO (4:1). Through optimization of the etch conditions smooth BTO sidewalls with an acceptable verticality (~70°) could be achieved (Figure 6.2b).

A self-aligned process for deposition of the metal electrodes was developed based on a damascene process. Damascene patterning of copper is a commonly used in CMOS fabrication. It uses wet polishing to planarize copper deposited on a pre-structured substrate, allowing for patterning of copper

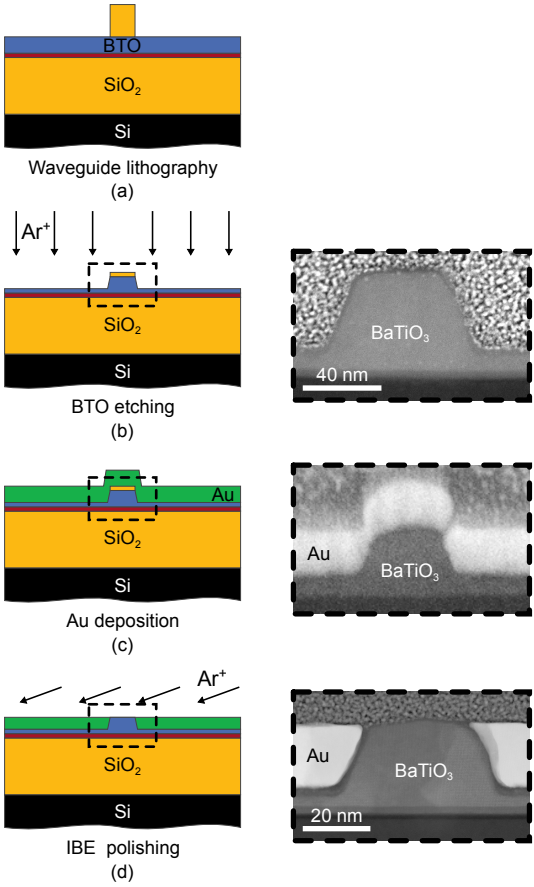

FIGURE 6.2: Process flow for fabrication of BTO plasmonic slot waveguides. The left column shows schematic illustrations of the process steps and the right column shows electron micrographs of the cross-section.

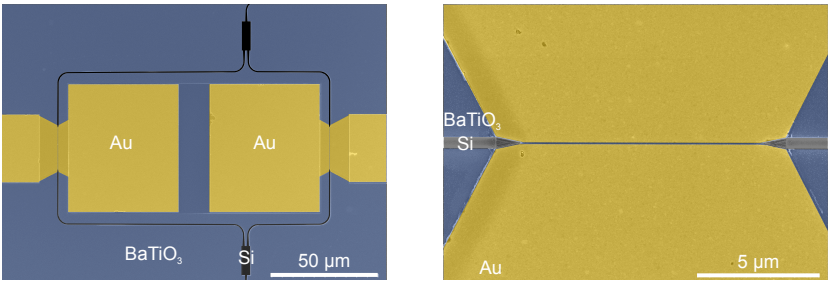

FIGURE 6.3: Colorized electron micrographs showing the layout of plasmonic BTO modulators. (a) Two plasmonic BTO phase shifters embedded in a MZI. (b) A single phase shifter showing the tapers used to couple between photonic Si waveguides and plasmonic BTO waveguides.

without dry etching [105]. The self-aligned deposition of the plasmonic electrodes uses IBE in a dry damascene process. First, metal (Au) is deposited over the BTO fin (Figure 6.2c). Then, low-incidence IBE is used to polish the metal layer. The polishing selectively removes the metal on top of the BTO fin, producing a MIM slot-waveguide with the electrodes in direct contact with BTO (Figure 6.2d). This process was combined with a lift-off to define the plasmonic regions as well as the electrical pads (Figure 6.3a).

Having established a fabrication process for BTO MIM waveguides we combined it with the fabrication of BTO-Si waveguides (Chapter 4) to make low-loss photonic access waveguides. We used linear tapers of the Si strip-waveguides to couple the optical mode into and out of the plasmonic phase shifters (Figure 6.3b) in a similar way to previous work on organic-based devices [104].

6.3 POCKELS EFFECT AND STABILITY

As a first step to characterize the BTO plasmonic modulators, we investigated the Pockels effect signatures and the thermal stability of the devices. For this purpose we used phase modulators which were characterized using 30-65 GHz RF signals. Optical sidebands are produced when modulating the phase of the optical carrier, which can be measured using an optical spectrum analyzer (Figure 6.4). The intensity ratio between the carrier and

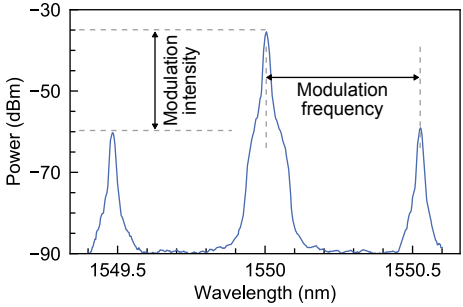

FIGURE 6.4: Optical spectrum of 65 GHz modulation of plasmonic BTO phase shifter. The intensity ratio between the carrier and the sidebands can be used to extract the modulation index [106].

the sidebands is a measure of the induced phase shift by the modulating signal [106].

Similar to the characterization of the Pockels effect in photonic BTO-Si devices (Chapter 4) we characterized the EO response of plasmonic BTO devices to verify the characteristic behavior of Pockels modulation. We found that also the plasmonic modulators exhibit the characteristic hysteretic behavior and anisotropy as expected. When estimating the Pockels coefficient of BTO in the plasmonic we found a value of ∼100 pm/V, which

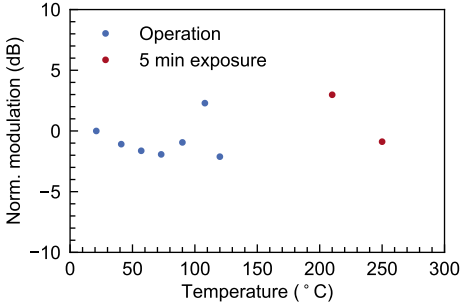

FIGURE 6.5: EO response of a BTO plasmonic phase modulator at 65 GHz at different temperatures. The device could be operated up to 130°C and exposed to temperatures up to 250°C without any degradation. (red). The fluctuations are attributed to coupling challenges.

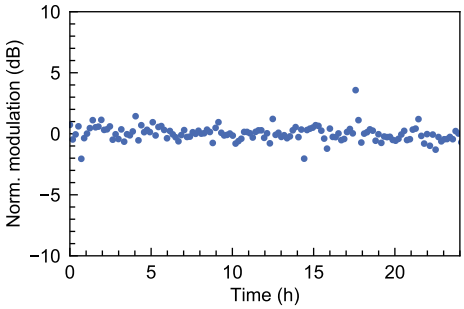

FIGURE 6.6: Continuous operation of the device with modulation at 65 GHz during 24 hours at 90°C showing no sign of device degradation.

is significantly lower than in the photonic devices discussed in Chapter 4. There can be multiple reasons for this discrepancy. The fact that thinner BTO was used means that the fraction of *c*-axis OOP domains in the device is larger. Since these domains do not contribute to EO modulation in this geometry, it will lead to a smaller effective Pockels coefficient. There is also a possibility that the etching of BTO caused damages to the material which degraded the Pockels coefficients. Because of the nano-scale structure of the device, there might also be a larger influence of ferroelectric dead-layers or other interface effects leading to lower modulation efficiency. Understanding what causes the reduced Pockels coefficient can potentially enable much more efficient plasmonic modulators in the future.

One of the anticipated advantages of BTO over organics in plasmonic modulators is the stability of the devices. Since BTO is a thermally and chemically stable material, we do not expect any degradation during device operation at elevated temperature. To measure the thermal stability of the devices, we performed sideband modulation measurements at elevated temperatures with the device operating at up to 130°C (limit of experimental setup), as well as measurements after exposing the device to up to 250°C for 5 minutes. The thermal stress on the device did not result in any detectable degradation of the modulation efficiency (Figure 6.5). We also operated the device continuously for 24 hours at 90°C without observing any degradation of the performance (Figure 6.6).

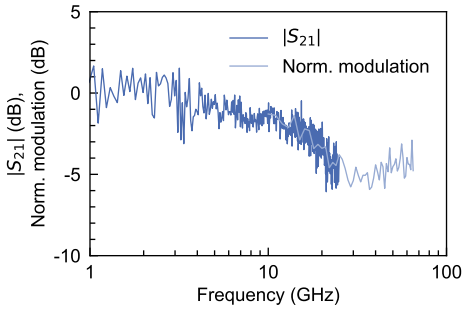

FIGURE 6.7: EO bandwidth of plasmonic BTO modulators.

6.4 BANDWIDTH AND DATA MODULATION

To characterize the device performance for high-speed data transmission, we first measured the frequency response of the devices. We used *S*-parameter measurements to determine the response up to 25 GHz, and sideband modulation measurements from 15 to 65 GHz (Figure 6.7). We observe a constant response up to ∼5 GHz. Between 5 and 25 GHz the modulation magnitude decreases by 5 dB, and from 25 GHz on the response is once again constant.

The drop in modulation amplitude between 5 and 25 GHz might be caused by an elasto-optic cut-off. The fin-structure of the plasmonic BTO device

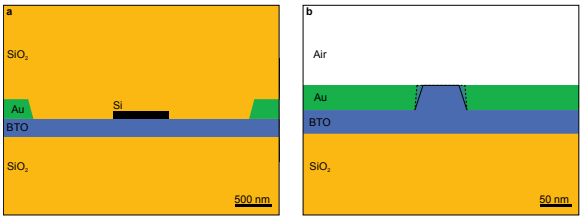

FIGURE 6.8: Schematic drawings of plasmonic and photonic phase shifters. a, In the photonic structure the BTO layer is clamped by the surrounding SiO_2 resulting in a reduced piezoelectric response. b, In the plasmonic structure the BTO has been structured in nano-scale dimensions and is not cladded. Both the lack of a cladding and the structuring reduce the clamping and allows the BTO fin to deform, as indicated in the drawing by the dashed lines, creating an elasto-optic response.

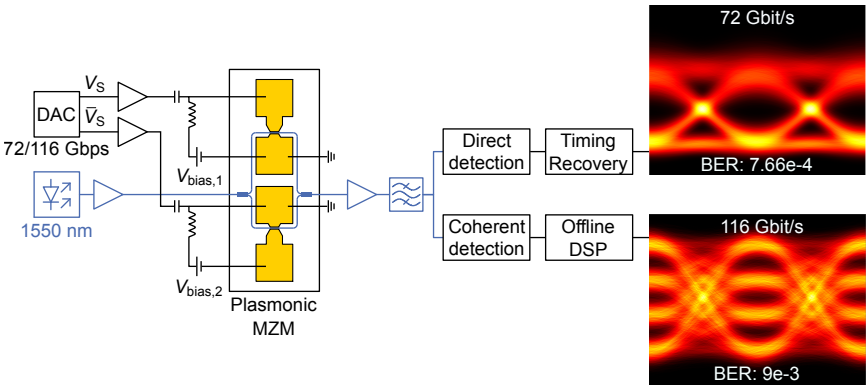

FIGURE 6.9: 72 and 116 Gbps data transmission using plasmonic BTO modulator.

allows for piezo-electric deformation of the BTO, contrary to the planar BTO used in photonic devices (Figure 6.8). The piezo-electric deformation causes an elasto-optic response which decays above 5 GHz modulation frequency, leaving a constant electro-optic response above 25 GHz.

The high bandwidth of plasmonic BTO devices makes it possible to transmit data at extremely high rates. To demonstrate this, we performed data modulation experiments using Mach-Zehnder modulators. We operated the modulator in a dual-drive push-pull scheme, where the signal is applied directly to one arm and the differential signal is applied to the other arm. The push-pull operation doubles the modulation depth while using the same driving voltage. A DC bias was applied to each arm of the modulator to ensure poling of the BTO, and to tune the operating point of the modulator.

With an OOK modulation scheme we successfully transmitted data at 72 Gbps (Figure 6.9), using direct detection and without pre- or post-equalization. The measured bit-error ratio (BER) was 7.7×10^{-4}, which is well below the 7 % hard-decision forward error correction (FEC) threshold of 3.8×10^{-3}. We were also able to transmit data at a rate of 116 Gbps using PAM4 (at 58 GBd) with coherent detection and post-equalization (Figure 6.9). Using this scheme we achieved a BER of 9×10^{-3} which is below the 15 % soft-decision FEC threshold of 1.9×10^{-2}, resulting in a net data rate of more than 100 Gbps.

6.5 CONCLUSION

Plasmonic devices offer a path to extend the functionality of EOMs far beyond the bandwidth limitations of photonic modulators. Plasmonic modulators based on organic materials have been used to demonstrate record performance. However, the organic material itself poses a fundamental restriction on the applicability of such devices. Here we have shown that plasmonic devices based on BTO can can provide the ultimate solution, combining the stability and technology compatibility of BTO with the performance of plasmonics. We used a novel process, developed to allow for self-aligned fabrication of sub-100 nm plasmonic BTO waveguides, to make BTO plasmonic modulator. Finally, we have demonstrated excellent performance of the plasmonic BTO modulators for high-speed data transmission.

7

BTO FOR CRYOGENIC PHOTONIC CIRCUITS

This chapter presents results on exploration of BTO devices for cryogenic applications, including the characterization of previously previously unknown properties of BTO thin films. These results are presented in full in Appendix E, which contains a manuscript has been submitted for publication.

7.1 INTRODUCTION

In Chapters 2-5 we have seen how a technology platform for optical communications was developed based on EOMs exploiting the Pockels effect in BTO thin films. In Chapter 6 this technology platform was used to make novel types of devices, plasmonic modulators, aimed at enhancing the bandwidth of optical transceivers beyond the limitations of conventional EOMs. In fact, the unique properties of BTO enable completely novel types of applications. As an example, the hysteresis of the ferroelectric switching in BTO can be used to make non-volatile optical memories [107]. The electro-static nature of the Pockels effect can also be used to make extremely efficient tuning elements [49, 108]. Another differentiator of modulators based on the Pockels effect is that they can in principle operate in the entire temperature range where the material retains its nonlinear optical properties. In the case of BTO, the upper temperature limit is set by the Curie temperature, which is $\sim$120°C in bulk crystals [109], but is known to be higher in thin films [110]. At temperatures below room temperature, BTO undergoes two phase transitions, at 270 and 200 K respectively [111, 112], but remains ferroelectric and thus has a Pockels effect. This opens the door for using BTO modulators in cryogenic applications, where the performance of silicon modulators heavily degrades due to carrier freeze-out [113, 114].

Cryogenic PICs are a key technology for the implementation of quantum computers and cryogenic supercomputers which need to operate at temperatures of a few-K or less [115–118] (Figure 7.1). While these cryogenic systems generally rely on electrical circuits for computation, optical in-

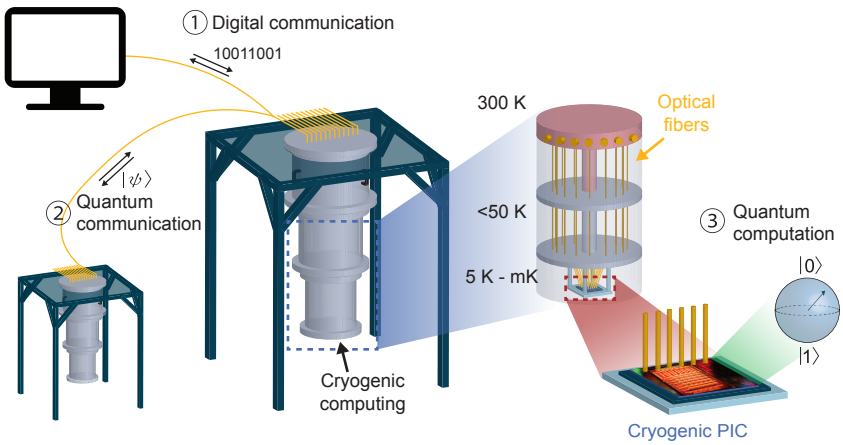

FIGURE 7.1: Schematic over applications for cryogenic PICs. ① Optical interconnects can overcome limitations of electrical wires for classical communication with cryogenic systems. ② Photons are the only viable carrier of quantum states over large distances and at ambient temperature, making them essential for quantum communication. ③ Cryogenic PICs are also pursued as a platform for quantum computing based on the quantum nature of photons.

terconnects is an attractive solution for communication with the outside world at room temperature. Because of the limited cooling power, cryogenic systems need high-bandwidth and thermally insulating interconnects [116, 119]. PICs can offer just that. Optical transceivers have the highest bandwidth available and optical fibers provide excellent thermal insulation. In addition to interconnect applications, cryogenic PICs are also pursued as a platform for quantum computing, where the quantum nature of photons is exploited as qubits [120]. In any photonic quantum computer electro-optic switches and tuning elements are imperative, e.g. for heralded photon sources and trimming of device performance [121, 122]. Photonics also offer the only viable solution to transmit quantum information over long distances and at ambient temperatures. For this reason, optical interfaces are essential to connect multiple quantum computers [123, 124] and for secure remote operation using true quantum communication [125].

While the number of potential applications for cryogenic PICs is growing, there is no technology platform available today that can fulfill the performance requirements. The main reason is the lack of efficient electro-optic switches at low temperature. A viable technology needs to provide low-loss,

low static and dynamic power, and high bandwidth. In attempts to reach these goals devices based either on highly doped pn-junctions [126] or on thermo-optic phase shifters [127] have been explored, based on their widespread use in room temperature PICs. Both of these concept have limited relevance for cryogenic applications due to intrinsic physical limitations. Because of carrier freeze-out at low-temperature the efficiency and bandwidth of plasma-dispersion modulators are strongly reduced compared to at room temperature. Even when using very high doping levels and a micro-disk architecture bandwidths are limited to <5 GHz. The high doping levels also result in increased absorption which makes low-loss switching and tuning impossible. Thermo-optic phase shifters are even more limited in bandwidth (<10 MHz) [128], and while they can be used for tuning and switching they consume large amounts of power. In fact, thermo-optic switches consume even more power than at room temperature due to the reduced thermo-optic coefficient of Si at low temperature [89, 126].

The results presented in the previous chapters of this thesis, as well as demonstrations based on other material systems [33, 92, 94], show that Pockels-based devices can achieve record metrics at room temperature. Because of the electro-static nature of the Pockels effect, there are no intrinsic limitations to achieving high performance with such devices also at few-K temperatures. The technological benefits of BTO-based devices (Si PIC integration, low-losses, material stability) hold also for cryogenic applications. However, in bulk BTO crystals the Pockels coefficients are unknown below 270 K. In thin films the uncertainty is even higher, as the structural behavior is known to differ from bulk due the stress and thermal mismatch between BTO and the substrate [129–131]. Because of this, even the crystal structure of BTO-on-Si is unknown at low temperatures. To know whether BTO is a suitable material for cryogenic PICs it is necessary to determine how its electro-optic properties are affected by cooling to low temperature.

7.2 LOW TEMPERATURE ELECTRO-OPTIC CHARACTERIZATION

To investigate the temperature dependence of structural and electro-optic properties of BTO, we characterized the EO response of photonic BTO-on-Si devices down to 4 K. This allows us to directly determine the efficiency of BTO-on-Si devices for cryogenic applications. If any structural phase transitions occur between room temperature and 4 K they will lead to a

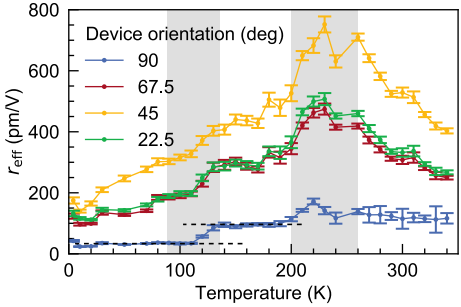

FIGURE 7.2: Temperature dependence of the effective Pockels coefficient in BTO along different crystal orientations. A phase transition in BTO causes a peak around 240 K. A second phase transition occurs around 100 K, resulting in a sharp drop of r_{eff} in 90° devices (indicated by dashed lines). The grey areas indicate the temperature ranges of the respective phase transitions. The error bars show the standard error of the fit used to extract the Pockels coefficients.

change of the Pockels tensor and should therefore be detectable in the EO response.

We used racetrack resonators similar to those described in Chapter 4 to measure the electro-optic properties of BTO as a function of temperature. The waveguide geometry was different in that the BTO layer was thinner, 80 nm instead of 225 nm, and silicon nitride was used as the waveguide material in order to eliminate potential charge-carrier effects present in a silicon strip-waveguide. The refractive index change of BTO was extracted from the resonance shifts in the same way as previously described. From that data the effective Pockels coefficient was determined (see Appendix E for details). We measured devices with varying orientations in order to be sensitive to different elements of the Pockels tensor. We characterized the BTO devices in the range from 4 K to 340 K (Figure 7.2).

The temperature dependence of r_{eff} reveals two distinct features: a peak around 240 K (most pronounced for 45°-device), and a sudden reduction (in particular for 90°-oriented device) around 100 K. Both of these features indicate the occurrence of a phase transition. The peak in the EO response is consistent with the predicted divergence of the r_{42} tensor element of bulk BTO near the transition from tetragonal to orthorhombic structure [38], albeit with the phase transition occurring at a lower temperature than for bulk crystals. The drop in response around 100 K coincides with a change

in the qualitative EO hysteresis of the devices (see Appendix E), indicating that this phase transition is electric-field induced. At a temperature of 4 K, the 45° BTO devices have an effective Pockels coefficient of about 200 pm/V, about a half of the value measured at room temperature. Even though r_{eff} is reduced compared to room temperature, 200 pm/V is still larger than most in-device Pockels coefficients reported for other materials at room temperature [92, 93].

7.3 DEVICE DEMONSTRATIONS

Having observed that a strong Pockels effect remains in BTO thin films at low temperature, we demonstrate some of the key functionalities required from EO switches in cryogenic PICs, low power switching and high-speed modulation, at 4 K. Using a Mach-Zehnder interferometer we are able to show switching between two outputs with a dynamic switching energy of 35 pJ and a static power consumption of just 10 pW. The extremely low static power consumption is possible because of a reduction in BTO conductivity by 10^4 compared to room temperature. The power required to induce a π phase shift (P_π) of 10 pW is more than one billion times lower than for thermo-optic phase shifters [127].

To make a high-speed modulator we optimized the waveguide geometry for more efficient modulation. This optimization included the use of thicker

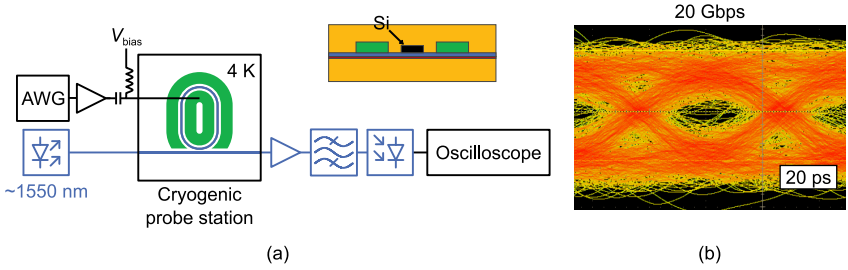

FIGURE 7.3: (a) Schematic of the experimental setup for data modulation. An RF amplifier was used to compensate for losses into the cryogenic probe station. The modulated optical signal was detected using a photodiode and recorded on a high-speed oscilloscope. The inset show the waveguide cross-section. (b) Eye diagram recorded at 20 Gbps with a drive voltage of 1.7 V_{pp}, corresponding to modulation energy of 45 fJ/bit.

BTO (225 nm) and a Si strip-waveguide (the same waveguide cross-section as used in Chapter 4). We used a low-Q ($Q \sim 6'000$) racetrack resonator to allow for a high bandwidth. We successfully recorded eye diagrams at a data rate of 20 Gbps (Figure 7.3). The low drive voltage (1.7 V_{pp}) and device capacitance results in a very low energy per bit of 45 fJ.

7.4 CONCLUSIONS

The lack of efficient electro-optic modulators and switches is the main technological roadblock for cryogenic PIC applications. Here we have shown that BTO technology has the potential to provide this missing piece. Through temperature-dependent EO characterization we have shown that BTO-on-Si thin films exhibit a different phase transition behavior compared to bulk crystals. We found that BTO maintains a large effective Pockels coefficient down to 4 K, despite undergoing phase transitions. Using BTO devices operated at 4 K we have demonstrated record low power switching and tuning, as well as the highest rate data transfer ever achieved using PICs at few-K temperature. These results show the potential of BTO technology to have a major impact on novel fields of PICs beyond optical transceivers.

8

CONCLUSION AND OUTLOOK

The first part of this thesis set out to investigate whether BTO-on-Si can be made a viable technology for modulators electro-optic transceivers. Three main challenges were identified on this path: reducing the large propagation losses, unambiguously proving the presence of a strong Pockels effect in BTO-on-Si, and demonstrating a viable path towards integration with advanced silicon photonic platforms. First, we were able to prove the origin of the large propagation losses in BTO-Si waveguides. We also showed that the losses can be reduced through minor modifications to the fabrication process to produce low-loss BTO-Si waveguides.

Second, through thorough characterization of BTO-on-Si devices we were able to demonstrate all of the characteristic features of the Pockels effect in BTO. Through systematic evaluation of our results we were able to quantify the Pockels coefficients and found record large in-device Pockels coefficients with $r_{42} = 923$ pm/V. The measured Pockels coefficients are the largest reported for any thin film material, which shows the great potential of BTO to revolutionize silicon photonics technology. This potential was further demonstrated by data transmission experiments were ring modulators were used to transmit data at rates up 40 Gbps.

Finally, we demonstrated fully monolithic integration of BTO-Si modulators on an advanced silicon photonics platform. Using an integration scheme based on molecular wafer bonding we fabricated BTO-Si modulators in the BEOL of a PIC platform. We showed that integration of BTO does not have any negative impact on other components in platform, making the integration scheme fully compatible with advanced silicon PICs.

These results lay the foundation for the realization of BTO-Si-based electro-optic transceivers. However, there still challenges to be overcome. The production of BTO-on-Si relies on MBE, a technique which is not well suited to large-scale production. To this end it would be desirable to develop an alternative method for BTO production. The first steps in this direction have already been taken using CVD of BTO [65]. The results are promising but the electro-optic properties of CVD BTO have not yet been thoroughly

investigated, and it is not yet clear whether the same material quality can be achieved as with MBE.

The limited bandwidth of the BTO Mach-Zehnder modulators reported here is another remaining challenge. While not trivial, we anticipate that through more extensive characterization of the electrical properties of BTO, more advanced electrode designs can be used to reach the bandwidth that is necessary for transceiver applications.

In the second part of the thesis, we explored potential applications of BTO-on-Si technology beyond conventional EOMs. We investigated whether BTO can be used in plasmonic modulators to replace the unstable organic materials that are typically used. With a novel fabrication technique we were able to demonstrate high-performance and good stability of BTO plasmonic modulators. We were able to demonstrate data transmission at 72 Gbps using OOK, and 116 Gbps using PAM4. . However, we found that the effective Pockels coefficient of BTO plasmonic modulators to be significantly smaller than in photonic devices. We believe the reason for this discrepancy is related to interface effects and dead layers in the nanostructured BTO, but further investigations are needed for a complete explanation. The performance of BTO plasmonic modulators is also limited by the large insertion loss of the devices. To reduced this loss, a more optimized patterning process is needed which results in a lower roughness, as well as optimized photonic-to-plasmonic coupling.

We also investigated the potential to use BTO in a novel application: cryogenic photonics. Here we measured the electro-optic properties of BTO at cryogenic temperatures for the first time. We found that a strong Pockels effect is preserved down to temperatures of 4 K. Through device demonstrations of low-power tuning and high-speed data modulation at 4 K we showed the BTO can be used to missing functionality to cryogenic PICs. Based on these demonstrations, it would now be possible to use integrated BTO devices in quantum experiments to show the use in real applications such as optical quantum computing.

In conclusion this thesis has served to demonstrate that BTO-on-Si technology has immense potential in various application areas, from data communication to quantum computing, while at the same time provide fundamental insights into the basic properties and behaviors of BTO.

A

LOW-LOSS $BATIO_3$-SI WAVEGUIDES FOR NONLINEAR INTEGRATED PHOTONICS

DOI: https://doi.org/.1021/acsphotonics.6b00350
ACS Articles on Request: http://pubsdc3.acs.org/articlesonrequest/AOR-gNUjxBiu6ZbYsTFxfmvq

Felix Eltes[1], Daniele Caimi[1], Florian Fallegger[1], Marilyne Sousa[1], Eamon O'Connor[1], Marta D. Rossell[2], Bert Offrein[1], Jean Fompeyrine[1], and Stefan Abel[1]

[1]IBM Research – Zurich, Säumerstrasse 4, 8803 Rüschlikon, Switzerland

[2]Electron Microscopy Center, EMPA, Swiss Federal Laboratories for Materials Science and Technology, 8600 Dübendorf, Switzerland

Abstract

Barium titanate ($BaTiO_3$) has become an attractive material to extend the functionalities of the silicon photonics platform because of its large Pockels coefficient of more than 1000 pm/V. $BaTiO_3$ integrated epitaxially on silicon-on-insulator (SOI) substrates can be structured in passive, and electro-optic silicon photonic devices using slot-waveguide geometries, both of which have been demonstrated. However, all devices demonstrated so far suffer from high optical propagation losses of 40 – 600 dB/cm, which limits their performance compared with state-of-the-art silicon photonics devices (<2 dB/cm). Here, we identify the origin of these high propagation losses, and demonstrate a path to fabricate low-loss $BaTiO_3$-Si wave-guides

with propagation losses of only 6 dB/cm. In particular, we identified the thin strontium titanate ($SrTiO_3$) seed layer typically used for the epitaxial deposition of $BaTiO_3$ on silicon as the main source of absorption: When manufacturing slot-waveguide structures, the $BaTiO_3/SrTiO_3$ layer stack is typically exposed to hydrogen, which is incorporated in the $SrTiO_3$ layer, and causes absorption. We demonstrate that a low-temperature anneal is sufficient to remove hydrogen and to achieve low propagation losses in waveguides. Thus, we found a way to eliminate the previously observed showstopper for incorporating functional and highly nonlinear barium titanate films into silicon photonic structures, ultimately enabling ultra-high-speed switches and novel nonvolatile optical silicon photonic devices.

Introduction

Silicon photonics is becoming a mature platform for photonic integrated circuits, benefiting from the processing and fabrication knowledge of microelectronics to realize reliable nanoscale devices. To link the electric and optic domains, in general electro-optical modulators based on the plasma-dispersion effect are used. [132] Although high modulation speeds have been reached in Si modulators [133], the devices typically suffer from relatively large insertion losses and the simultaneous change of the real and imaginary parts of the refractive index. Thus, advanced modulation formats, such as quadrature amplitude modulation (QAM), are difficult to implement. In telecommunication applications, these formats were enabled by exploiting the Pockels effect in $LiNbO_3$ [32, 134], but silicon does not provide this option because of a vanishing Pockels effect [27].

Enabling the Pockels effect on the silicon photonic platform could lead to improved devices in terms of power consumption, insertion losses, and modulation speeds. In addition, it could allow functionalities that cannot be achieved with bulk silicon only, such as ultra-low-power tuning or nonvolatile optical memories. The technical options investigated include the application of strain [135] and the use of silicon-organic hybrid structures [136, 137]. These approaches suffer either from small Pockels coefficients or from low process compatibility due to thermal instability. Heterogeneous integration of inorganic materials is an alternative path to bring a strong Pockels effect to silicon photonics. However, as the integration of high-quality $LiNbO_3$ on silicon is limited to local bonding schemes with low yield or to wafer bonding approaches with a maximum donor wafer size of 6 inch [93, 138], the integration of good electro-optical materi-

als that are compatible with large-scale silicon wafers has recently attracted increased attention.

One promising candidate is barium titanate, a ferroelectric oxide with a strong Pockels effect that can be deposited with high crystalline quality directly on silicon by, for example, molecular beam epitaxy (MBE). [44] As recently demonstrated, $BaTiO_3$ layers on silicon substrates retain a strong Pockels coefficient of $r \approx 150$ pm/V [51] and can be implemented in active and passive silicon photonic structures [48, 49, 77]. A major issue in all demonstrations of hybrid $BaTiO_3$-Si devices so far has been the high propagation losses (α_p) of 40 to >500 dB/cm at the wavelength $\lambda = 1.55$ μm, much larger than the propagation losses below 2 dB/cm [139] of state-of-the-art silicon waveguides. These high propagation losses were not expected because $BaTiO_3$ bulk crystals are transparent at $\lambda = 1.55$ μm. [75] In principle, these good optical properties are maintained in thin films, as shown by the rather low propagation losses of 4 dB/cm in waveguides made from $BaTiO_3$ layers deposited on magnesium oxide substrates. [45] Those results indicate that $BaTiO_3$ thin films do not suffer intrinsically from high propagation losses, but that microstructural effects when grown on silicon, interface effects with silicon, or the processing conditions during waveguide fabrication introduce those high losses.

In this work, we carefully studied various contributions to the propagation losses in hybrid $BaTiO_3$-Si waveguides to ultimately identify and eliminate the reason for the losses. In particular, we used various waveguide geometries, process conditions, and post-fabrication annealing treatments to separate loss channels arising from scattering and absorption in the different materials and at their interfaces.

Typically, $BaTiO_3$-Si waveguides are fabricated as half-way-etched slot-waveguide structures: The waveguide consists of a blanket $BaTiO_3$ film sandwiched between the device Si of an SOI wafer and a patterned top Si layer (Figure A.1a). The slot-waveguide geometry enhances the optical confinement in the $BaTiO_3$ slab, while keeping bending losses low. A critical step in slot-waveguide fabrication is the integration of the top Si layer, which requires several deposition and etching steps.

To disentangle the different origins of optical losses, we measured the propagation losses at various steps during the fabrication of the slot waveguides, using SiO_2 strip-loaded waveguides (Figure A.1b). Our geometry of choice exhibits a similar optical confinement in the $BaTiO_3$ layer as that of the $BaTiO_3$-Si waveguides (Figure A.1). While the confinement factor is

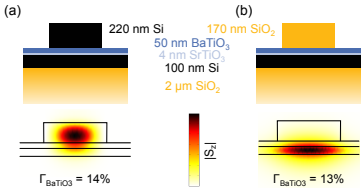

FIGURE A.1: Schematic drawing of (a) the cross section of the target $BaTiO_3$-Si slot-waveguide geometry and (b) the SiO_2 strip-loaded waveguide geometry as used to investigate partially processed structures. For comparison, the magnitude of the Poynting vector of the optical modes is shown, as simulated using COMSOL Multiphysics. The optical confinement (Γ) in $BaTiO_3$ is similar in both structures despite the different layer stacks.

comparable, the bending losses in SiO_2 strip-loaded waveguides are much higher, which prevents the geometry from being used for active photonic applications. However, the simple fabrication process makes these waveguides ideal for investigating propagation losses with-out the influence of processing.

Methods

Waveguide fabrication

The $BaTiO_3$ films used for waveguide fabrication were deposited by MBE on SOI substrates with 100 or 220 nm device silicon using the method reported in [77]. A 4-nm-thin epitaxial $SrTiO_3$ seed layer was grown via MBE prior to shuttered co-deposition of $BaTiO_3$, to ensure good crystalline quality and a low surface roughness of R_{RMS} <0.5 nm. [51, 140, 141] Details of the deposition process are described elsewhere. [77, 142]

We fabricated strip-loaded waveguides on these $BaTiO_3$/SOI substrates by spin coating and patterning 170-nm-thick hydrogen silsesquioxane (HSQ), which trans-forms into SiO_2 when exposed via electron-beam lithography (EBL) (Figure A.1).

For the realization of the compact slot-waveguide structures, we bonded $BaTiO_3$ films grown on SOI substrates with 220 nm device silicon onto SOI wafers with a 100-nm-thick device silicon layer via direct wafer bonding. [53] We used 5-nm-thick Al_2O_3 adhesion layers, deposited by atomic layer deposition (ALD) on both wafers prior to the bonding step. [54] After

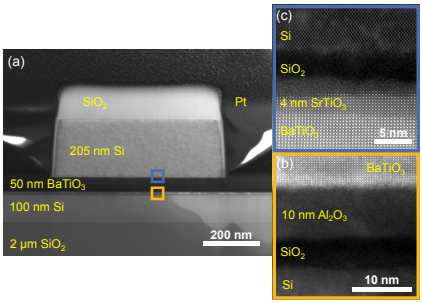

FIGURE A.2: STEM images of a $BaTiO_3$-Si slot waveguide. (a) BF-STEM image showing the full waveguide cross section. The cladding is platinum from the sample preparation. (b) HAADF-STEM image showing the Al_2O_3 interface after wafer bonding. (c) HAADF-STEM image showing the $SrTiO_3$ seed layer.

bonding and annealing at 250°C, the initial MBE growth wafer was removed by grinding and selective wet etching, leaving only the device silicon as a top layer. This layer was thinned during the chemical etching process of the SOI wafer, leaving 205 nm Si. The silicon top layer was then structured using EBL and an HBr/O_2 inductively coupled plasma-etching process to form waveguides (Figure A.2).

Scanning Transmission Electron Microscopy (STEM)

Bright-field STEM (BF-STEM) analysis, including cross sectioning and lamella preparation, were carried out by means of a FEI Helios Nanolab 450S focused ion beam (FIB) operated at an accelerating voltage 30 kV for BF-STEM.

High-angle annular dark field STEM (HAADF-STEM) measurements were performed using a double spherical aberration-corrected JEOL JEM-ARM200F microscope operated at 200 kV. The convergence semiangle was set to 25.3 mrad, and the annular semi-detection range of the annular dark-field detector was set to collect electrons scattered between 90 and 370 mrad.

Optical characterization

We determined the propagation losses in the waveguide structures by measuring the transmission spectrum between 1.5 and 1.6 µm through waveguides with lengths varying from 100 µm to 9 mm. We used the com-

bination of either a tunable laser with a power meter or a superluminescent light-emitting diode with a spectrum analyzer. To extract the propagation losses, α_p, we first corrected for the spectral coupling characteristics of the grating couplers. Then, we linearly fitted the transmission versus waveguide length, using multiple waveguides for each length. As an example, Figure A.5 shows transmission versus waveguide length, and the corresponding fit. The slope of the linear fit gives the propagation losses per unit length. [143] The standard error was estimated based on the variance in losses of multiple (>2) sets of waveguides with the same lengths, combined with the linear fit error.

Chemical characterization

The surface chemistry of $BaTiO_3$ and $SrTiO_3$ films was studied in an ultra-high-vacuum (UHV) XPS chamber with a base pressure of 10^{-9} mBar. The chamber is equipped with a monochromatic Al K_α X-ray source and a Phoibos150 hemispherical analyzer, mounted at 50° take-off angle, defined from the normal to sample surface. Gaussian–Lorentzian line shapes were used for deconvoluting the spectra after Shirley background subtraction.

Results and discussion

To confirm the high propagation losses observed in $BaTiO_3$-Si slot-waveguide structures [48, 49, 77], we reproduced these structures using the fabrication process described above. Indeed, the propagation losses of $\alpha_p = 148 \pm 7$ dB/cm for the TE mode are in agreement with the presence of an unknown loss channel in our structures. In principle, propagation losses can be caused by three different mechanisms: (1) Absorption, (2) scattering at waveguide sidewalls, inter-faces and material defects, and (3) leakage. By careful simulations with well-established optical mode solvers (Phoenix and COMSOL Multiphysics), we were able to exclude radiation losses due to poor light confinement. To separate the contributions originating from absorption and scattering, we then analyzed α_p for differently processed samples, ranging from unprocessed $BaTiO_3$ films to fully processed slot waveguides, as described below.

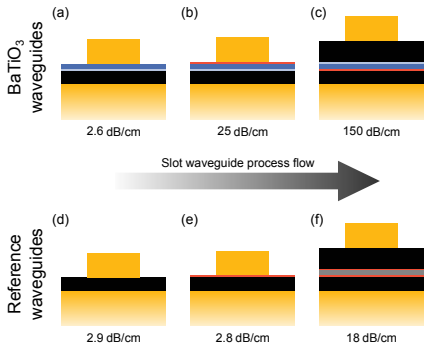

FIGURE A.3: Schematics of waveguide cross sections and propagation losses at different stages during the processing. See Figure A.1 for color scheme, with the addition of Al_2O_3 (red) and Si_3N_4 (gray).

Process related losses

SiO_2 strip-loaded waveguides on $BaTiO_3$/SOI substrates (Figure A.3a) show the same propagation losses (2.6 ± 0.2 dB/cm) as the reference waveguides fabricated without the $BaTiO_3$ layer (2.9 ± 0.2 dB/cm, Figure A.3d). From this comparison, we can conclude that (1) MBE-grown $BaTiO_3$ does not absorb at $\lambda = 1.55$ µm prior to any post-deposition etching, deposition or annealing steps; (2) light-scattering effects in the $BaTiO_3$ layer can be disregarded – in agreement with the high structural quality described above (Figure A.2), and (3) our experiments are limited by propagation losses of $\sim$3 dB/cm due to scattering at the SiO_2 sidewalls, assuming that in our reference waveguide there is only negligible absorption in the SiO_2 and Si layers. [144]

The deposition of Al_2O_3 for wafer bonding increases the losses to 25.3 ± 0.5 dB/cm on $BaTiO_3$ substrates (Figure A.3b), but does not alter the propagation losses of the SOI reference waveguides (2.8 ± 0.3 dB/cm, Figure A.3d). These results indicate that the Al_2O_3 layer itself is transparent, but that a chemical reaction with the $BaTiO_3$ or $SrTiO_3$ layer occurs during the ALD process. One possible reactant is hydrogen, which is formed during the ALD process from H_2O precursors [79]. The strongly reducing hydrogen might create oxygen vacancies in $SrTiO_3$ or $BaTiO_3$, resulting in higher propagation losses. [145]

After fabrication of the $BaTiO_3$-Si slot-waveguide layer stack by bonding a crystalline silicon top layer (Figure A.3c), the propagation losses increase to 154 ± 26 dB/cm, which is in the same range as those of the fully processed wave-guides (Figure A.1a). Here again, we attribute the origin of this strong increase to hydrogen: During the bonding process, excess water is formed, which decomposes into hydrogen when oxidizing the Si below the Al_2O_3 layer. [53, 80] As described above, the hydrogen might react with $BaTiO_3$ or $SrTiO_3$ – in particular because of the increased diffusion into the $BaTiO_3/SrTiO_3$ stack at the elevated temperatures during the annealing process. Reference waveguides with nonabsorbing Si_3N_4 layers [144] instead of the $BaTiO_3$ film (Figure A.3f) show significantly lower propagation losses (18 ± 2 dB/cm). The refractive index of the Si_3N_4 was tuned to a similar value as that of the $BaTiO_3$ layer to ensure the same mode profile. The lower losses in the Si_3N_4 slot wave-guides indicate that possible scattering losses at the bonding interface contribute only slightly to the overall much higher propagation losses of $BaTiO_3$ slot waveguides.

The comparison of different waveguides and process steps provides strong indications that hydrogen induces absorbing defects in the $BaTiO_3/SrTiO_3$ layer stack during the bonding process. Absorption caused by hydrogen exposure is also consistent with the previously observed high losses in $BaTiO_3$-Si slot-waveguide structures fabricated from amorphous silicon (a-Si) top layers deposited via plasma-enhanced chemical vapor deposition (PECVD) [48]: During the deposition of low-loss a-Si, SiH_4 precursors and excess H_2 are used [81, 146], which produces reactive atomic hydrogen during deposition. The dependence of the hydro-gen concentration on the specific process conditions used might also explain the large variations in propagation loss-es observed in the past (40 – 600 dB/cm [48, 49, 77]).

Role of hydrogenation

To confirm the effect of hydrogen exposure, we performed control experiments by explicitly exposing SiO_2 strip-loaded $BaTiO_3$/SOI waveguides to hydrogen plasma. The plasma exposure was performed at 290°C under 80 mTorr pressure and 100 sccm flow of hydrogen with 200 W plasma power in an Oxford FlexAL ALD tool. Identical conditions were used for all hydrogen plasma exposures in this study. Indeed, hydrogen exposure induces propagation losses in the waveguide structures that increase nonlinearly with the process time up to 320 ± 20 dB/cm (Table A.1). The exposure of a SOI reference sample with SiO_2 waveguides to the same conditions

TABLE A.1: Influence of hydrogen plasma exposure on propagation losses in SiO_2-strip-loaded $BaTiO_3$ and Si waveguides.

Waveguide layers	Hydrogen plasma time	Propagation losses [dB/cm]
50 nm $BaTiO_3$/4 nm $SrTiO_3$/100 nm Si/2 μm SiO_2	None	2.6 ± 0.2
50 nm $BaTiO_3$/4 nm $SrTiO_3$/100 nm Si/2 μm SiO_2	40 min	50 ± 3
50 nm $BaTiO_3$/4 nm $SrTiO_3$/100 nm Si/2 μm SiO_2	80 min	320 ± 20
220 nm Si/2 μm SiO_2	None	1.8 ± 0.3
220 nm Si/2 μm SiO_2	80 min	1.7 ± 0.1

showed that the plasma has no influence on the SiO_2 and silicon layers, and confirms that the higher losses are due to the presence of the $BaTiO_3/SrTiO_3$ layer stack in the wave-guide (Table A.1).

While the results of the plasma exposure experiments confirm that exposing $BaTiO_3/SrTiO_3$ to atomic hydrogen induces absorption, they do not reveal whether the absorption is due to the creation of oxygen vacancies or due to another interaction with hydrogen, such as hydrogenation of the materials [147–149]. To investigate the role of oxygen vacancies, we first prepared SiO_2 strip-loaded $BaTiO_3$/SOI waveguides with high propagation losses (>300 dB/cm) using a long hydrogen plasma exposure (same conditions as above), and subsequently annealed the sample in UHV ($<10^{-9}$ mBar) at ∼550°C for 60 min. This UHV annealing step strongly reduced α_p to 49 ± 5 dB/cm, even though oxygen vacancies could not have been cured owing to the low oxygen partial pressure ($<10^{-9}$ mBar). The losses obtained after the UHV anneal can be explained by the presence of two competing processes. First, outgassing of hydrogen strongly reduces the losses induced by the hydrogen plasma exposure. Second, the high temperature and low oxygen partial pressure cause absorbing oxygen vacancies, leading to moderate losses after UHV annealing. In a control experiment, another SiO_2 strip-loaded $BaTiO_3$/SOI sample without prior hydrogen plasma exposure

($\alpha_p \approx 3$ dB/cm) indeed exhibited propagation losses of 90 ± 11 dB/cm after an UHV anneal at a higher temperature (600°C instead of 550°C).

The results of the UHV annealing experiments reveal two important aspects: First, long anneals at low oxygen partial pressure induce propagation losses due to the formation of oxygen vacancies. Second, high propagation losses induced by hydrogen exposure can be strongly reduced through UHV annealing. We assume that the hydrogen outgasses from the $BaTiO_3/SrTiO_3$ layer stack, resulting in reduced propagation losses.

To avoid the formation of oxygen vacancies while out-gassing hydrogen, we finally annealed SiO_2 strip-loaded $BaTiO_3$-Si waveguides with high α_p (>300 dB/cm), from hydrogen plasma exposure, in oxygen at 500°C for 60 min, which resulted in waveguides with $\alpha_p = 2.2 \pm 0.2$ dB/cm. As high-temperature oxygen annealing is not compatible with many complementary metal-oxide-semiconductor (CMOS) fabrication steps, we adjusted the annealing process to more moderate conditions. Ultimately, we were able to successfully outgas hydrogen from high-loss waveguides by annealing in argon ($p_{O2} < 10^{-7}$ mBar) at 350°C, which is compatible with standard CMOS processes. At this annealing temperature, no oxygen vacancies are induced, resulting in 2.6 ± 0.2 dB/cm propagation losses.

Chemical sensitivity to hydrogen

To understand the physical process behind the hydrogen-induced absorption better, we correlated the observed loss-es with chemical information from the uppermost 5 – 10 nm of a $SrTiO_3$ and a $BaTiO_3$-terminated sample via XPS measurements. After exposing the sample to a hydrogen plasma, a much stronger chemical change was ob-served in the $SrTiO_3$ layer than in the $BaTiO_3$ layer. In particular, the Ti 2p peak reveals a significant reduction of Ti^{4+} to Ti^{3+} in $SrTiO_3$, whereas in $BaTiO_3$ the fraction of Ti^{3+} remains unchanged (Figure A.4). These results indicate that the hydrogen selectively reduces the titanium in the $SrTiO_3$ layer, which leads to an increase in the optical absorption.

To verify that the 4-nm-thick $SrTiO_3$ layer is the main source of absorption in our structures, we compared SiO_2 waveguides made using a 50 nm $BaTiO_3$/4 nm $SrTiO_3$ layer stack with waveguides using only a 4 nm $SrTiO_3$ layer. Both stacks where fully oxygenated prior to waveguide fabrication. Assuming that both $BaTiO_3$ and $SrTiO_3$ contribute significantly to the absorption after hydrogenation, one would expect much higher propagation

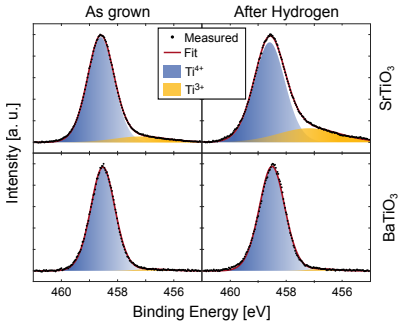

FIGURE A.4: Ti 2p 3/2 XPS spectra of $BaTiO_3$ and $SrTiO_3$ before and after exposure to hydrogen plasma. The lower binding-energy (BE) component corresponds to Ti^{3+} and the higher BE component to T^{i4+}. [82, 83] The fraction of reduced titanium in $SrTiO_3$ doubles after exposure to hydrogen plasma, whereas there is no significant change in $BaTiO_3$. The Ti^{3+} component in unprocessed $SrTiO_3$ can be attributed to oxygen vacancies due to the oxygen-free high-temperature crystallization step during deposition.

losses on the $BaTiO_3/SrTiO_3$ sample because of the high optical confinement factor of 13.2 % in the $BaTiO_3/SrTiO_3$ layer stack. The much lower optical confinement in the $SrTiO_3$ layer (1.4 %) of our $SrTiO_3$-layer-only reference sample would accordingly result in significantly lower losses. However, after a 20-min hydrogen plasma treatment, the propagation losses in both samples increase similarly from 2.6 ± 0.2 dB/cm to 50 ± 3 dB/cm for the $BaTiO_3/SrTiO_3$ sample (Table A.1), and from 4.0 ± 0.5 dB/cm to 81 ± 3 dB/cm in the $SrTiO_3$-layer-only sample. These results show that the main contribution of the propagation losses indeed originates from the 4-nm-thick $SrTiO_3$ layer rather than from the $BaTiO_3$ layer, and confirm the selectivity of the hydrogenation process observed with XPS. Taking into account the optical confinement factor and the overall waveguide losses, we can estimate the losses in the $SrTiO_3$ layer as $\sim 5,000$ dB/cm after 20-min hydrogen plasma exposure. Assuming that the high propagation losses in all $BaTiO_3/SrTiO_3$/Si waveguides are dominated by absorption in $SrTiO_3$, we consistently estimate that the losses in the $SrTiO_3$ layer induced during the slot-waveguide fabrication are more than $10,000$ dB/cm.

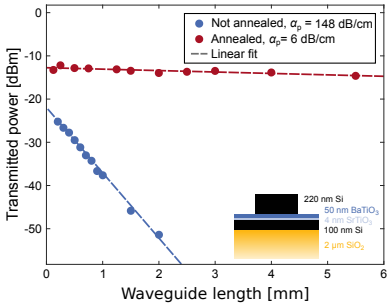

FIGURE A.5: Transmission through slot waveguides of varying lengths, before and after annealing. The plotted values are the average transmitted power through several waveguides with identical length. The inset shows the waveguide geometry.

Fabrication of low loss slot-waveguide structures

Finally, we applied our insights into the loss mechanism and the curing procedure to fabricate low-loss $BaTiO_3$-based slot-waveguide structures. Using the same fabrication scheme as described above, we were able to reduce the propagation losses from initially $\alpha_p = 148 \pm 7$ dB/cm to 6.3 ± 0.9 dB/cm by annealing the waveguides in oxygen at 350°C for 60 min (Figure A.5). The remaining propagation losses are within the typical range of slot-waveguide structures, which generally suffer from scattering effects at the interfaces. [150, 151]

Using this fabrication method, it is now possible to fabricate various optical elements, such as couplers, splitters and interferometers, with a highly nonlinear optical crystal embedded, in silicon photonics. Ring resonators with a radius of 75 µm with well-defined resonances and a quality factor of $Q > 20,000$ (Figure A.6) demonstrate the usability of the $BaTiO_3$-Si hybrid waveguides.

Conclusions

Previous reports on novel $BaTiO_3$-Si hybrid waveguides consistently showed high propagation losses of up to 600 dB/cm. In this study, we identified a strong optical absorption of more than 10,000 dB/cm in the thin $SrTiO_3$ seed layer as the major source of these large propagation losses. The absorption is induced by hydrogen exposure during the integration of the top

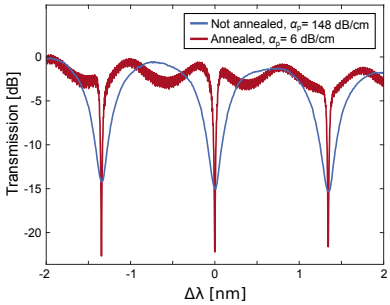

FIGURE A.6: Comparison of ring resonator spectra before and after annealing. The spectra are taken from ring resonators with a 75 μm radius and gap sizes close to critical coupling. The spectra are normalized to account for insertion losses. The corresponding waveguide cross section is shown in the inset of Figure A.5.

silicon layer, which is done by either direct wafer bonding or PECVD. In contrast, absorption effects in the $BaTiO_3$ layer are negligible. We developed CMOS-compatible annealing procedures that fully recover the hydrogen-induced losses and that can be used to obtain low-loss slot-waveguide structures ($\alpha_p = 6$ dB/cm, Figure A.7) and high-Q ring resonator cavities ($Q > 20,000$, Figure A.6). The ability to remove high propagation losses puts renewed focus on a $BaTiO_3$-based photonic technology, and renders

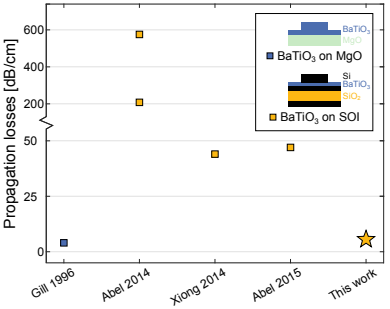

FIGURE A.7: Comparison of previously reported propagation losses in $BaTiO_3$-based waveguides on MgO substrates and on silicon substrates with this work. The waveguides fabricated from $BaTiO_3$ on Si use a slot geometry to achieve enhanced optical confinement in the $BaTiO_3$ layer and to reduce the bending losses. [48, 69, 77]

it very appealing for more advanced silicon photonic structures: It enables novel applications and structures, such as high-speed modulators, non–volatile optical memories, and radio-frequency electric field detectors.

B

LARGE POCKELS EFFECT IN MICRO- AND NANOSTRUCTURED BARIUM TITANATE INTEGRATED ON SILICON

Nature Materials, vol. 18, issue 1, pp. 42-47 (2019)
DOI: https://doi.org/10.1038/s41563-018-0208-0

Stefan Abel[1,*], Felix Eltes[1,*], J. Elliott Ortmann[2], Andreas Messner[3], Pau Castera[4], Tino Wagner[5], Darius Urbonas[1], Alvaro Rosa[4], Ana M. Gutierrez[4], Domenico Tulli[6], Ping Ma[3], Benedikt Baeuerle[3], Arne Josten[3], Wolfgang Heni[3], Daniele Caimi[1], Lukas Czornomaz[1], Alexander A. Demkov[2], Juerg Leuthold[3], Pablo Sanchis[4] and Jean Fompeyrine[1]

[1]IBM Research – Zurich, Säumerstrasse 4, 8803 Rüschlikon, Switzerland

[3]Department of Physics, The University of Texas, Austin, TX, USA

[3]Institute of Electromagnetic Fields (IEF), ETH Zurich, 8092 Zurich, Switzerland

[4]Nanophotonics Technology Center, Universitat Politècnica València, Valencia, Spain

[5]ETH Zurich, Nanotechnology Group, Rüschlikon, Switzerland

[6]DAS Photonics, Universitat Politècnica València, Valencia, Spain

*These authors contributed equally to this work

ABSTRACT

The electro-optical Pockels effect is an essential nonlinear effect used in many applications. The ultrafast modulation of the refractive index is, e.g., crucial to optical modulators in photonic circuits. Silicon has emerged as a platform for integrating such compact circuits, but a strong Pockels effect is not available on silicon platforms. Here, we demonstrate a large

electro-optical response in silicon photonic devices using barium titanate. We verify the Pockels effect to be the physical origin of the response, with $r_{42} = 923$ pm/V, by confirming key signatures of the Pockels effect in ferroelectrics: The electro-optic response exhibits a crystalline anisotropy, remains strong at high frequencies, and shows a hysteresis upon changing the electric field. We prove that the Pockels effect remains strong even in nanoscale devices, and show as a practical example data modulation up to 50 Gbit/s. We foresee our work to enable novel device concepts whose application area largely extends beyond communication technologies.

INTRODUCTION

Silicon photonics has become a platform for dense and low-cost integrated photonic circuits for a wide range of applications [132, 150, 152–154], all of which require fast, energy-efficient electro-optical (EO) switches. State-of-the-art modulators based on silicon [155] rely on the plasma dispersion effect [27] and have two major constraints: First, the change of the real and imaginary parts of the refractive index is linked. A modulation of only the optical phase is therefore not possible, which renders the use of advanced modulation formats difficult [156, 157]. Second, the operating speed is limited by the charge-carrier lifetimes in forward-biased devices or by the RC characteristics in reversed-biased devices [29], leading to a maximal bandwidth of a few tens of GHz. These constraints are not present in discrete modulators that exploit the Pockels effect in lithium niobate ($LiNbO_3$, LNO) single crystals, which have been used for decades in long-haul telecommunication [158]. Because no Pockels effect exists in a centrosymmetric crystal such as silicon, materials with sizeable Pockels coefficients must be integrated onto silicon photonic structures to combine the benefits of bulk Pockels modulators with the low fabrication costs of integrated silicon photonics. Unfortunately, so far, no satisfactory solution exists. The integration of LNO on silicon can only be performed locally [159] or on small wafer scales [93] because no epitaxial deposition process is available. Organic materials with large Pockels coefficients have been integrated on silicon and show high-speed performance [160, 161]. Unfortunately, their limited range of operating temperatures hinders their use in real applications. Lead zirconate titanate (PZT) thin films, a more stable material, have also been used to fabricate active switches on a SiN waveguide platform [92], but no direct integration on compact silicon photonics has been achieved.

Barium titanate ($BaTiO_3$, BTO) has emerged as an excellent candidate to enable Pockels-effect-based devices on silicon for several reasons. First, BTO has one of the largest Pockels coefficients of all materials [162]. Second, it has previously been used in thin-film EO modulators on exotic oxide substrates [163, 164]. Third, BTO can be grown on silicon substrates [51, 165] with large wafer sizes, and with an excellent crystal quality [166]. Previous work reported values of the Pockels coefficients lower than BTO bulk values, but five times larger than bulk LNO [51]. Fourth, BTO is a chemically and thermally stable material. Finally, functional passive photonic structures, such as low-loss hybrid BTO-Si waveguides, have already been realized [95]. Earlier results were shown on EO switching in BTO-Si waveguides [48, 49, 166] or in BTO plasmonic devices operated at high speed [167], but the influence of undesired effects, such as charge migration or plasma dispersion, could not yet be excluded as the source of the EO response. No proof exists that BTO maintains its superior EO properties when embedded into micro- and nanoscale silicon photonics structures.

In this work, we unambiguously prove the presence of the Pockels effect in BTO integrated into silicon photonic devices by verifying three independent criteria: We show, first, high-speed modulation up to frequencies of 65 GHz, second, the dependence of the EO response on the orientation of the optical and externally applied electrical fields relative to the crystalline orientation of BTO, and third, optical evidence of ferroelectric domain switching. These features are unique signatures of the Pockels effect and exclude other physical switching mechanisms. We extract a Pockels coefficient of $r_{42} \sim 923$ pm/V, which is 30 times larger than in LNO, and the highest value reported in silicon photonic structures.

In the following sections, we first disclose the fabrication of the layer stack containing ferroelectric BTO, in which the Pockels effect is present. Next, we describe the layout and the design of both microscale photonic and nanoscale plasmonic devices used to verify the presence of the Pockels effect. We discuss the need of using two complementary device geometries to fully characterize the EO properties of BTO, as presented in detail in the third section. Finally, we demonstrate the generic applicability of BTO-enhanced photonic structures by performing data modulation at high rates of up to 50 Gbit/s.

FABRICATION OF BTO LAYERS

In this section, we show that high-quality, single-crystalline BTO on SiO_2 can be obtained using a combination of epitaxy and direct wafer bonding. With our concept, two prerequisites to enable EO switching in BTO/Si structures are fulfilled: First, the approach yields dense, crystalline, and tetragonal BTO films, which are needed to preserve the Pockels effect [66]. Second, it enables a thick lower cladding below the BTO films, which is required to avoid optical leakage into the substrate. Previous electro-optical BTO/Si devices were based on BTO on silicon-on-insulator (SOI) substrates [48, 49]. However, in such layer stacks, mobile charges in the semiconducting device silicon layer may screen the applied electric field and result in an EO response due to plasma dispersion [162]. To prevent this effect, we fabricated a hybrid amorphous-epitaxial heterostructure without any silicon below the BTO layer using a two-step process.

In the first step, 80- to 225-nm-thick BTO layers are grown by molecular beam epitaxy (MBE) on SOI substrates. To ensure epitaxial growth, the SOI is covered with a 4-nm-thin MBE-grown strontium titanate ($SrTiO_3$, STO) buffer layer [51] (Methods). In the second step, we transfer the BTO layer onto another silicon wafer covered with SiO_2 via direct wafer bonding and substrate back-etching, using Al_2O_3 as bonding interface [168]. The 5- to 10-nm-thick Al_2O_3 layer deposited on both the host and the donor wafer via atomic layer deposition guarantees a high bonding strength [169]. The low surface roughness below 0.4 nm for both wafers (Figure B.1a) results in a high bonding yield. After thermal treatment, the donor wafer is removed via grinding and multiple etching steps (Methods), resulting in the desired wafer stack of $Si/STO/BTO/Al_2O_3/SiO_2/Si$ (Figure B.1b). Most of these steps are commonly available in a back-end-of-the-line integration process and enable the addition of functional oxide layers with planarized, oxide-covered wafers fabricated in a standard CMOS process [166].

The layers show a well-defined crystalline orientation with respect to the wafer as is necessary for obtaining high-performance photonic devices [70]. The crystallinity and interfaces remain of high quality after completion of the process, as is visible at a microscopic level in high-resolution scanning transmission electron microscopy (HRSTEM) images (Figure B.1c). High-resolution X-ray diffraction (HRXRD) analysis confirms the cube-on-cube epitaxial relationship between the BTO layer and the device silicon layer (Figure B.1d). The sharp rocking curve (Figure B.1e) further confirms the high crystalline quality at a macroscopic level.

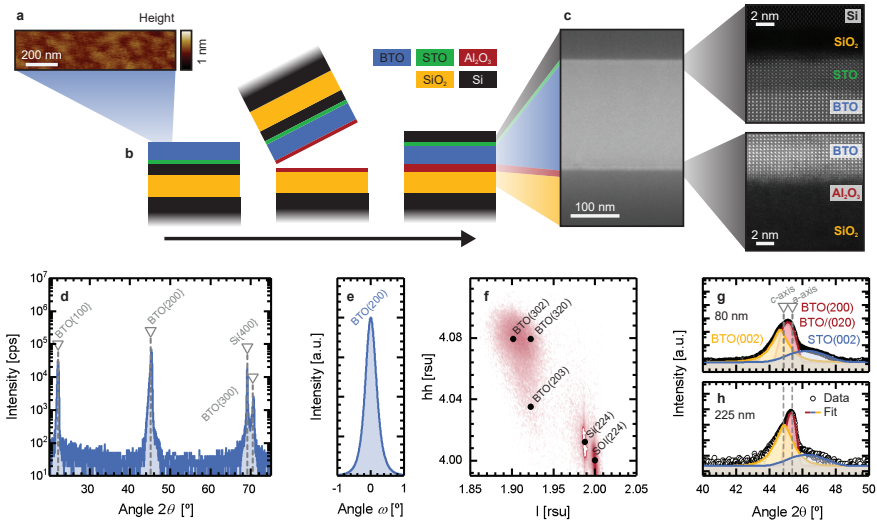

FIGURE B.1: Fabrication process and structural characterization for a hybrid crystalline-amorphous BTO-SiO_2 heterostructure. a, Atomic force microscopy image showing the low roughness of BTO prior to the bonding process. b, Schematic of process (from left to right) to obtain the hybrid stack using direct wafer bonding of an MBE-grown BTO film onto a thermally oxidized acceptor wafer with Al_2O_3 as a bonding interface. c, The low-resolution cross-sectional image shows a uniform and smooth layer stack, whereas the higher-resolution HRSTEM images (right) reveal the high quality of the crystalline structure of BTO and of the BTO/STO interface formed during the deposition process (top) as well as the sharpness of the bonding interface (bottom). d, The HRXRD diffractogram confirms the absence of any polycrystalline domains in the final hybrid stack, with only BTO (h00) peaks visible (pseudo-cubic notation), and the epitaxial relationship between silicon and BTO. e, The high quality of the BTO layer is evidenced by the low mosaicity ($\Delta\omega \approx 0.3°$) extracted from the rocking curve measured on the BTO (200) Bragg peak. f, Reciprocal space map plotted in reciprocal space units (rsu) around the {224} silicon and {203} BTO Bragg peaks acquired on the hybrid stack. Three possible orientations are revealed, with the long *c*-axis being parallel to either the [001] (*c*-axis domains) or to the [110] or [-110] silicon directions (*a*-axis domains). g, h, Higher-resolution diffraction around the pseudo-cubic (200) BTO peak, highlighting the relative contributions of the a- and *c*-axis domains in the BTO layer. The comparison of (g) an 80-nm-thick and (h) a 225-nm-thick BTO layer shows the higher relative fraction of the *c*-axis domain in thinner films.

A more detailed analysis shows that the BTO film has a tetragonal symmetry, consistent with the bulk unit cell of BTO, with two short a-axes and one longer *c*-axis (Figure B.1f). The orientation of these axes is critical for device operation because of the strong dependence of the Pockels effect on the relative orientation of the static electric field, the direction and polarization of the light, and the crystalline orientation [51, 70]. The reciprocal space map around the BTO(203) film peak (Figure B.1f) shows the presence of two types of *a*-axis-oriented domains which are rotated by 90° in-plane relative to each other, and a smaller fraction of *c*-axis domains (see Figure B.1 caption). The *c*-axis domains stem from epitaxial strain, and are expected to form at the interface between STO and BTO [51, 67]. Consistently, the relative volume fraction of *c*-axis domains is indeed larger in the 80-nm-thin film (Figure B.1g) than the 225-nm-thick film (Figure B.1h).

DEVICE INTEGRATION & CHARACTERIZATION

To confirm the Pockels effect in the BTO layer, we test the anisotropy and the frequency behavior of the electro-optic response of various integrated devices. We use racetrack resonators with differently oriented straight sections relative to the BTO crystalline axes (Figure B.2a). The relatively small footprint of such structures of $\sim(100\ \mu m)^2$ allows the fabrication of many separate devices of different orientation, which are needed to probe the angular dependence of the electro-optic response. Resonant devices are well-studied and allow a quantitative analysis of the EO response [170]. Due to the finite photon lifetime, the electro-optic bandwidth of resonant photonic devices is typically limited to few tens of GHz [171], which restricts the usage of such devices for high-speed characterization as needed to validate the Pockels effect. Mach-Zehnder modulators (MZM) can be operated at high-speed without bandwidth limitations due to finite photon lifetimes. However, the larger size of MZMs of several millimeters impacts the electrode bandwidth [29]. Advanced radio frequency (RF) engineering of travelling wave electrodes is required to obtain high-bandwidth BTO/Si based MZM structures. As an alternative, plasmonic phase modulators offer extremely high bandwidth due to the low capacitance resulting from the small device size [101]. In our work, we use such BTO-based plasmonic structures to extend the frequency range of our EO characterization to 65 GHz. Since an accurate quantitative analysis of plasmonic phase modulators is not possible (Supplementary Note 1), we used both photonic and plasmonic device types for our analysis of the electro-optic response.

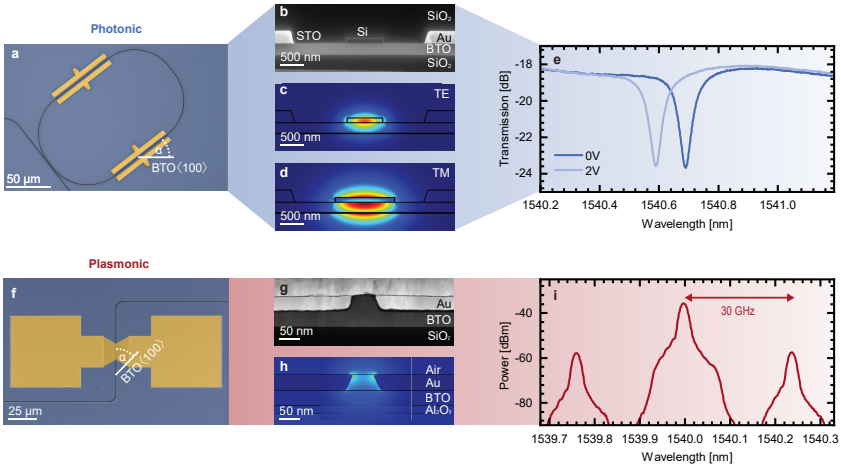

FIGURE B.2: Layout of the photonic and plasmonic devices. a, False-color optical microscopy image of a photonic ring resonator prior to the fabrication of contact pads. The angle α indicates the orientation of the straight section relative to the BTO<100> axis (pseudo-cubic notation). Waveguides are shown in black, the BTO surface in blue, and the electrodes in yellow. b, Scanning electron microscopy (SEM) cross-sectional image of the photonic devices between the electrodes. c, d, Simulated mode profile of the photonic TE and TM mode, respectively (methods). The colors indicate the electric field strength, ranging from blue (low) to red (high). e, Exemplary transmission spectra of a photonic racetrack resonator for two different bias voltages. The EO response is calculated based on the shift of the resonance wavelength. f, g, h, Similar figures as a-d for the plasmonic device, showing the false colored top-view reordered via SEM, the cross section, and the simulated mode profile (same color code as in c, d). i, Example of a transmission spectrum of a plasmonic phase modulator operated at a wavelength $\lambda = 1540$ nm with an RF signal at 30 GHz. The intensity ratio of the peak ($\lambda = 1540.00$ nm) to the first sidebands ($\lambda = 1539.75$ nm and 1540.24 nm) is used to determine the change of the effective index Δn_{eff} of the plasmonic mode.

We have therefore fabricated both photonic and plasmonic devices with embedded BTO (Methods). For photonic structures, the device-silicon layer is used to form strip-loaded waveguides cladded with SiO_2. The waveguide is single-mode and supports transverse-electric (TE) (Figure B.2c) and transverse-magnetic (TM) (Figure B.2d) polarizations with 39 % (TE) or 55 % (TM) of the optical power confined in the BTO layer. Electrodes separated by 2 µm from the waveguide generate an electric field parallel

to the 225-nm-thick BTO layer (Figure B.2a,b, Supplementary Note 2). To analyze the tensorial nature of the EO response, racetrack resonators were fabricated with different angles α relative to the BTO<100> pseudo-cubic crystalline direction (Figure B.2a). Applying a DC or RF signal to the electrodes (Figure B.2e), the shift in the resonance wavelength of the resonators is used to determine the change of the effective mode index Δn_{eff} in the waveguides (Methods).

The 10-μm-long plasmonic structures are based on an 80-nm-thick BTO layer, from which a 50-nm-wide fin is etched and contacted (Methods). The plasmonic waveguide (Figure B.2f,g) confining 50 % of the optical power in the BTO layer (Figure B.2h) [172] is coupled to photonic waveguides via tapered structures (Supplementary Note 3). We derive Δn_{eff} from the power ratio between spectral bands (Figure B.2i), which are created by two-wave mixing processes when applying an RF signal to the electrodes (Methods).

CONFIRMATION OF POCKELS EFFECT

To confirm the presence of the Pockels effect in BTO, it is crucial to analyze characteristic features of the EO response [173], primarily its frequency dependence to exclude slow EO effects and its anisotropic nature to rule out isotropic EO effects. In addition, the Pockels effect in a ferroelectric should translate into a hysteretic response of the refractive index versus field, consistent with the poling of ferroelectric domains. Here we investigate all these characteristics to confirm the presence of the Pockels effect in our devices.

The modulation of the refractive index at radio frequencies [174] differentiates the Pockels effect from the thermo-optic effect and from ionic diffusion processes, both of which occur at long timescales. We measure a constant EO response up to 30 GHz in photonic devices with Q-factors of $Q = 5 \times 10^3$ (Figure B.3a), which coincides with the cut-off frequency of our experimental equipment (Methods, Supplementary Figure S22). Due to the finite photon lifetime [171] and peaking effects [175] in resonant structures, the response at higher frequencies cannot be interpreted unambiguously. From the constant EO response up to 30 GHz in photonic devices, we cannot completely exclude a possible contribution of plasma dispersion induced by the strong electric field in the silicon strip above the BTO layer. Non-resonant plasmonic devices, where silicon is absent in the active region, are used to extend the analysis to higher frequencies. Indeed,

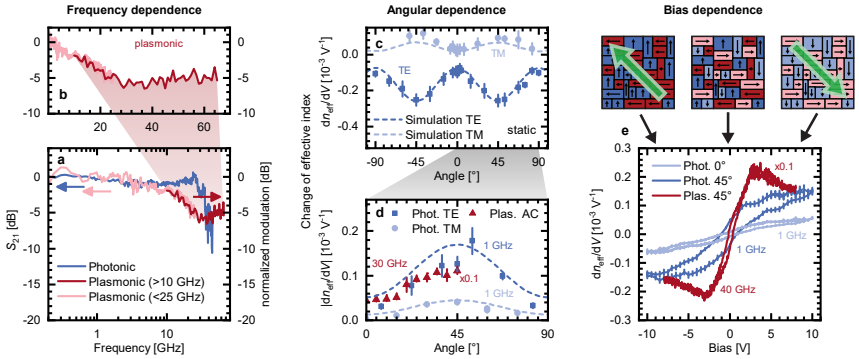

FIGURE B.3: a, Frequency dependence of the EO response of a photonic ring modulator (TE polarization) and a plasmonic phase modulator. b, Linear zoom into the high-frequency region of the plasmonic modulator up to 65 GHz. c, Angular dependence of the EO response of photonic devices designed for different optical polarizations for static electric fields and, d, for photonic and plasmonic devices at alternating electric (AC) fields at 1 GHz and 30 GHz, respectively. The dashed lines in c and d correspond to the simulated response of the photonic devices using the Pockels tensor extracted from the experiments (Supplementary Note 5). e, EO hysteresis curve obtained at 1 GHz (photonic devices, TE polarization) and at 30 GHz (plasmonic devices) when sweeping the applied bias in devices oriented at different angles α (see labels). The schematics on top indicate the orientation of the ferroelectric domains for the electric field (green arrow) oriented at α=±45°.

the EO response in plasmonic devices is constant in the frequency range from 30 to 65 GHz (Figure B.3a), and unambiguously supports the presence of the Pockels effect in the BTO-based devices.

In contrast to the flat frequency response of the photonic devices, the plasmonic modulators show a reduction of the EO response in the frequency range from ∼2 to 30 GHz by ∼5 dB (Figure B.3b). This reduction is attributed to the mechanical boundary conditions in plasmonic devices: At frequencies up to few GHz, horizontal deformation of the BTO fin driven by the piezo-electric effect [176] results in a larger, un-clamped EO response [38] compared to the high frequency region. Such effect is not visible in photonic devices, where mechanical motion is suppressed due to clamping from the SiO_2 cladding (Supplementary Note 4).

Because of the tensorial nature of the Pockels effect [38], the orientation α of the waveguides (defined in Figure B.2) should influence the EO response. Indeed, photonic racetrack devices show a clear dependence on α (Figure B.3c). As the electric-field-induced Δn_{eff} parallel and perpendicular to the BTO layer is anisotropic, the EO response is expected to be sensitive to the polarization of the optical mode. We experimentally confirmed such an anisotropy between the TE and the TM modes in photonic devices (Figure B.3c,d), and compared it with simulations (Supplementary Note 5) of the expected EO response. The experimental angular dependence and polarization dependence of the EO response agree quantitatively with the simulations (Figure B.3c). We determined the two largest non-vanishing coefficients of the Pockels tensor in the BTO layer in the photonic structures to be $r_{42} = (923 \pm 215)$ pm/V and $r_{33} = (342 \pm 93)$ pm/V. Owing to the small response of the TM devices at $\alpha = 0°$, no reliable extraction of the r_{13} coefficient is possible (Supplementary Note 6). The similar angular dependences of the EO modulation at static and radio frequencies indicate a common and constant physical effect as the origin of the EO response at all time and length scales probed in our measurements (Figure B.3d). Here, we limited the analysis to 1 GHz to minimize the influence of finite photon lifetimes on the angular dependence (Supplementary Figure S21). Our experimental procedure does not allow an accurate quantitative analysis of the Pockels response at RF (Methods). However, the flat frequency response of the S_{21} parameter in the photonic devices (Figure B.3a) indicates a constant Pockels effect from static (Figure B.3c) to high frequencies (Figure B.3d).

Although we can measure an effective, orientation-dependent materials response in plasmonic devices, which qualitatively agrees well with the tensorial nature of the Pockels effect (Figure B.3d, Supplementary Note 1), it is not possible to deconvolute and quantify the Pockels coefficients as can be done for photonic devices. Nanoscale plasmonic devices are more sensitive to extrinsic effects such as process damages or device geometry as well as intrinsic effects such as dead dielectric layer, or distribution of *c*- and *a*-axis domains in the plasmonic waveguide. Nevertheless, taking these effects into account, the measured effective response of the plasmonic devices can be reproduced using the Pockels coefficients determined on the photonic devices (Supplementary Note 1).

In addition to the high-frequency response and the angular dependence, the EO response caused by the BTO layer should lead to a hysteretic behavior when sweeping the bias voltage due to the reorientation of ferroelectric domains. Because the Pockels effect is a linear EO effect, domains with

opposing ferroelectric orientations induce an opposite phase shift, resulting in a vanishing EO response for films with equally distributed domains [51]. The EO response will saturate while increasing the bias, once all domains are polarized in the same direction. Indeed, the expected hysteresis is clearly visible in both the microscale photonic and nanoscale plasmonic devices (Figure B.3e). The coercive field E_c extracted for photonic devices ($E_c = 2 \times 10^5$ V/m) is in good agreement with previously reported values for BTO films on silicon of similar thicknesses [51]. In contrast, the coercive field in plasmonic structures is more than one order of magnitude larger ($E_c = 1 \times 10^7$ V/m), but remains consistent with a voltage drop over an interfacial non-ferroelectric layer (Supplementary Note 1) and common observations in thin ferroelectrics, where domain pinning and finite depolarizing fields enhance E_c in devices with reduced dimensions [177].

In the case of photonic devices, the hysteresis loop is not completely pinched at larger voltages due to slow ionic diffusion processes occurring at time scales similar to the sweeping rate used during the hysteresis measurements (Methods, Supplementary Note 7). These diffusion effects are related to the surface reactivity of the bonded material stack towards the ambient atmosphere, which take place in the gap between the electrode and the waveguide. As a consequence, the potential distribution within the device is slightly modified without impacting the angular dependence and the frequency response as discussed above (Supplementary Note 7).

APPLICATION OF THE POCKELS EFFECT

Having demonstrated the existence of a strong Pockels effect in our structures, we now demonstrate its potential use for high-speed data communication (Figure B.4). Recording an eye-diagram is an insightful way to evaluate the performance of an EO modulator. A photonic ring modulator with Q-factor $Q = 9 \times 10^3$ and a 10-μm-long plasmonic phase modulator with a slot width of 50 nm are used to achieve a high modulation bandwidth (Methods), with data rates of 40 Gbit/s (photonic device, see Supplementary Figure S24 for eye diagrams at lower data rates) and 50 Gbit/s (plasmonic device). These results show the applicability of the BTO/Si technology for high-speed data transmission. They can also be used to estimate the performance of MZM, which, if well-engineered, are commonly preferred over resonant structures or phase modulators for integrated optical links. The electro-optic response measured in our TE photonic waveguides translates to a $V_\pi L$ product of 0.45 V·cm (Supplementary Note 8), which is

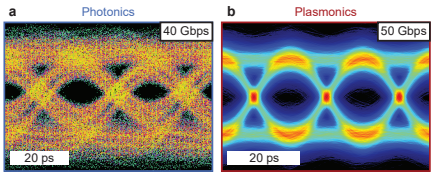

FIGURE B.4: a, Eye diagram for data rates of 40 Gbit/s (photonic device) and b, of 50 Gbit/s (plasmonic device).

competitive with state-of-the-art integrated Si [15] and InP [178] EO phase shifters. Additionally, we estimated the switching energy of an optimized MZM (Supplementary Note 8) to be 96 fJ/bit, which is in the same range as advanced Si-based Mach-Zehnder modulators [12, 78]. These performance metrics prove the technological relevance of having the Pockels effect available on silicon as an EO switching mechanism.

SUMMARY AND CONCLUSION

We have unambiguously demonstrated the presence of the Pockels effect in a hybrid $BaTiO_3$-SiO_2 stack integrated into photonic and plasmonic structures on silicon. While the photonic resonator devices allow for the quantitative determination of the individual Pockels tensor elements of BTO, the plasmonic devices enable bandwidth measurements at frequencies up to 65 GHz. The results from these two complementary device structures demonstrate that BTO maintains its superior electro-optical properties after fabrication of both microscale photonic and nanoscale plasmonic components. Key characteristics, such as the high-speed response, the angular anisotropy, and hysteretic switching, rule out other physical effects as the origin of the EO response. The magnitude of the EO response is bulk-like [38] and many times larger than for any Pockels materials previously integrated on silicon [51, 159, 161]. The chemical and thermal stability of oxides also outperform those of organic nonlinear materials [100, 161]. The use of our structures for data communication at rates of 50 Gbit/s reveals the prospects of this technology for a new class of integrated modulators. Our approach can deliver devices with a competitive $V_\pi L$, is suited for complex modulation formats, and is compatible with a tight integration within CMOS fabrication lines. Having demonstrated the presence of the Pockels effect in the materials stack, we foresee that superior electro-optical performance can be obtained by further optimization of the device parame-

ters such as the thickness of the BTO layer, the gap between the electrodes, and the electrode layout optimized for RF operation. The ability to control the Pockels effect in integrated photonic devices also has profound implications for applications beyond data communication. Sensory [154, 179, 180], mid-infrared [181], and neuromorphic computing applications [107, 152, 153] would also strongly benefit from devices that are operated at reduced operating speeds or exploit non-volatile EO effects. Ultimately, hybrid BTO/Si photonic devices provide an additional degree of freedom for designers to realize not only a new generation of compact, high-speed modulators, but also novel devices such as ultra-low-power tuning elements [49], non-volatile optical memories [182], or microwave-to-optical quantum converters [124].

METHODS

Fabrication of BTO layers

MBE deposition

MBE deposition was done in a chamber with a base pressure of $<3 \times 10^{-10}$ Torr. Before BTO deposition on 2" SOI wafers with 100- or 220-nm-thick device silicon layers, a 4-nm STO seed layer was deposited. After HF-cleaning of the substrate, 0.5 mono layers of Sr was deposited at 600-650°C. After cooling to 50°C, the Sr was oxidized in molecular oxygen, followed by the deposition of amorphous STO at an O_2 pressure of $\sim 5 \times 10^{-7}$ Torr. The amorphous STO was crystallized by annealing in UHV at 400-500°C, resulting in epitaxial STO. BTO growth was done at 500-600°C under atomic oxygen. A plasma source was used to generate atomic oxygen at a pressure of $\sim 5 \times 10^{-6}$ Torr.

Bonding

Direct wafer bonding was performed using 5- to 10-nm-thick Al_2O_3 layers deposited by atomic layer deposition on both donor and receiver wafers. After surface preparation and bonding, an annealing step was performed at 250°C. The donor wafer was removed by grinding, followed by wet etching, leaving the device Si of the SOI donor wafer as the top layer.

Device fabrication

Photonics

Fabrication of photonic devices started by epitaxial deposition of 225-nm BTO on a 4-nm STO buffer on an SOI wafer with 100-nm top Si. The BTO and top-Si layers were transferred by direct wafer bonding to a high-resistivity wafer with a 2-μm-thick thermal oxide. Photonic waveguides and grating couplers were fabricated by patterning the top Si layer using inductively coupled plasma (ICP) etching. After waveguide fabrication, the devices were annealed in O_2 at 400°C for 4 h to reduce propagation losses to ∼10 dB/cm (Supplementary Note 9). Electrodes were deposited in a metallization step. An SiO_2 cladding was deposited by PECVD, in which vias were etched by ICP followed by the final metallization. The width of the waveguides was chosen to be 0.75 and 1.25 μm to ensure single-mode TE and TM operation, respectively. Single mode operation was verified by simulating the 2D mode profiles with PHOENIX and COMSOL. Racetrack resonators with 50 μm (TE) and 75 μm (TM) bend radius, and 75-μm-long straight sections were fabricated along with ring modulators with varying radii.

Plasmonics

The photonic components of the plasmonic devices were fabricated in the same way as the photonic devices (using 80-nm BTO deposited on an SOI wafer with 220-nm top Si). After patterning of photonic regions, the plasmonic waveguides were etched into the BTO using ion beam etching. After structuring of the BTO, the electrodes were deposited by a self-aligned metallization process. The propagation losses of the plasmonic structures are ∼1.4 dB/μm (Supplementary Note 9).

Device characterization

Photonics

Optical fibers and integrated grating couplers were used to first couple light emitted from a tunable diode laser at a wavelength of λ ∼1550 nm into the active devices, and afterwards out of the chip to detect the transmitted power. Applying a voltage to the electrodes creates an electric field in the BTO layer (Supplementary Note 2), which results in a modification of the refractive index because of the Pockels effect. For photonic devices,

we tracked these modifications by recording the transmission spectra of the resonators as a function of the bias voltage applied. The change of the refractive index of the BTO layer can be determined from the change of the resonance wavelength λ_0 (Supplementary Note 10). For hysteresis measurements, we iteratively changed the bias and recorded transmission spectra with a delay of $\sim$10 s. We acquired the frequency dependence of the EO response by modulating the applied voltage from 50 MHz to 40 GHz. We recorded the S_{21} parameter of a TE ring modulator with a radius of 15 μm using a vector network analyzer (VNA) while scanning λ across the resonance and measuring the modulated optical power at a high-speed detector with a 3 dB cut-off frequency of 33 GHz (Supplementary Note 10, Figure S22) after amplifying, filtering, and attenuating the modulated signal (Supplementary Note 10, Figure S19). Note that the values reported for the S_{21} parameters (Figure B.3b) are extracted off-resonance to minimize effects from the finite photonic lifetime on the EO bandwidth (Supplementary Note 10, Figure S21). The nonlinear distortion of the EO response by the erbium-doped fiber amplifier (EDFA) operated close to saturation is considered in the data analysis, but results in inaccuracies which prevent an accurate quantitative analysis of the change of the refractive index from the S21 parameters (Supplementary Note 10).

Plasmonics

To characterize the plasmonic phase shifters, we applied a bias voltage of about 2.5 V and an RF signal of approximately 10 dBm at frequencies f_{RF} between 15 and 65 GHz directly to the electrodes of the phase shifters, and recorded the optical spectrum using an optical spectrum analyzer (OSA). The modulation amplitude was measured as the power ratio between the optical carrier and the modulation sidebands at $f_0 \pm \Delta f_{RF}$. We calibrated the RF power at the input of the RF probe and subtracted the losses of the probe based on the data sheet supplied. To measure the frequency response of plasmonic devices at frequencies lower than 15 GHz, a lightwave component analyzer was used to record the S_{21} parameter of a Mach-Zehnder modulator consisting of two plasmonic phase shifters between 100 MHz and 25 GHz. The overlap between the S_{21} parameter and the phase shifter modulation in the 15-25 GHz range was used to normalize the phase-shifter modulation to the S_{21} parameter.

Datacom experiments

Photonics

A TE photonic ring modulator with a radius of 12.5 μm, a coupling gap of 0.35 μm and an electrode gap of 2.75 μm was used to characterize the high-speed data-transmission capability, whereby an NRZ pseudorandom binary sequence (PRBS) of length $2^7 - 1$ delivered by a bit pattern generator (BPG) was applied, connected to an external clock. The modulating signal was applied by high-speed ground-signal-ground (GSG) RF probes to the electrodes. The modulated optical signal was then optically amplified by an EDFA, filtered via an optical filter, and finally photo-detected prior to its visualization at the digital communication analyzer (DCA). In this way, a 40-Gbit/s signal was generated (Supplementary Note 10, Figure S23).

Plasmonics

A plasmonic phase shifter with a 50-nm-wide and 10-μm-long plasmonic waveguide was used for BPSK data modulation. An electrical 50 Gbit/s signal was generated and amplified before being applied to the modulator. The applied RF voltage peak was 0.8 V at a 50 Ω system, and the DC bias voltage was 2.5 V. A tunable laser, set to 1.55 μm, amplified through an EDFA to 16 dBm was used for the optical input. After the modulator, the optical signal was re-amplified through an EDFA, fed to an optical coherent receiver and recorded by a digital sampling oscilloscope (DSO, 160 GSa/s, 63 GHz 3-dB bandwidth). The digitized signal was processed offline, including timing recovery, carrier recovery, least mean square (LMS) equalization, symbol decision and error counting (Supplementary Note 11, Figure S24).

Simulations

Photonics

All simulations are performed with a MEEP Finite Difference Time Domain (FDTD) solver. The calculations were performed using 2D FDTD with the cell size of 8 : 6 μm ($y : z$) using 33-nm grid size and 1-μm-thick perfectly matched layer (PML) boundary conditions. The simulation geometry consisted of a SiO_2 bottom layer, 225-nm BTO, and a 100-nm-thick and 1250/750-nm-wide Si ridge layer cladded with air. The Gaussian-shaped source was positioned in the center of the waveguide, and the size of the

source was equal to the dimensions of the waveguide (width = 750/1250 nm, height = 325 nm). The wavelength range was set to 1430 – 1670 nm. The simulated EO response of the photonic devices was compared with the experimental data to extract the elements of the Pockels tensor (Supplementary Note 5 and 6).

Plasmonics

All simulations were performed with COMSOL Multiphysics. Eigenmodes were calculated in 2D Finite Element Method (FEM) simulations with a simulated region of 500 : 2000 nm^2 (width:height) and five mesh cells per effective wavelength in the simulated materials. The metal surface was meshed with 1.5-nm vertex spacing. First-order scattering boundary conditions were used. The simulation environment consisted of a 1000-nm SiO_2 bottom layer, 20-nm Al_2O_3, 76-nm BTO, 38-nm BTO slab and metal electrodes, and 1000-nm air cladding. The geometry was adapted to the TEM imaging of devices as fabricated and characterized. Simulations were performed at $\lambda = 1550$ nm; material data obtained from ellipsometry was used for BTO and Au (Supplementary Note 1).

C

A $BaTiO_3$-BASED ELECTRO-OPTIC POCKELS MODULATOR MONOLITHICALLY INTEGRATED ON AN ADVANCED SILICON PHOTONICS PLATFORM

DOI: https://doi.org/10.1109/JLT.2019.2893500

Felix Eltes[1], Christian Mai[2], Daniele Caimi[1], Marcel Kroh[2,3], Youri Popoff[1,4], Georg Winzer[2], Despoina Petousi[2], Stefan Lischke[2], J. Elliott Ortmann[1,5], Lukas Czornomaz[1], Lars Zimmermann[2,6], Jean Fompeyrine[1], Stefan Abel[1]

[1]IBM Research – Zurich, Säumerstrasse 4, 8803 Rüschlikon, Switzerland

[2]IHP, Im Technologiepark 25, 15236 Frankfurt (Oder), Germany

[3]Silicon Radar GmbH, Im Technologiepark 1, 15236 Frankfurt (Oder), Germany

[4]EMPA, 8600 Dübendorf, Switzerland

[5]Department of Physics, The University of Texas, Austin, Texas 78712, United States

[6]Technische Universitaet Berlin, FG Si-Photonik, Einsteinufer 25, 10587 Berlin, Germany

Abstract

To develop a new generation of high-speed photonic modulators on silicon-technology-based photonics, new materials with large Pockels coefficients have been transferred to silicon substrates. Previous approaches focus on realizing stand-alone devices on dedicated silicon substrates, incompatible with the fabrication process in silicon foundries. In this work, we

demonstrate monolithic integration of electro-optic modulators based on the Pockels effect in barium titanate (BTO) thin films into the back-end-of-line of a photonic integrated circuit (PIC) platform. Molecular wafer bonding allows fully PIC-compatible integration of BTO-based devices and is, as shown, scalable to 200 mm wafers. The PIC-integrated BTO Mach-Zehnder modulators outperform conventional Si photonic modulators in modulation efficiency, losses, and static tuning power. The devices show excellent $V_\pi L$ (0.2 V·cm) and $V_\pi L\alpha$ (1.3 V·dB), work at high speed (25 Gbps), and can be tuned at low static power consumption (100 nW). Our concept demonstrates the possibility of monolithic integration of Pockels-based electro-optic modulators in advanced silicon photonic platforms.

Introduction

Silicon technology based photonic integrated circuits (Si PIC) are becoming essential for various applications in the domain of communication technologies [183]. For large data centers, Si PIC technology offers attractive features for transceivers targeting intra and inter data-center communication. Utilizing advanced manufacturing techniques for the co-integration of optics and electronics enables high-speed and cost-effective transceiver solutions that take advantage of device scaling opportunities. Targeting a truly monolithic integration with CMOS (or Bi-CMOS) is crucial for such transceivers. The co-use of the back-end of line (BEOL) by photonic and electronic devices results in the smallest possible parasitics, which is a pre-requisite for efficient RF driving. Standard Si PIC modulators are based on phase shifters using the free-carrier dispersion effect. In terms of phase-shifter properties this is not the optimum solution. Besides a rather low modulation efficiency, nonlinearity and high-loss also limit modulator performance. The impossibility of disentangling amplitude and phase modulation also restricts their use for higher modulation formats [29, 132]. In addition, the high junction capacitance limits the achievable bandwidth [29] and is detrimental for power consumption. It is therefore highly desirable to enable - in a silicon photonic technology - pure electro-optic phase shifters exploiting the Pockels effect, in order to provide a solution without residual amplitude modulation, yet with high linearity, high efficiency and low optical loss. Recently, this field of research experienced a renaissance, with several attempts to demonstrate Pockels modulators potentially compatible with Si-PIC. Different strategies are being followed, using either a strain-induced Pockels effect in silicon [184], using well-known Pockels materials such as $LiNbO_3$, bonded

onto silicon by direct wafer bonding [93, 94], or introducing novel materials with large Pockels coefficients [91, 92]. All these approaches have intrinsic weaknesses, coming either from a weak Pockels effect [184], the limited availability of large wafer sizes [93, 94], thermal stability issues [91], or incompatibility with standard fabrication processes [92].

Our approach utilizes single crystalline, ferroelectric $BaTiO_3$ (BTO) as a material having a large Pockels coefficient and where an integration path of single crystalline layers with silicon does exist [51, 96, 185]. Over the past years, great progress has been made in developing a hybrid BTO/silicon technology, including passive structures with low-propagation losses [95], active electro-optic switching [48, 49], excellent thermal stability [167], and, very recently, large Pockels coefficients of r_{42}=923 pm/V and high-speed modulation in photonic devices [96, 185]. However, previous work was developed on silicon-on-insulator substrates – without attention to process integration in a standard PIC or electronic PIC (EPIC) process. Here, we overcome this limitation and demonstrate the integration of highly efficient BTO Pockels modulators in the BEOL of a silicon photonic process flow and show the scalability of our approach up to 200 mm, making this an attractive technology for high-speed transceivers.

Technology concept

Our concept of high-speed transceivers relies on the monolithic integration of BTO thin films via direct wafer bonding above an interlayer dielectric (ILD) in a standard EPIC flow (Fig. C.1a) [166]. The bonding step can be performed on top of any ILD above the front-end-of-line (FEOL) structures. Using wafer bonding we can first deposit BTO epitaxially on a silicon substrate, and then transfer the epitaxial layer onto an amorphous substrate, such as an ILD. Having an epitaxial BTO film is of importance for two reasons: First, the low defectivity in single-crystalline films is crucial for achieving a large effective Pockels effect in the material [66]. Second, the low surface roughness of epitaxial BTO films is critical for obtaining high bonding yield. To fabricate BTO thin films, we use a deposition process based on molecular beam epitaxy [44, 51], which relies on the epitaxial growth on Si wafers and can thus be scaled to large wafer sizes. The availability of large substrates is major a benefit compared to the bonding of $LiNbO_3$ on silicon or to the epitaxial growth on crystalline oxides, both approaches being limited by the available substrate or donor crystal sizes.

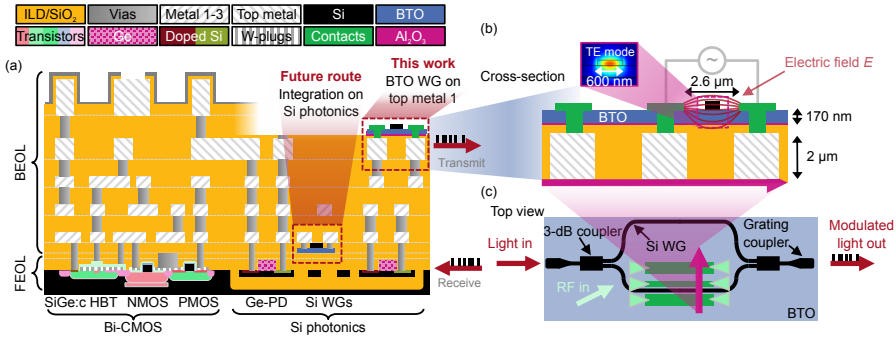

FIGURE C.1: Scheme for monolithic integration of BTO/Si on PIC platforms. (a) Schematic cross-sections of PIC with electrical and optical front-end, and BTO integration in the back-end (this work) or front-end (future route). (b) Cross-section of active BTO/Si waveguide used for electro-optic modulators. The electrodes (shown in grey) are fabricated in the BEOL of the PIC platform. (c) Schematic layout of BTO/Si electro-optic modulator reported in this work. The BTO/Si active waveguide is used as phase shifter in a Mach-Zehnder modulator.

The BTO devices are based on a strip-loaded waveguide geometry, where a Si strip on top of BTO guides the optical mode (Fig. C.1b). Lateral electrodes for phase shifters are made using metal lines fabricated in the top metal level of the BEOL before BTO integration, combined with a final metallization after BTO integration. Optical simulations are used to inform the design of the BTO-Si waveguides and to ensure substantial overlap of the transverse electric (TE) optical mode and the BTO layer at a wavelength of 1550 nm. Using a 170-nm-thick BTO layer loaded with a 100-nm-thick Si strip, we achieve an optical overlap of 38 % between the first order TE mode and the BTO layer. The BTO/Si phase shifters can be used in Mach-Zehnder modulators (MZMs), or ring modulators. In this work we used unbalanced MZMs, with multi-mode interference splitters. Grating couplers were used to couple light in and out of the devices (Fig. C.1c). The magnitude of the refractive index change induced by the Pockels effect is strongly anisotropic and depends on the relative orientation of the crystalline axes, the optical electrical field, and the modulating electric field [69, 96]. To ensure the maximum response we designed phase shifters with waveguides along the BTO[110] direction.

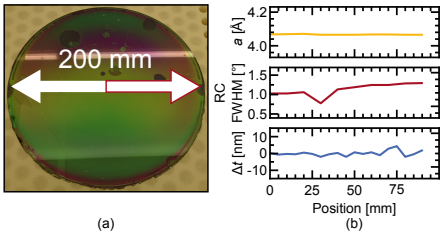

FIGURE C.2: Wafer bonding transfer of thin-film BTO between 200 mm source and target wafers. (a) Photo of transferred BTO layer. (b) Radial measurements of the homogeneity of the transferred BTO layer. XRD and ellipsometry was used to measure the lattice parameter, rocking curve, and thickness of the BTO, all of which show good homogeneity across the 200 mm wafer.

Integration and fabrication

We deposited BTO thin films on $SrTiO_3$-buffered silicon-on-insulator (SOI) substrates with 100 nm top Si using a previously reported process [44, 51]. Deposition of BTO using molecular beam epitaxy ensures a high-quality single-crystal film. After BTO deposition, we transferred the BTO layer and the top Si layer onto a planarized acceptor wafer using thin alumina layers for adhesion at the bonding interface. The donor wafer was subsequently removed by a combination of mechanical grinding and chemical etching, resulting in a high transfer yield from the source wafer.

To demonstrate the scalability of our approach, we transferred BTO layers grown on a 200 mm SOI substrate onto another 200 mm silicon wafer that had been capped with a thermal oxide (Fig. C.2a). The transferred $BaTiO_3$ layer was thoroughly characterized using X-ray diffraction (XRD) and ellipsometry (Fig. C.2b). The out-of-plane lattice parameter and rocking curve show good crystalline homogeneity with only minor variations along the 100 mm radius. Additionally, the thickness of the BTO, measured by ellipsometry, varies only minimally across the wafer. The observed variations in thickness contain a significant uncertainty due to variations also in the other layers of the stack.

For the fabrication of modulators (Fig. C.3), we used 200 mm target wafers, processed following a PIC flow having the same BEOL processes as EPIC runs [186]. In this work, the BEOL process of the PIC run was interrupted at the 4th metallization level, top metal 1 (TM1), after ILD planarization. We transferred a 170-nm-thick BTO layer from a 50 mm SOI wafer onto

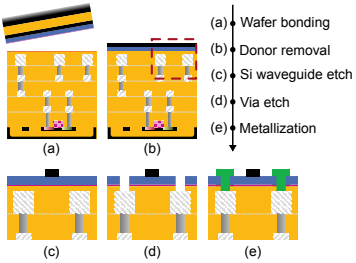

FIGURE C.3: Simplified process flow for integration of BTO modulators in the BEOL of a PIC process flow. Schematics of the cross-sections (left) are shown at various steps in the process (right). After wafer-bonding of the BTO and Si layers, the Si is patterned into a strip-loaded waveguide, after which vias and contacts are fabricated. Figures (c)-(d) show a magnification of the region within the dashed rectangle in (b).

the planarized PIC wafer. Si waveguides were patterned by dry etching. In order to ensure a homogeneous electric field across the BTO and to avoid a voltage drop over the thin ILD layer between BTO and TM1, vias to TM1 were etched through the BTO and the ILD along the waveguides. With a final metallization step, we extended the buried RF lines on top of the BTO. A cross-sectional electron micrograph (Fig. C.4) demonstrates the successful fabrication of BTO/Si modulators on the PIC substrate.

Direct wafer bonding using Al_2O_3 adhesion layers has a temperature budget well within the limits of the BEOL process [54]. However, annealing steps at temperatures up to 350°Care needed to reduce the propagation losses in the BTO layer [95]. It is therefore necessary to verify that the BTO integration does not cause any degradation of FEOL components. As the Ge photodiodes fabricated in the FEOL are highly sensitive to thermal degradation, we characterized their performance before and after BTO device integration. We cannot detect any degradation in either dark current or high-speed signal detection performance (Fig. C.5). The absence of such degradation confirms that our integration strategy is compatible with the thermal limitations of the FEOL and BEOL processes, making integration of BTO devices compatible with PIC platforms, and fulfills the prerequisites for compatibility with EPIC platforms.

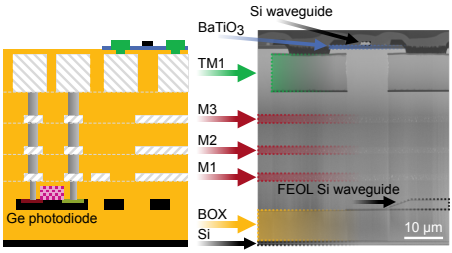

FIGURE C.4: Cross-sectional STEM image of BTO modulator integrated after top metal 1 (TM1) in BEOL process of a Si PIC wafer. The schematic shows how the modulator was integrated in this work. The electron micrograph shows the successful integration of BTO/Si modulators. Intermediate metal levels (M1 to M3) as well as the FEOL levels can be identified.

Device performance

To characterize the device performance, we used both passive ring resonators and active MZMs. The ring resonators had a radius of 30 µm, to ensure negligible bending losses, and allow accurate extraction of propagation loss. From the high Q-factor ($\sim$50,000) of ring resonators we extract a propagation loss of 5.8 dB/cm. Since the BTO layer itself has only minimal contributions to the propagation losses [95], we are instead limited by scattering losses in the Si waveguides. Using an optimized patterning process the propagation losses can be reduced further. We performed

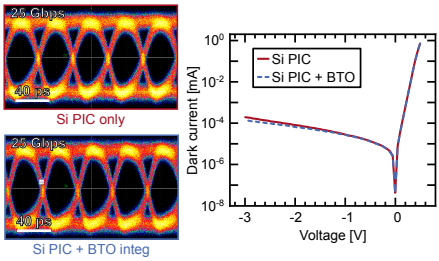

FIGURE C.5: Comparison of FEOL Ge photodiode performance before and after integration BTO modulators. The photodiodes were characterized by recording a modulated data signal, and by measuring the dark-current. No detectable degradation is caused by integration of BTO modulators, showing that the integration scheme is compatible with the PIC FEOL.

electro-optic characterization on unbalanced MZMs with phase shifter lengths of 1-2 mm. By applying a voltage to one arm of the MZM and recording the induced phase shift as a function of the applied voltage (Fig. C.6), we extracted the DC $V_\pi L$ value as 0.23 V·cm. This value is 10 times smaller than state-of-the-art Si depletion-type plasma-dispersion modulators ($V_\pi L \sim 2$ V·cm) [15, 29] and comparable to integrated silicon semiconductor-insulator-semiconductor capacitor (SISCAP) modulators ($V_\pi L$ of $\sim$0.2 V·cm) [97]. When taking into account propagation losses α we reach a $V_\pi L\alpha$ of 1.3 V·dB, which is significantly better than any available high-speed Si modulator ($V_\pi L\alpha$ >10 V·dB). In the current devices the propagation losses are limited by scattering from roughness in the Si waveguide. By improved processing, propagation losses can be reduced to less than 3 dB/cm, resulting in a $V_\pi L\alpha$ <0.7 V·dB. The low $V_\pi L\alpha$ shows one of the key advantages of the hybrid BTO/Si technology compared to alternative modulator concepts: BTO/Si shows both a large electro-optic response and low insertion losses, since neither high doping levels nor absorbing materials are needed in the modulator design.

When sweeping the bias voltage, the phase shift of the MZM (Fig. C.6a) exhibited a hysteretic behavior, consistent with the ferroelectric nature of BTO [96]. The hysteresis curve illustrates the need for poling the BTO layer with a bias above the coercive field ($\sim$1 V) to maximize the electro-optic response. For smaller bias voltages, mixed ferroelectric domain states result in a reduced effective Pockels effect r_{eff}, which ultimately vanishes for evenly populated domain states [51] (Fig. C.6b). The cancellation effect of opposing domains causes a deviation from the linear phase response when varying a DC voltage: The total electro-optic response is the convolution of the linear Pockels effect and nonlinear domain switching effects. To isolate the Pockels effect from the electro-optical response we extract the V_π at the extremes of the curve shown in Fig. C.6a, where all domains have been poled. The re-orientation of ferroelectric domains is a relatively slow process («1 GHz) [187], which does not impact the operation of the modulator at high frequency – even at a bias below the poling voltage.

Moreover, as the Pockels effect is an electric-field effect, very low-power tuning of the MZMs is possible. The low leakage results in extremely low tuning powers, P_π <100 nW (Fig. C.7), compared to silicon thermo-optic tuning elements which typically have a P_π >1 mW [188]. As the Pockels-effect is a linear EO effect the device bias can be used for tuning without changing propagation losses and without affecting the modulation efficiency.

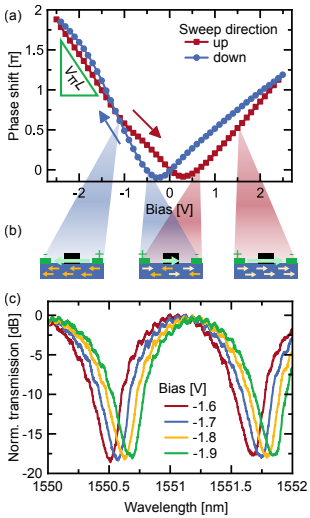

FIGURE C.6: (a) Induced phase shift when applying voltage to one arm of a 2-mm-long MZM. The response is linear at large voltages but shows non-linear, hysteretic contributions for small biases due to ferroelectric domain switching in the BTO layer as visualized in (b): The yellow arrows correspond to the polarization of ferroelectric domains. In the middle configuration the EO response of oppositely oriented domains cancel out, resulting in a vanishing effective Pockels coefficient. A sufficient bias voltage can align the domains to maximize the EO response. The ferro-electric domain switching is a slow effect that does not occur at frequencies >1 GHz. (c) Transmission spectra at various bias voltages in the poled regime used for $V_\pi L$ extraction.

From the measured $V_\pi L$ it is possible to extract the effective Pockels coefficient r_{eff} of the BTO layer using eq. C.1

$$r_{\text{eff}} = \frac{\lambda g}{n_{\text{BTO}}^3 \Gamma_{\text{BTO}} V_\pi L} \tag{C.1}$$

as $r_{\text{eff}} = 380$ pm/V. Here, λ is the operating wavelength of 1.55 µm, g is the electrode-gap (2.6 µm), n_{BTO} is the refractive index of BTO (2.29) as measured by ellipsometry on similar films, and Γ_{BTO} is the EO interaction factor which can be estimated as the optical overlap with BTO (38 %) assuming a homogeneous electric field across the BTO. The magnitude of the extracted r_{eff} is in the range of expected values for BTO thin films: The electro-optic response exceeds values previously reported on MBE-grown

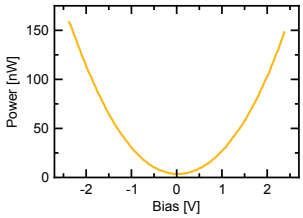

FIGURE C.7: Power-voltage characteristics of a 2-mm-long MZM device. The leakage current is small in the full bias range (<100 nA), resulting in low static power consumption of ∼100 nW at the operating point of 2 V.

BTO layers on silicon [48, 51, 66], but is smaller than those reported in ref. [96], where BTO films of very high crystalline quality with rocking curves of 0.3° are reported. The variation of the magnitude of the Pockels coefficients in similar material stacks is in agreement with the dependence of the electro-optic response on the actual crystalline quality and film morphology [66].

To determine the high-frequency response, small-signal electro-optic S_{21} measurements were performed on a MZM with 1-mm-long electrodes (Fig. C.8). The 3-dB bandwidth is 2 GHz. The reason for this limited bandwidth is a mismatch between the optical mode and the electrical mode in the traveling wave electrodes, caused by the high dielectric constant of the BTO. Our device designs are based on moderate BTO permittivity values of $\epsilon_{BTO} = 100$ [77], which turned out to be strongly underestimated compared to recent reports of ϵ_{BTO} as high as 3000 in epitaxial $BaTiO_3$ thin films [96, 189, 190]. To improve the bandwidth, the electrodes should be designed based on the actual properties of the BTO layer to achieve mode matching between the RF and optical modes. To show that the bandwidth is not limited by the electro-optic properties of the material but rather by the electrical design, we measured the bandwidth of a ring modulator with a 10 μm radius, the small radius induces bending losses resulting in a reduced Q-factor of ∼15,000. The measured bandwidth of ∼20 GHz (Fig. C.8) is limited by the photon lifetime (Q-factor ∼15,000) but demonstrates the potential for high bandwidth operation using BTO/Si devices – as confirmed in previous reports [96, 167].

We further characterized the high-speed performance of the BTO/Si modulators with data-modulation experiments using a 1-mm-long MZM. An electrical pseudorandom binary sequence (PRBS) was generated with a

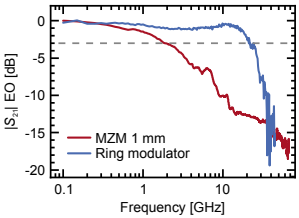

FIGURE C.8: Small signal frequency response of a 1-mm-long MZM, and a ring modulator with radius 10 μm. The bandwidth of the MZM is limited by mismatch between the optical and RF modes, whereas the ring modulator is limited by the photon lifetime.

bit-pattern generator, without pre-emphasis or any other signal processing. The signal was amplified (V_p ~2 V) and was then applied to one arm of the MZM along with a 2 V DC bias. The MZM was operated in a traveling wave configuration with an off-chip 50 Ω termination. The modulated optical signal was amplified (to compensate losses from grating couplers and from the experimental setup) and directly detected using a high-speed photodiode. Eye-diagrams were recorded on a sampling oscilloscope with 10, 20, and 25 Gbps data rates (Fig. C.9). Non-closed eyes can be achieved even at 25 Gbps, however the result of the limited EO bandwidth of the modulator is qualitatively visible as a reduction eye opening from 10 to

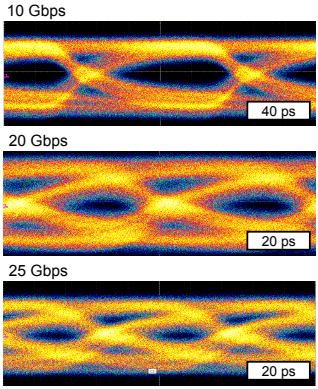

FIGURE C.9: Eye-diagrams from back-to-back data transmission through 1-mm-long BTO MZM in single-drive mode at 10, 20, and 25 Gbps, respectively. A bias voltage of 2 V was applied during the experiments.

25 Gbps. With an adapted electrode design, we expect to reach data rates >50 Gbps using MZMs.

Conclusion

We have shown how a material ($BaTiO_3$) with the Pockels effect can be integrated into a silicon photonics platform in a scalable way using direct wafer bonding. The demonstrated Mach-Zehnder modulators show excellent performance, exceeding state-of-the-art silicon-based devices on several figures of merit, such as $V_\pi L$ and $V_\pi L\alpha$. The established integration concept provides a path for a novel generation of high-speed modulators and ultra-fast switches. The technology is however not limited to such existing components, but further enables entirely new types of devices on a silicon photonics platform. Using BTO, ultra-low-power tuning elements [49] and compact plasmonic devices [96, 191], as well as non-volatile elements for optical neuromorphic computing exploiting ferro-electric domain switching [107] are possible.

D

INTEGRATED FERROELECTRIC PLASMONIC OPTICAL MODULATOR

2017 Optical Fiber Communications Conference (OFC), Th5C.7, Post deadline paper (Optical Society of America, 2017)

DOI: https://doi.org/10.1364/OFC.2017.Th5C.7

Andreas Messner[1*], Felix Eltes[2*], Ping Ma[1], Stefan Abel[2], Benedikt Baeuerle[1], Arne Josten[1], Wolfgang Heni[1], Daniele Caimi[2], Jean Fompeyrine[2], Juerg Leuthold[1]

[1]Institute of Electromagnetic Fields (IEF), ETH Zurich, 8092 Zurich, Switzerland

[2]IBM Research – Zurich, Säumerstrasse 4, 8803 Rüschlikon, Switzerland

*These authors contributed equally to this work

Abstract

An integrated ferroelectric plasmonic Mach-Zehnder modulator is demonstrated to work in a direct-detection setup with a 72 Gbit/s NRZ modulation format. The device works reliably beyond 130°Cwith an extinction ratio beyond 15 dB.

Introduction

Optical modulators based on the linear electro-optic (EO) effect (Pockels effect) have become the workhorse in high-capacity links. The linear EO effect is of particular interest as it provides a pure phase modulation, which can be used in Mach-Zehnder and IQ-modulator to encode advanced modulation formats. However, to keep up with the ever-increasing demand for capacity such modulators should be integratable with standard CMOS

technology and offer a large bandwidth across a large optical spectrum at the most compact footprint.

Silicon photonics is currently one of the most promising platforms for enabling highly integrated mixed electronics-photonics circuits because it relies on the standard CMOS fabrication infrastructure. Since a strong linear electro-optic effect is absent in silicon, silicon modulators are normally based on the plasma dispersion effect. Although this effect has bandwidth limitations [29], it enables data rates of 70 Gbit/s in a single Mach-Zehnder modulator [133]; more complex configurations allow data rates of 224 Gbit/s [192]. Other attempts take advantage of organic materials with a linear EO coefficient to overcome the speed limitations, such as silicon-organic hybrid modulators. IQ-modulators extend into the range of 252 Gbit/s [193], with EO bandwidths up to 100 GHz [194]. Plasmonic modulators promise ultimate *RC*-limited speed, enhanced device power efficiency and smallest footprint thank to the concentrated optical mode. Recently, plasmonic-organic hybrid modulators with a bandwidth of up to 170 GHz and data rates exceeding 100 Gbit/s have been realized [101]. While all the solutions meet the demand and enable high-speed optical links, they either have a large footprint or rely on organic nonlinear materials, which are not CMOS compatible, require a complicated poling procedure and encounter reservations about their thermal limitations. Integrated ferroelectrics exhibit a strong electro-optic effect and are chemically and thermally stable materials. Barium titanate ($BaTiO_3$) thin films deposited epitaxially on silicon possess a very high $\chi^{(2)}$ nonlinearity [51], which can be exploited in silicon photonics devices [48, 49].

Here, we demonstrate a plasmonic ferroelectric $BaTiO_3$ Mach-Zehnder modulator on silicon operating in a NRZ 72 Gbit/s experiment without pre- and post-equalization and bit-error ratios well below the standard FEC limit. The active section is as short as 10 μm. No degradation due to temperature exposure beyond 250°Chas been found.

Ferroelectric Plasmonic Modulator

The ferroelectric plasmonic modulator (FPM) represents a new type of plasmonic electro-optic modulators, based on ferroelectric $BaTiO_3$. The Mach-Zehnder modulator, see Fig. D.1(a), consists of two ferroelectric phase modulators, see Fig. D.1(b). A simulation of the plasmonic mode in the phase modulator is shown in Fig. D.1(c). Two tapered mode converters

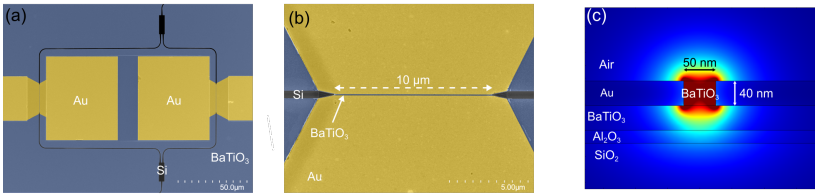

FIGURE D.1: False color SEM image of (a) Ferroelectric Plasmonic Mach-Zehnder Modulator (FPM), and (b) plasmonic phase modulator. (c) Simulated optical mode profile and layer stack in the plasmonic section.

couple the photonic mode from access waveguides to the plasmonic slot and back again. On-chip multimode interference couplers (MMIs) are employed to split the light to the two arms of the FPM. A geometrical path length difference of 100 µm between the two arms is used to obtain an easily controllable operating point. Grating couplers are used to couple light into and from the chip.

The FPM exploits the Pockels effect of $BaTiO_3$, allowing high frequency operation with low power consumption. Key to the FPM is a plasmonic phase modulator. The footprint of a single 10 µmlong phase modulator can be as small as 20 μm^2 but is currently constrained by the size of the contact pads.

To fabricate the device, an 80-nm-thick $BaTiO_3$ film was deposited epitaxially on a SOI wafer by molecular beam epitaxy [51]. The wafer was bonded to a 3 µm SiO_2 on highly resistive silicon wafer using Al_2O_3 adhesion layers. The original $BaTiO_3$ handle wafer was stripped and the buried oxide was removed. The silicon photonic components were structured by e-beam lithography (EBL) and subsequently dry-etched. 50-nm-wide and 40-nm-tall $BaTiO_3$ strips were structured by EBL and dry-etched, gold electrodes were applied by e-beam evaporation and subsequent lift-off to form plasmonic waveguides.

The effective Pockels coefficient derived from measurements is in the range of 25 pm/V to 100 pm/V at 65 GHz. There is quite some uncertainty in this value because the extent of the poling in the slab is unknown. It is important to point out however, that the refractive index changes with $\Delta n \sim n_0^3 \cdot r_{\text{eff}}$. Since the refractive index of $BaTiO_3$ is $n_0 \approx 2.3$ and thus larger than in competing organic approaches the overall refractive index Δn is large despite of a moderate effective electro-optic coefficient. With

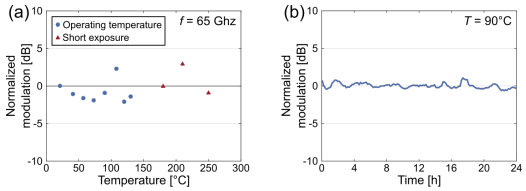

FIGURE D.2: (a) Plot of the EO response of the plasmonic phase modulator at 65 GHz at different temperatures. No degradation is seen when operating the device up to 150°C (blue) and no degradation is found when exposing the device to short term heading (5 min) exposure for up to 250°C (red). The fluctuations are attributed to coupling challenges. (b) Modulation at 65 GHz during 24 hours of continuous operation at 90°C showing no sign of device degradation.

the current device, the V_π is 14.5 V. Simulations indicate a loss of 1 dB per μm of plasmonic waveguide with about 2 dB in conversion losses from the waveguide to the plasmonic slot waveguides. However, this first device generation comes with an insertion loss of 25 dB for a 10-μm-long, 50-nm-wide plasmonic phase modulator. These losses include at least 10 dB from the photonic-to-plasmonic converters and 15 dB plasmonic slot waveguide losses. SEM images and simulations indicate that there is room for improvement by optimizing the waveguide sidewalls, the plasmonic-to-photonic converters and the grating couplers.

To show the stability of the FPM across a large temperature operating range, we measure the electro-optic modulation at temperatures ranging from 20 to 130°C, see Fig. D.2(a), as well as the response of the device after a 5-minute exposure to temperatures up to 25o°C, showing the process compatibility of the device. The devices also show long-term stability at 90°C, a typical operating temperature, see Fig. D.2(b).

Data transmission experiment

Data transmission experiments up to 72 Gbit/s have been performed in a direct detection setup, see Fig. D.3. Clear and open eyes can be seen even without predistortion or post-equalization.

For the experiment, a De Brujin bit sequence of order 18 was generated offline and sent to the memory of a digital-to-analog converter (DAC) with a sampling rate of 72 GSa/s and a 3 dB bandwidth of 16 GHz. Higher-order sequences were not available due to memory restrictions. The DAC's

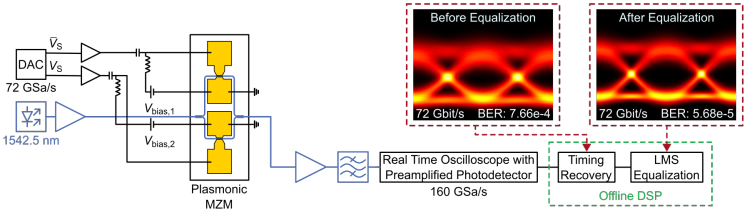

FIGURE D.3: Schematic of the data experimental setup. The signal was created offline and sent to a DAC (3 dB BW: 16 GHz). The signal is electrically amplified and fed to the chip. CW light from an ECL is boosted to 18 dBm by an EDFA before it is coupled to the chip. The FPM is driven in push-pull mode. A DC bias is applied on each arm. The modulated light is amplified before it is digitized and processed. The insets show the eye-diagrams of a 72 Gbit/s NRZ data transmission before and after equalization.

differential output signals were electrically amplified before they were fed to the chip. The Mach-Zehnder modulator was operated in dual-drive push-pull mode. The applied voltage-peak $V_p = 2.8$ V. The extinction ratio is estimated to be larger than 15 dB. Two bias tees were used to apply a DC bias of ca. 3 V over each of the two arms. The DC bias could also be used to fine-tune the operating point of the FPM.

Light from an external cavity laser (ECL) at 1542.5 nm wavelength was amplified to 18 dBm by an erbium doped fiber amplifier (EDFA) and launched onto chip using grating couplers. Two cascaded EDFAs amplified the optical output signal before it was detected by a 70 GHz PIN photo diode and digitized by a real-time oscilloscope with 160 GSa/s and an electrical bandwidth of 62 GHz.

The digitized signal was processed offline. First, we did a timing recovery and resampled the signal to two samples per symbol. The eye diagram of this operation is shown in Fig. D.3. Subsequently, a T/2-spaced feed-forward equalizer with 51 taps which is adaptively controlled by a decision direct least mean square (DD-LMS) algorithm has been used to compensate for linear distortions. The eye diagram of which is shown as well in Fig. D.3. Finally, we made a hard decision, evaluated 899,000 bits, counted the errors, and calculated the bit error rates (BER).

Data transmission has been achieved at 18, 36, 48, 54, 56, 64 and 72 Gbit/s, with all measured BERs being well below a 7 % hard-decision FEC threshold of $BER = 3.8 \times 10^{-3}$. The resulting eye diagram for the transmissions

of 72 Gbit/s are shown as an inset in Fig. D.3, the measured BER are 7.66×10^{-4} after timing recovery, and 5.68×10^{-5} after LMS equalization. These results demonstrate clearly the device's capability to act in a direct transmission scheme without costly transmitter or receiver DSP.

Conclusions

We have experimentally demonstrated for the first time an ultra-compact ferroelectric plasmonic modulator. We have shown that the device is stable over time at typical CPU operating temperatures, and has a stable electro-optic response up to 130°C. Finally, we are able to demonstrate a directly detected 72 Gbit/s NRZ transmission through a Mach-Zehnder modulator. This shows the device's potential for application in real-life environments.

E

AN INTEGRATED CRYOGENIC OPTICAL MODULATOR

Currently under review

Felix Eltes[1], Gerardo E. Villarreal-Garcia[2], Daniele Caimi[1], Heinz Siegwart[1], Antonio A. Gentile[2], Andy Hart[2], Pascal Stark[1], Graham D. Marshall[2], Mark G. Thompson[2], Jorge Barreto[2], Jean Fompeyrine[1], Stefan Abel[1]

[1]IBM Research – Zurich, Säumerstrasse 4, 8803 Rüschlikon, Switzerland

[2]Quantum Engineering Technology Labs, H. H. Wills Physics Laboratory, University of Bristol, Bristol, BS8 1TL, United Kingdom

Integrated electrical and photonic circuits (PIC) operating at cryogenic temperatures are fundamental building blocks required to achieve scalable quantum computing, and cryogenic computing technologies [115, 116, 120, 121]. Optical interconnects offer better performance and thermal insulation than electrical wires and are imperative for true quantum communication. Silicon PICs have matured for room temperature applications but their cryogenic performance is limited by the absence of efficient low temperature electro-optic (EO) modulation. While detectors and lasers perform better at low temperature [195, 196], cryogenic optical switching remains an unsolved challenge. Here we demonstrate EO switching and modulation from room temperature down to 4 K by using the Pockels effect in integrated barium titanate ($BaTiO_3$)-based devices [96]. We report the nonlinear optical (NLO) properties of $BaTiO_3$ in a temperature range which has previously not been explored, showing an effective Pockels coefficient of 200 pm/V at 4 K. We demonstrate the largest EO bandwidth (30 GHz) of any cryogenic switch to date, ultra-low-power tuning which is 10^9 times more efficient than thermal tuning, and high-speed data modulation at 20 Gbps. Our results demonstrate a missing component for cryogenic PICs. It removes major roadblocks for the realisation of novel cryogenic-compatible systems in the

field of quantum computing and supercomputing, and for interfacing those systems with the real world at room-temperature.

Cryogenic technologies are becoming essential for future computing systems, a trend fuelled by the world-wide quest to develop quantum computing systems and future generations of high-performance classical computing systems [117, 118]. While most computing architectures rely solely on electronic circuits, photonic components are becoming increasingly important in two areas. First, PICs can be used for quantum computing approaches where the quantum nature of photons is exploited as qubits [120, 121]. Second, optical interconnects can overcome limitations in bandwidth and heat leakage that are present in conventional electrical interconnect solutions for digital data transfer between cryogenic processors and the room temperature environment [116]. In addition, due to their low interaction with the environment, photons are the only viable carriers to transport quantum states over large distances. Optical interfaces are therefore essential for true quantum communication, necessary to connect multiple quantum computers [123, 124] and for secure remote operation of quantum computers [125].

Today, the realisation of such photonic concepts is hindered by the lack of switches and modulators that operate at cryogenic temperatures with low-loss, high bandwidth, and low static power consumption. So far, only two concepts for cryogenic EO switches have been investigated, based either on the thermo-optic effect [127] or the plasma-dispersion effect [126]. Both mechanisms have physical limitations which intrinsically restrict the low-temperature performance of such devices. Thermo-optic phase shifters exploit Joule heating with large static power consumption and exhibit a bandwidth of less than a few MHz [128]. Plasma-dispersion-based devices require very high doping levels to compensate for carrier freeze-out at cryogenic temperatures. The high doping leads to large propagation losses and devices are limited to a bandwidth of <5 GHz in micro-disk modulators [126]. The use of EO switches based on the Pockels effect has been shown to offer low propagation losses and high-bandwidth, combined with low static power consumption at room temperature [92, 94–96]. Because of its electro-static nature, the Pockels effect has no intrinsic physical limitations for its application at cryogenic temperature. However, the lack of a Pockels effect in silicon means that heterogenous integration of new materials is needed to bring Pockels-based switching in PIC platforms. Pockels modulators have recently been demonstrated using organics [197], PZT [92], $LiNbO_3$ [198], and $BaTiO_3$ [96]. Among them, $BaTiO_3$ stands out due to

having the largest Pockels coefficients [96] and exhibiting compatibility with advanced silicon photonics platforms [199]. We complete this triumvirate by demonstrating that $BaTiO_3$ is also an ideal candidate for cryogenic EO integration.

Both the NLO properties and structural behaviour of $BaTiO_3$ thin-films are entirely unknown at temperatures below 300 K. In fact, even in bulk $BaTiO_3$ crystals the NLO behaviour is unexplored below 270 K, and the room temperature NLO behaviour of $BaTiO_3$ thin-films has only recently been thoroughly investigated [96]. Predictions of the Pockels tensor at cryogenic temperatures based on data at higher temperatures is not possible because the temperature dependence of neither the Pockels coefficients nor the crystalline phase of thin-film $BaTiO_3$ on Si is known. The phase transitions of thin-films are expected to differ from bulk crystals [112] due to the structural mismatch and thermal stress that exists between the substrate and the $BaTiO_3$ layer [129–131]. Here, we determine the cryogenic behaviour of $BaTiO_3$ thin films by analysing the performance of $BaTiO_3$-based EO switches at temperatures down to 4 K. Our results show that efficient EO switching at cryogenic temperature is indeed possible and with bandwidths beyond 30 GHz. We also demonstrate the applicability of such devices for low-power switching and tuning as well as high-speed data modulation at 20 Gbps at 4 K.

In this work, we use two waveguide designs fabricated on single crystalline $BaTiO_3$ layers bonded to SiO_2-buffered silicon substrates (Figure E.1a, see Methods). In the first design, silicon nitride (SiN)-based waveguides allowed us to study the pure NLO properties of $BaTiO_3$ in absence of mobile charge carriers which could result in an additional, non-Pockels EO response. In the second, silicon (Si) waveguides served as more efficient devices to demonstrate high-speed data modulation. The enhanced efficiency originates from a larger optical-mode overlap with the $BaTiO_3$ layer (41 %) than with the SiN waveguides (18 %) (Figure E.1b,c). We found that the propagation losses (5.6 dB/cm, SiN device) were not affected by the presence of $BaTiO_3$ in the active section (Supplementary Note, SN 1) throughout the temperature range studied.

To characterise the NLO behaviour of $BaTiO_3$ at 4 K, we measured the induced resonance shift in a racetrack resonator as a function of the DC bias (Figure E.1d,e), from which we determined the refractive index change of $BaTiO_3$ (Δn_{BTO}) as a function of the applied electric field (see Methods). This dependence allows us to study two of the three expected features

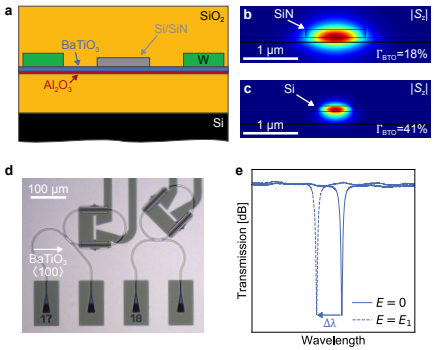

FIGURE E.1: $BaTiO_3$ electro-optic device concept. (a), Schematic cross-section of the devices. A silicon or silicon nitride layer forms a strip-waveguide on top of an $BaTiO_3$ layer. Lateral electrodes fabricated with W are used to apply an electric field across the $BaTiO_3$. The devices are embedded in SiO_2 layers on top of silicon substrates. (b), Optical mode simulation of the SiN waveguide geometry and (c) the Si waveguide geometry, showing an optical confinement in $BaTiO_3$ of 18 % and 41 % respectively. (d), Optical micrograph of racetrack resonator devices used to characterise the nonlinear optical properties of $BaTiO_3$. (e), Characterisation principle of resonant electro-optic switches, showing example data of a shifted resonance. The shift in resonance wavelength is measured for an applied electric field and converted to the material properties of $BaTiO_3$ (see Methods).

of Pockels-based switching [96]: NLO hysteresis and angular anisotropy, the third being the persistence of the Pockels effect at high frequencies (>10 GHz) [85].

The NLO response with a hysteretic behaviour (Figure E.2a) indicates that a non-vanishing Pockels effect is preserved in $BaTiO_3$ down to a temperature of 4 K. We determine the effective Pockels coefficient, r_{eff}, by analysing the hysteretic behaviour of the refractive index change (SN 2). The dependence of r_{eff} on device orientation (Figure E.2b) reveals the second signature of the Pockels effect, its anisotropy. The reduced magnitude at 4 K compared to room temperature is due to a temperature dependence of the Pockels effect, as discussed below. While r_{eff} is reduced with temperature, the EO response is expected to be present at high frequencies also at low temperature. Indeed, we observe a constant EO response in racetrack resonators with a low Q factor ($Q \sim 1,800$) up to 30 GHz (Figure E.2b). This constitutes the highest bandwidth for any cryogenic modulator reported to date. The frequency response is expected to remain flat at even higher frequency but

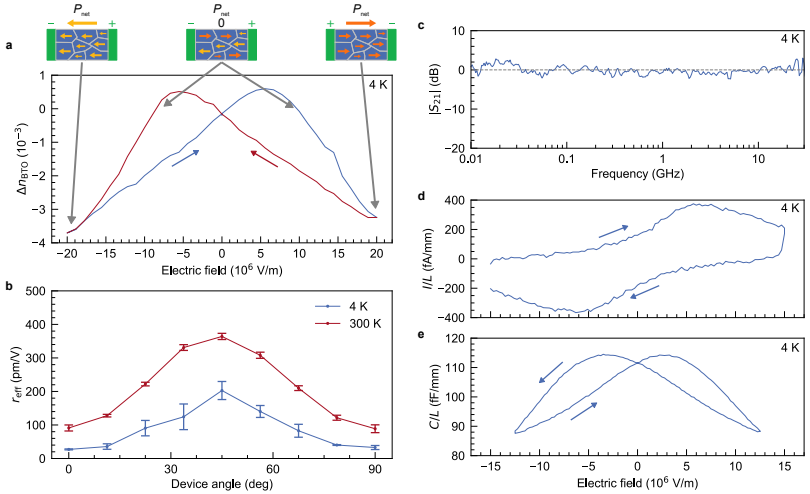

FIGURE E.2: Electro-optic and electrical response of $BaTiO_3$-based optical switches at 4 K. (a), Refractive index change of $BaTiO_3$ as a function of applied electric field for a device in the 11.25° direction (as defined in b). The hysteretic behaviour originates from ferroelectric domain switching in the $BaTiO_3$, as shown schematically (top). (b), Angular anisotropy of the effective Pockels coefficient in $BaTiO_3$. The angle is defined relative to the $BaTiO_3$<100> direction. The same anisotropy as for $BaTiO_3$ at room temperature is observed but with reduced magnitude. The error bars show the combined standard error of the fit and from averaging measurements of multiple devices with the same orientation. c, Electro-optic S_{21}-parameter of $BaTiO_3$ ring resonator showing a flat response up to a record frequency of 30 GHz at 4 K. (d), Current measured as a function of electric field across the $BaTiO_3$ layer showing extremely low current flowing through the material. The current is dominated by capacitive charging together with ferroelectric switching current resulting in a peak (SN 3). (e), Capacitance as a function of electric field, showing characteristic ferroelectric hysteresis and field-dependent permittivity.

could not be measured in our experiment (see Methods). The hysteretic behaviour, anisotropy, and high-speed response prove the presence of the Pockels effect in $BaTiO_3$ at 4 K.

We performed electrical characterisation of the material at low temperature using dedicated electrical test structures (SN 3). The resistivity of $BaTiO_3$ at 4 K is very high, $>10^9$ Ωm. In fact, the measured current is dominated by capacitive charging and ferroelectric switching currents (Figure E.2d).

The field-dependent capacitance shows clear hysteretic characteristics (Figure E.2e), consistent with ferroelectric domain switching.

The measured r_{eff} at 4 K is lower than at room temperature (Figure E.2b), which has two causes. First, the Pockels effect itself is generally temperature dependent due to changes in strain and polarisation of the crystal [38]. Second, the non-zero elements of the Pockels tensor depend on the crystal symmetry, which can change abruptly with temperature due to structural phase transitions. $BaTiO_3$ bulk crystals are known to transition from a tetragonal phase at room temperature to orthorhombic and rhombohedral phases at lower temperatures ($\sim$270 K and $\sim$200 K respectively) [111]. Such transitions change the elements of the Pockels tensor and modify the magnitude of the effective Pockels coefficients [38]. Because phase transitions of thin-film materials can be drastically affected by substrate strain [129–131], studying the properties of thin-film $BaTiO_3$ becomes critical when considering cryogenic applications. To investigate the effects of possible phase transitions, we measured r_{eff} in a range from 4 to 340 K. Indeed, the magnitude of r_{eff} is strongly temperature-dependent (Figure E.3). A peak around 240 K, with r_{eff}>700 pm/V, is consistent with the reported divergence of the r_{42} element of the Pockels tensor close to the tetragonal-orthorhombic transition [38]. Consistently, the permittivity of the $BaTiO_3$ layer (see Methods) also shows a peak in the same temperature range (SN 4), confirming that the abrupt change in r_{eff} is caused by a phase transition. Below 240 K the magnitude of r_{eff} decreases gradually to around 200 pm/V at 4 K. In addition to the phase transition at 240 K, a second phase transition occurs below 100 K causing a rapid change in r_{eff} of 90° devices. This phase transition is also observed in the qualitative behaviour of the NLO hysteresis which shows that the transitions is induced by the electric field (SN 4). While r_{eff} of $BaTiO_3$ is reduced at 4 K compared to room temperature, the value of $\sim$200 pm/V is still larger than most other material systems at room temperature [34, 92, 200]. The effect of a reduced Pockels coefficient on the energy efficiency of EO switching is partially compensated for by a simultaneous reduction of the permittivity of $BaTiO_3$ (SN 4). Additionally, the conductivity of $BaTiO_3$ is reduced by more than four orders of magnitude (SN 3), resulting in a negligible static power consumption of $BaTiO_3$-devices in cryogenic environments.

We demonstrate the applicability of $BaTiO_3$ for cryogenic photonic applications by two examples: low-power EO switching and high-speed data modulation. For switching we use a Mach-Zehnder interferometer with 2×2 multimode interference splitters, applying a voltage to one arm. Because

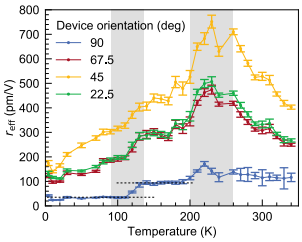

FIGURE E.3: Temperature dependence of the Pockels effect in $BaTiO_3$. The effective Pockels coefficient along different crystal orientations at temperatures from 4 K to 340 K. The peak around 240 K is the signature of a phase transition in $BaTiO_3$. A second, field-induced phase transition occurs around 100 K, causing a sharp drop of r_{eff} in 90° devices (indicated by horizontal dashed lines). This phase transition is also evident in the qualitative evaluation of the optical response (SN 4). The grey areas indicate the temperature ranges of the respective phase transitions. The error bars show the standard error of the fit used to extract the Pockels coefficients (SN 2).

the leakage current through $BaTiO_3$ at 4 K is 10^4 times lower than at 300 K, less than 10 pW static power is consumed when inducing a π phase shift to switch between the two optical outputs (Figure E.4a,b). Compared to state-of-the-art technology based on thermo-optic phase shifters [127], static tuning using $BaTiO_3$ is one billion times more power efficient. The dynamic energy of the switch is ~30 pJ, which could be reduced to ~2 pJ in an optimised device geometry (SN 5). As a second example, we performed data modulation experiments by sending a pseudo-random bit-sequence to the modulator and recording the optical eye-diagram (Figure E.4c,d). Data transmission at rates up to 20 Gbps are achieved with our experimental setup using a drive voltage (V_{pp}) of just 1.7 V, resulting in an extremely low energy consumption of 45 fJ/bit.

In conclusion, we have shown that $BaTiO_3$ thin films can be used to realise EO switches and modulators for efficient cryogenic operation of silicon PICs. We have demonstrated low-power switching, as well as high-speed data modulation. Combining $BaTiO_3$ with silicon photonic integrated circuits, we make a building block available that was previously inaccessible for any cryogenic circuits. We anticipate that such new components are a milestone for a versatile platform of cryogenic photonics for applications such as quantum computing and cryogenic computing technology, as well as quantum interconnects to room-temperature environments.

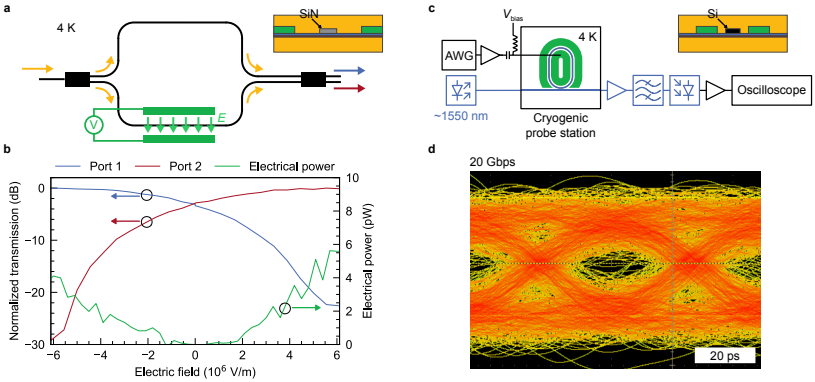

FIGURE E.4: Demonstration of low-power switching and high-speed data modulation with $BaTiO_3$-based devices at 4 K. (a), Schematic of Mach-Zehnder (MZ) configuration used to switch between two ports. The inset shows the waveguide cross-section. (b), Transmission from both ports of a MZ switch as a function of applied electric field, along with the static power consumption. When fully switching between outputs, less than 10 pW static power is consumed, and only 30 pJ of dynamic energy. (c), Schematic of the experimental setup for data modulation. The electrical signal was amplified to compensate for losses into the cryogenic probe station, and then applied to the device. The modulated optical signal was detected using a photodiode and recorded on a high-speed oscilloscope. The inset show the waveguide cross-section. (d), Eye diagram recorded at 20 Gbps with $V_{pp} = 1.7$ V, corresponding to modulation energy of 45 fJ/bit.

METHODS

Device fabrication

Single crystalline $BaTiO_3$ was deposited on top of an epitaxial 4-nm-thick STO seed layer by molecular beam epitaxy on 8" SOI wafers with 220-nm-thick device silicon layer for SiN-based devices, and on 2" SOI wafers with 100-nm-thick device silicon for Si-based devices, following a process described elsewhere [96]. Direct wafer bonding was used to transfer the $BaTiO_3$ and device Si layers onto high-resistivity Si wafers capped with a 3-µm-thick thermal oxide. Specifics of the direct wafer bonding process can be found in ref. [96].

For SiN-based waveguides the device Si layer was removed by dry etching, followed by chemical vapor deposition of SiN. The waveguide layer (Si or

SiN) was patterned by dry etching. After waveguide patterning, a combination of SiO_2 cladding deposition, via etching, and metallisation was used to form the final cross-section. Intermediate annealing steps were used to reduce propagation losses.

The SiN-based waveguides use an 80-nm-thick $BaTiO_3$ layer, and 150-nm-thick SiN layer. The strip-waveguide width is 1.1 μm. The electrode-to-electrode gap is 9 μm. The Si strip-waveguides were fabricated using 225-nm-thick $BaTiO_3$ and 100-nm-thick Si. The waveguide width is 0.75 μm, and the electrode-to-electrode gap is 2.3 μm.

Cryogenic measurements

The cryogenic electro-optic measurements were performed in a Lakeshore CPX cryogenic probe station, fitted with RF (40 GHz BW, K-type connectors) and optical feed-throughs. DC and RF signals were applied to the devices using RF probes, and optical coupling was achieved using a fibre array with polarisation maintaining fibres for 1550 nm. A tuneable laser (EXFO T100S-HP) and power meter were used to record transmission spectra (EXFO CT440). The cryogenic electrical measurements were performed in a Janis cryogenic probe station equipped with DC probes. Current-voltage and capacitance-voltage measurements were performed using a parameter analyser. Both cryogenic probe stations were cooled by liquid helium to a base temperature of 4.2 K.

DC EO characterisation

The DC electro-optic response was extracted by applying a voltage to the electrodes of a racetrack resonator and measuring the shift in resonance wavelength ($\Delta\lambda$), compared to the unbiased case, as a function of the applied voltage. From the measured wavelength shift, the change in $BaTiO_3$ refractive index (Δn_{BTO}) can be estimated as

$$\Delta n_{\mathrm{BTO}} = \frac{\lambda_0 \cdot \Delta\lambda}{FSR \cdot L_{\mathrm{E}} \cdot \Gamma_{\mathrm{BTO}}} \tag{E.1}$$

where Γ_{BTO} is the optical confinement in $BaTiO_3$, FSR is the free spectral range of the resonator, L_{E} is the electrode length, and λ_0 is the resonance

wavelength with no voltage. [96] The effective Pockels coefficient, r_{eff}, was then determined according to the procedure described in SN 2.

RF frequency response

To measure the EO frequency response (EO S_{21}) a vector network analyser (VNA, Keysight PNA 50 GHz) was used to apply the electrical stimulus to a $BaTiO_3$ ring modulator. The modulated optical signal was applied to a photodiode (Newport 1024) and the response recorded by the VNA. Electrical calibration was performed before the measurement, and the response of the photodetector was compensated for the data analysis. While the VNA could generate signals up to 50 GHz, the bandwidth of the photodetector was 26 GHz, which in combination with large frequency-dependent electrical losses in the cryogenic probe station (SN 6) makes it impossible to measure the bandwidth beyond 30 GHz.

Devices for data modulation

For data modulation experiments, devices with Si strip-waveguide were used. The racetrack resonator that was used had a bending radius of 15 μm and straight sections of 30 μm.

Data modulation experiments

The electrical signal was generated using an arbitrary waveform generator. A pseudo-random bit stream of $2^7 - 1$ bits was used for modulation. The electrical signal was pre-distorted to compensate for the finite time-response of the electrical signal path (SN 6). The signal was amplified using a RF amplifier and sent to the cryogenic setup, with an estimated voltage swing on the device of 1.7 V (SN 6). A Pritel FA-23 EDFA was used to amplify the modulated optical signal which was applied to a photo diode and recorded on an oscilloscope.

ACKNOWLEDGMENTS

This work has received funding from the European Commission under grant agreements no. H2020-ICT-2015-25- 688579 (PHRESCO) and H2020-ICT-2017-1-780997 (plaCMOS), from the Swiss State Secretariat for Education,

Research and Innovation under contract no. 15.0285 and 16.0001, from the Swiss National Foundation project no 200021_159565 PADOMO, from EPSRC grants EP/L024020/1, EP/M013472/1, and EP/K033085/1, the UK EPSRC grant QuPIC (EP/N015126/1), and ERC grant 2014-STG 640079. JB thanks Dr. Döndü Sahin for her assistance with the experimental setup.

SUPPLEMENTARY INFORMATION

Supplementary Note 1 – Propagation losses

To investigate whether there is any significant contribution to propagation losses from the $BaTiO_3$ (BTO) layer we fabricated different length waveguide structures of identical dimensions with and without the $BaTiO_3$ layer present. The non-distinguishable (within error) propagation losses in both structures (Figure E.5a) indicates that the propagation losses of our devices are limited by our SiN waveguide fabrication process. This conclusion is corroborated by the fact that losses are lower in the Si-$BaTiO_3$ waveguides which uses a fabrication process-flow that has undergone greater optimisation in our cleanroom. Since SiN waveguides with much lower propagation losses can in principle be manufactured [201], the SiN-$BaTiO_3$ waveguide losses are expected to be improved significantly with an improved fabrication process.

The fixed loss per unit length of the waveguide structures leads us to believe that sidewall roughness is the dominant cause of loss in our devices. It is expected therefore that the loss should be temperature independent. To verify this we measured the propagation loss of SiN-$BaTiO_3$ devices at 4 K and compared the device results with room temperature (300 K) and found no difference (Figure E.5b).

Supplementary Note 2 – Determination of r_{eff}

We extract the effective Pockels coefficient of $BaTiO_3$ from the measurements of nonlinear optical hysteresis in Δn_{BTO} as a function of electric field. The ferroelectric hysteresis of $BaTiO_3$ is directly related to Δn_{BTO} through the fraction of poled domains, ν, according to:

$$\Delta n_{\text{BTO}} = -\frac{1}{2} r_{\text{eff}} \nu n_{0,\text{BTO}}^3 E \tag{E.2}$$

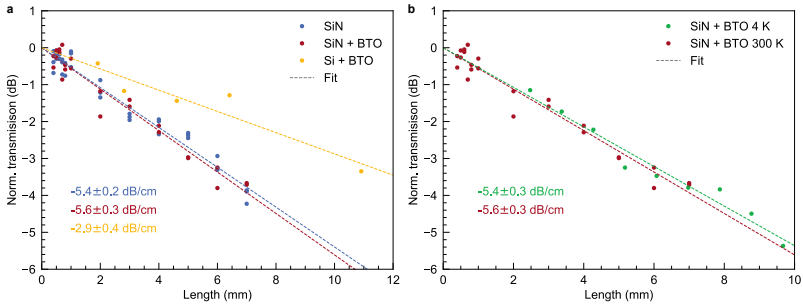

FIGURE E.5: Cut-back loss-measurements of (a) SiN and SiN-$BaTiO_3$ and Si-$BaTiO_3$ waveguides showing no measurable losses caused by $BaTiO_3$, and (b) SiN-$BaTiO_3$ waveguides at 300 K and 4 K showing no change in losses with temperature.

where E is the applied electric field, and $n_{0,\mathrm{BTO}}$ is the refractive index of $BaTiO_3$ with no field applied. The poling fraction of a ferroelectric material can be described by [202]:

$$\nu = \frac{\sinh(A(E \pm E_C))}{A/B - 1 + \cosh(A(E \pm E_C))} \tag{E.3}$$

where EC is the coercive field, A and B are material parameters [202]. Inserting the expression for ν in eq. (E.2) we can determine the material parameters in eq. (E.3) as well as r_{eff} by fitting to the measured Δn_{BTO}. To model the optical response at large electric fields, we introduced a parameter, k, for the third-order nonlinear optical response:

$$\Delta n_{\mathrm{BTO}} = -\frac{1}{2} r_{\mathrm{eff}} \nu n_{0,\mathrm{BTO}}^3 E + kE^2 \tag{E.4}$$

In this work we derived the Pockels coefficients from our data using eq. (E.4) as the fit. An example of the quality of the fit is shown in Figure E.6; the fitting parameters of which are given in Table E.1.

Supplementary Note 3 – Electrical characterisation

Electrical I-V and C-V measurements were performed on dedicated test structures consisting of 2-mm-long electrodes separated by 1.25 μm (C-V)

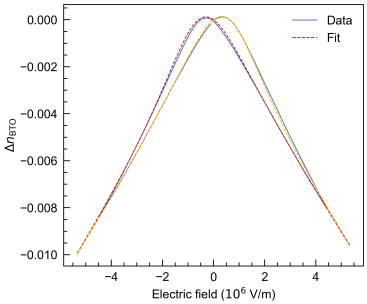

FIGURE E.6: NLO hysteresis measured in a $BaTiO_3$-SiN device at 300 K and the fitted model based on equation (E.4).

TABLE E.1: Parameters for the fit showed in Figure E.6. $n_{0,BTO}$ was fixed to 2.29 based on ellipsometry measurements at room temperature.

r_{eff} (pm/V)	E_C (MV/m)	A (μm/V)	B (μV/m)	k (10^{-18} m^2/V^2)
321	0.606	1.09	0.762	16.7

or 2 μm (I-V) which were patterned on top of 80-nm-thick $BaTiO_3$. The test structures were mounted in a cryogenic probe station and characterised at temperatures in the range 4 K to 300 K. At 4 K, the current measured in the I-V sampling is dominated by capacitive charging and ferroelectric switching. Above 150 K, thermally activated leakage current starts to dominate (Figure E.7). The leakage mechanism in titanate perovskites such as $BaTiO_3$ can typically be described by a modified Schottky emission equation [203] which describes a thermally activated charge transport. Indeed, we observe such thermal activation for temperatures above 150 K. Below that temperature, the experimentally measured leakage is linked to ferroelectric switching currents and capacitive charging.

The different contributions to the measured current and their relation to ferroelectric switching are illustrated in Figure E.8. ① When the applied field is at a maximum the material domains and dielectric are fully polarised and the current flowing is only that associated with leakage. ② When the applied field is reduced to zero (a fraction of) the ferroelectric domains alone remain polarised. ③ When a small opposing field is applied the ferroelectric domains begin to switch their polarisation, the dielectric is also charging and these combine to form a current maximum. ④ The material

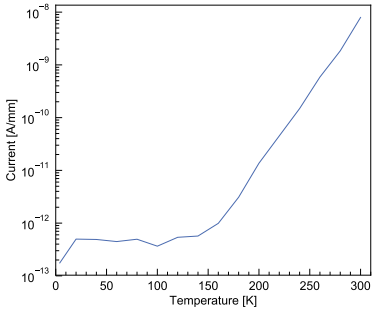

FIGURE E.7: Leakage current through $BaTiO_3$ at various temperatures showing a reduction by more than 10^4 from 300 K to 4 K.

is now in the reversed state to ① and the current is dominated by a leakage current flowing in the reverse direction.

Supplementary Note 4 – Field induced phase transition

As described in the main manuscript, the electrical and electro-optic data suggests the presence of a field-induced phase transition in $BaTiO_3$ at temperatures below ∼100 K (Figure E.3). At temperatures below 100 K, the electro-optic response of the device changes sign when the electric-field strength exceeds 10-15 $\times$ 10^4 V/cm (Figure E.9). This change indicates the appearance of negative elements in the Pockels tensor, which can only be caused by a change in the crystal symmetry – a phase transition.

Indeed, in the case of the phase transitions of bulk $BaTiO_3$ the low-temperature transition from orthorhombic (space group $Pmn2_1$) to rhombohedral (space group R3m) structure includes the appearance of negative elements (r_{22}) [84]:

$$\begin{pmatrix} 0 & 0 & r_{13} \\ 0 & 0 & r_{23} \\ 0 & 0 & r_{33} \\ 0 & r_{42} & 0 \\ r_{51} & 0 & 0 \\ 0 & 0 & 0 \end{pmatrix}_{Pmn2_1} \Rightarrow \begin{pmatrix} 0 & -r_{22} & r_{13} \\ 0 & r_{22} & r_{13} \\ 0 & 0 & r_{33} \\ 0 & r_{42} & 0 \\ r_{42} & 0 & 0 \\ -r_{22} & 0 & 0 \end{pmatrix}_{R3m} \tag{E.5}$$

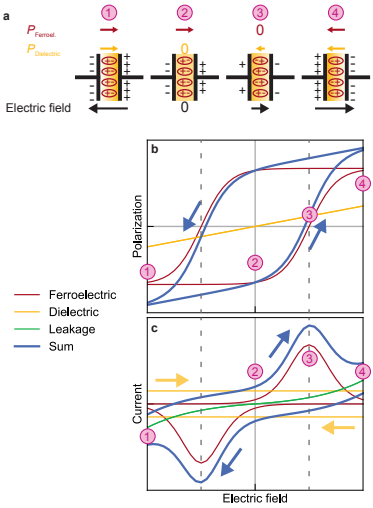

FIGURE E.8: Change in polarisation and resulting electrical current in $BaTiO_3$ capacitors. (a) Polarisation states in ferroelectric capacitor at different field strengths. (b) The calculated polarisation and, c, current showing contributions from ferroelectric domain switching, dielectric charging, and leakage.

A transition to a rhombohedral phase at large electric fields, something not observed in bulk $BaTiO_3$, could trigger the change in the electro-optic behaviour as described above. Phase transitions are also expected to affect the dielectric properties of a material and we expect to see a peak or kink in permittivity around the phase transition temperature. Because of the micro-domain structure of $BaTiO_3$ thin-films, such peaks can be significantly broadened. C-V data (as shown in Figure E.2e) acquired at various temperatures was used to extract the permittivity of the $BaTiO_3$ layer. The permittivity was extracted by performing electro-static simulations where the $BaTiO_3$ permittivity was varied to match the measured capacitance as described in more detail in the supplementary information of ref. [96].

Indeed, we observe a kink in the permittivity at large bias fields around 100 K (Figure E.10). We can also see that there is a peak around 240 K, corresponding to the phase transition observed in the temperature dependent EO response (Figure E.3)

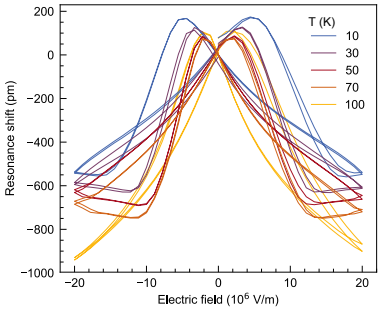

FIGURE E.9: Induced resonance shift at various temperatures from 10 to 100 K in a device oriented along the 45° direction ($BaTiO_3$[011]) showing evidence of a field-induced phase transition below 100 K at electric field strength of 10-15 $\times$ 10^4 V/cm.

Supplementary Note 5 – Switching energy

The Mach-Zehnder interferometer (MZI) used for switching (Figure E.4a,b) consists of 500 μm long electrodes separated by 9 μm. Mapping our experimentally determined capacitance values (Figure E.2e) to the geometry of the MZI results in a total device capacitance of ∼11 fF. For a full π phase shift ±50 V are applied to the device, resulting in a switching energy of $CV^2 = 28$ pJ. Optimisation of the device geometry using thicker $BaTiO_3$ (240 nm) to increase the optical overlap (∼55 %), a smaller electrode gap (4.5 μm), and a longer phase shifter (1 mm) would reduce the voltage by a factor 12 while simultaneously increasing the capacitance by a factor 12. These changes would be expected to result in a reduction of the switching energy to only 2.3 pJ.

Highly-doped p-n junctions cannot be used for low-loss switching because of the large propagation losses and the simultaneous modulation of the (real part of the) refractive index and the absorption. Thermo-optic switches do not have such optical loss issues and are better suited for switching. However, in thermo-optic switches the power consumption is dominated by the static current through the device. It is therefore necessary to specify the time needed for switching the state of the device. Due to the low bandwidth, thermo-optic devices are typically limited to ∼1 μs switching speed. Switching at this time scale corresponds to the lowest switching energy that can be achieved. During that switching period the switch will require ∼0.25 μJ, assuming $P_\pi = 0.5$ W [127] and 50 % of the maximum

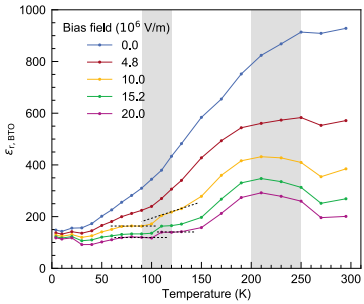

FIGURE E.10: Temperature dependence of $BaTiO_3$ permittivity at different electric-field strengths. A clear peak around 240 K is observed for all field-strengths, and at high field strengths a kink appears around 100 K, matching the phase transitions observed in the electro-optic response (Figure E.3). The kinks in the 10 and 20 MV/m curves are indicated by dashed lines. The grey areas indicate the temperature regions of the two phase-transitions.

current as average current applied during the switching operation. The switching energy of 0.25 μJ is $\sim 10^4$ times larger than the value we report for $BaTiO_3$ device, and 10^5 times larger than the value expected for an optimised $BaTiO_3$ device. Please note that in addition to this dynamic switching energy, also the static power consumption needed to hold the state requires significant power in thermo-optic devices ($\sim$0.5 W) and is almost negligible (<10 pW) in $BaTiO_3$-based switches.

Supplementary Note 6 – Data modulation experiment

The cryogenic probe station used in the experiments is equipped with dual RF connections for sending a signal to a GSGSG RF probe mounted inside the system. In order to account for the impact of this connection on the electro-optical measurements, we carefully characterised the electrical performance of the RF connectors both by measuring the frequency response, and by sending data signals. We used a dedicated sample with metal lines similar to those used in the EO devices to connect the signal lines of the GSGSG probe inside the probe station. The S_{21} parameter in that configuration show an attenuation of 10-20 dB in the frequency range of 10-30 GHz when the signal is transmitted through the cryogenic probe station (Figure E.11). We compensate for the attenuation in the S-parameter measurements of the photonic devices (Figure E.2c) by calibrating the setup

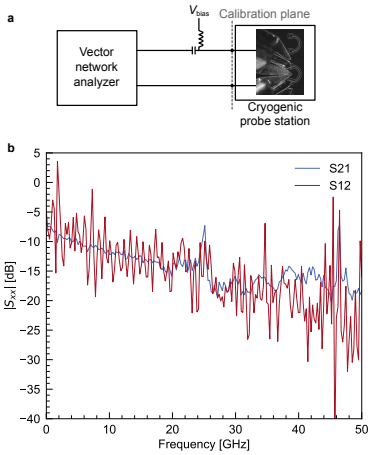

FIGURE E.11: *S*-parameter measurements of the transmission through the cryogenic probe station. (a) The experimental configuration used to perform the measurements. The calibration plane was adjusted to the connections to the cryostat. (b) The measured transmission *S*-parameters through the cryostat. We observe large frequency dependent losses with 10-15 dB attenuation in the 10-20 GHz range.

using a calibration kit. For data transmission measurements (see below) such calibration is not possible.

To evaluate the performance of the $BaTiO_3$ photonic modulator, we analysed the signal integrity and estimated the actual voltage applied to the electrodes of the modulator when performing data modulation experiments.

As discussed above, RF losses in the setup severely impact the electrical signal applied to the metal lines in the sample. We compensated for part of bandwidth limitations in the electrical path by pre-distorting the electrical signal generated in an arbitrary waveform generator (AWG) (Figure E.12a). However, the electrical eye diagram still shows significant noise and a limited time-response which indicates the limitations to our electro-optical characterisation setup.

By comparing the magnitude of the electrical signal transmitted through the cryogenic probe station (as described in Figure E.12), with and without amplification, to the magnitude of the source output, we could determine the contributions of the individual components in the setup (Figure E.12b). Based on the contributions of the individual components in the setup, we

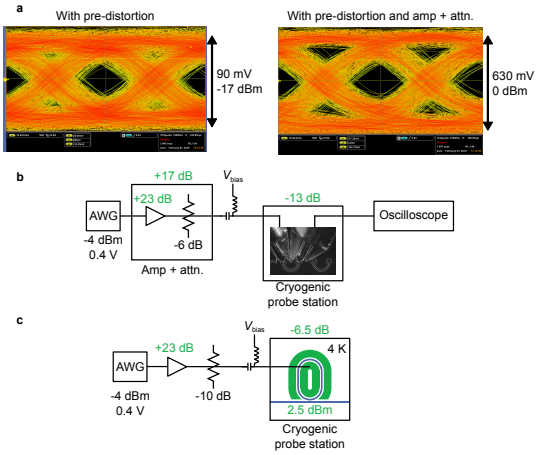

FIGURE E.12: Characterisation of modulation voltage in cryogenic probe station. (a) By measuring the signal amplitude after being sent through the cryogenic probe station, with and without amplification we can extract the contribution of the individual components in the system. (b) We find that the RF amplifier provides 23 dB of gain, and that transmitting the signal through the cryogenic probe station an attenuation of -13 dB. (c) We can extract the real drive voltage based on the values for the RF amplifier and the cryogenic probes station. Assuming equal losses in to and out of the probe station results in 6.5 dB attenuation of the RF signal at the device. Combing all gain/attenuation values results in 2.5 dBm RF power on the device, which corresponds to $\sim$1.7 V_{pp} on an open termination.

can extract the real drive voltage applied to the device during the electro-optic data modulation experiments. We estimate the drive voltage applied to the EO modulator to be V_{pp} $\sim$1.7 V (Figure E.12c). Using an estimated device capacitance of 62 fF (based on an identical sample stack used in ref. [96] and assuming the same reduction of permittivity with temperature as observed in this work), we determine the modulation energy to be 45 fJ/bit according to

$$E_{bit} = \frac{1}{4} C V^2 \tag{E.6}$$

BIBLIOGRAPHY

1. Cisco. *Cisco Global Cloud Index: Forecast and Methodology, 2016–2021* tech. rep. (2018).
2. Boyd, J. T., Wu, R. W., Zelmon, D. E., Naumaan, A., Timlin, H. A. & Jackson, H. E. *Planar And Channel Optical Waveguides Utilizing Silicon Technology* in *Proc. SPIE* (1985), 0517 – 0517.
3. Zhu, H., Zhou, L., Wang, T., Liu, L., Wong, C., Zhou, Y., Yang, R., Li, X. & Chen, J. Optimized silicon QPSK modulator with 64-Gb/s modulation speed. *IEEE Photonics Journal* **7** (2015).
4. Liao, L., Samara-Rubio, D., Morse, M., Liu, A., Hodge, D., Rubin, D., Keil, U. & Franck, T. High speed silicon Mach-Zehnder modulator. *Optics Express* **13**, 3129 (2005).
5. Liao, L., Liu, A., Rubin, D., Basak, J., Chetrit, Y., Nguyen, H., Cohen, R., Izhaky, N. & Paniccia, M. 40 Gbit/s silicon optical modulator for high-speed applications. *Electronics Letters* **43**, 1196 (2007).
6. Marris-Morini, D., Vivien, L., Fédéli, J. M., Cassan, E., Lyan, P. & Laval, S. Low loss and high speed silicon optical modulator based on a lateral carrier depletion structure. *Optics Express* **16**, 334 (2008).
7. Spector, S. J., Geis, M. W., Zhou, G.-R., Grein, M. E., Gan, F., Popović, M. A., Yoon, J. U., Lennon, D. M., Ippen, E. P., Kärtner, F. X. & Lyszczarz, T. M. CMOS-compatible dual-output silicon modulator for analog signal processing. *Optics Express* **16**, 11027 (2008).
8. Kim, G., Park, J. W., Kim, I. G., Kim, S., Kim, S., Lee, J. M., Park, G. S., Joo, J., Jang, K.-S., Oh, J. H., Kim, S. A., Kim, J. H., Lee, J. Y., Park, J. M., Kim, D.-W., Jeong, D.-K., Hwang, M.-S., Kim, J.-K., Park, K.-S., Chi, H.-K., Kim, H.-C., Kim, D.-W. & Cho, M. H. Low-voltage high-performance silicon photonic devices and photonic integrated circuits operating up to 30 Gb/s. *Optics Express* **19**, 26936 (2011).
9. Gardes, F. Y., Thomson, D. J., Emerson, N. G. & Reed, G. T. 40 Gb/s silicon photonics modulator for TE and TM polarisations. *Optics Express* **19**, 11804 (2011).
10. Korn, D., Yu, H., Hillerkuss, D., Alloatti, L., Mattern, C., Komorowska, K., Bogaerts, W., Baets, R., Van Campenhout, J., Verheyen, P., Wouters, J., Moelants, M., Absil, P., Koos, C., Freude, W. & Leuthold, J. *Detection or Modulation at 35 Gbit/s with a Standard CMOS-processed Optical*

Waveguide in *Conference on Lasers and Electro-Optics 2012* (Optical Society of America, San Jose, California, 2012), CTu1A.1.

11. Yu, H., Pantouvaki, M., Van Campenhout, J., Korn, D., Komorowska, K., Dumon, P., Li, Y., Verheyen, P., Absil, P., Alloatti, L., Hillerkuss, D., Leuthold, J., Baets, R. & Bogaerts, W. Performance tradeoff between lateral and interdigitated doping patterns for high speed carrier-depletion based silicon modulators. *Optics Express* **20**, 12926 (2012).
12. Ding, J., Chen, H., Yang, L., Zhang, L., Ji, R., Tian, Y., Zhu, W., Lu, Y., Zhou, P., Min, R. & Yu, M. Ultra-low-power carrier-depletion Mach-Zehnder silicon optical modulator. *Optics Express* **20**, 7081 (2012).
13. Dong, P., Chen, L. & Chen, Y.-k. High-speed low-voltage single-drive push-pull silicon Mach-Zehnder modulators. *Optics Express* **20**, 6163 (2012).
14. Ding, R., Liu, Y., Li, Q., Yang, Y., Ma, Y., Padmaraju, K., Lim, A. E.-J., Lo, G.-Q., Bergman, K., Baehr-Jones, T. & Hochberg, M. Design and characterization of a 30-GHz bandwidth low-power silicon traveling-wave modulator. *Optics Communications* **321**, 124 (2014).
15. Patel, D., Ghosh, S., Chagnon, M., Samani, A., Veerasubramanian, V., Osman, M. & Plant, D. V. Design, analysis, and transmission system performance of a 41 GHz silicon photonic modulator. *Optics Express* **23**, 14263 (2015).
16. Samani, A., Chagnon, M., Patel, D., Veerasubramanian, V., Ghosh, S., Osman, M., Zhong, Q. & Plant, D. V. A Low-Voltage 35-GHz Silicon Photonic Modulator-Enabled 112-Gb/s Transmission System. *IEEE Photonics Journal* **7**, 1 (2015).
17. Zhou, Y., Zhou, L., Zhu, H., Wong, C., Wen, Y., Liu, L., Li, X. & Chen, J. Modeling and optimization of a single-drive push-pull silicon Mach-Zehnder modulator. *Photonics Research* **4**, 153 (2016).
18. Vermeulen, D., Aroca, R., Chen, L., Pellach, L., McBrien, G. & Doerr, C. Demonstration of Silicon Photonics Push–Pull Modulators Designed for Manufacturability. *IEEE Photonics Technology Letters* **28**, 1127 (2016).
19. Petousi, D., Rito, P., Lischke, S., Knoll, D., Garcia-Lopez, I., Kroh, M., Barth, R., Mai, C., Ulusoy, A., Peczek, A., Winzer, G., Voigt, K., Kissinger, D., Petermann, K. & Zimmermann, L. Monolithically Integrated High-Extinction-Ratio MZM With a Segmented Driver in Photonic BiCMOS. *IEEE Photonics Technology Letters* **28**, 2866 (2016).

20. Li, M., Wang, L., Li, X., Xiao, X. & Yu, S. Silicon intensity Mach-Zehnder modulator for single lane 100 Gb/s applications. *Photonics Research* **6**, 109 (2018).
21. Zhou, J., Zhang, Q., Wang, J., Zhu, L. & Hong, J. *Model and design of silicon photonic carrier-depletion Mach-Zehnder modulators for 400Gb/s and beyond PAM and QAM applications* in *SPIE OPTO Silicon Photonics XIV* **10923** (2019).
22. El-Fiky, E., Samani, A., Patel, D., Jacques, M., Sowailem, M. & Plant, D. V. 400 Gb/s O-band silicon photonic transmitter for intra-datacenter optical interconnects. *Optics Express* **27**, 10258 (2019).
23. Zhou, G., Zhou, L., Zhou, Y., Zhong, Y., Liu, S., Guo, Y., Liu, L. & Chen, J. *Silicon Mach-Zehnder modulator using a highly-efficient L-shape PN junction* in *Tenth International Conference on Information Optics and Photonics (CIOP 2018)* **10964** (2018).
24. Ma, Y., Williams, C., Ahmed, M., Elmoznine, A., Lim, D., Liu, Y., Shi, R., Huynh, T., Roman, J., Ahmed, A., Vera, L., Chen, Y., Horth, A., Guan, H., Padmaraju, K., Streshinsky, M., Novack, A., Sukkar, R., Younce, R., Rylyakov, A., Scordo, D. & Hochberg, M. *An all-silicon transmitter with co-designed modulator and DC-coupled driver* in *Optical Fiber Communication Conference (OFC) 2019* (Optical Society of America, San Diego, California, 2019), Tu2A.2.
25. Lin, J., Sepehrian, H., Rusch, L. A. & Shi, W. *CMOS-Compatible Silicon Photonic IQ Modulator for 84 Gbaud 16QAM and 70 Gbaud 32QAM* in *Optical Fiber Communication Conference* (Optical Society of America, San Diego, California, 2018), Tu2E.4.
26. Van Campenhout, J., Ban, Y., De Heyn, P., Srinivasan, A., De Coster, J., Lardenois, S., Snyder, B., Balakrishnan, S., Lepage, G., Golshani, N., Janssen, S., Lesniewska, A., Croes, K., Miller, A., Verheyen, P., Pantouvaki, M. & Absil, P. *Silicon Photonics for 56G NRZ Optical Interconnects* in *Optical Fiber Communication Conference* (Optical Society of America, San Diego, California, 2018), W1I.1.
27. Soref, R. & Bennett, B. Electrooptical effects in silicon. *IEEE Journal of Quantum Electronics* **23**, 123 (1987).
28. Thomson, D. J., Gardes, F. Y., Fedeli, J.-M., Zlatanovic, S., Hu, Y., Kuo, B. P. P., Myslivets, E., Alic, N., Radic, S., Mashanovich, G. Z. & Reed, G. T. 50-Gb/s Silicon Optical Modulator. *IEEE Photonics Technology Letters* **24**, 234 (2012).
29. Petousi, D., Zimmermann, L., Gajda, A., Kroh, M., Voigt, K., Winzer, G., Tillack, B. & Petermann, K. Analysis of Optical and Electrical

Tradeoffs of Traveling-Wave Depletion-Type Si Mach–Zehnder Modulators for High-Speed Operation. *IEEE Journal of Selected Topics in Quantum Electronics* **21**, 199 (2015).

30. Han, J.-H., Boeuf, F., Fujikata, J., Takahashi, S., Takagi, S. & Takenaka, M. Efficient low-loss InGaAsP/Si hybrid MOS optical modulator. *Nature Photonics* **11**, 486 (2017).
31. Hiraki, T., Aihara, T., Hasebe, K., Takeda, K., Fujii, T., Kakitsuka, T., Tsuchizawa, T., Fukuda, H. & Matsuo, S. Heterogeneously integrated III–V/Si MOS capacitor Mach–Zehnder modulator. *Nature Photonics* **11**, 482 (2017).
32. Wooten, E. L., Kissa, K. M., Yi-Yan, A., Murphy, E. J., Lafaw, D. A., Hallemeier, P. F., Maack, D., Attanasio, D. V., Fritz, D. J., McBrien, G. J. & Bossi, D. E. A review of lithium niobate modulators for fiber-optic communications systems. *IEEE Journal of Selected Topics in Quantum Electronics* **6**, 69 (2000).
33. Kieninger, C., Kutuvantavida, Y., Elder, D. L., Wolf, S., Zwickel, H., Blaicher, M., Kemal, J. N., Lauermann, M., Randel, S., Freude, W., Dalton, L. R. & Koos, C. Ultra-high electro-optic activity demonstrated in a silicon-organic hybrid modulator. *Optica* **5**, 1 (2018).
34. Damas, P., Roux, X. L., Bourdais, D. L., Cassan, E., Marris-morini, D., Izard, N., Maroutian, T., Lecoeur, P. & Vivien, L. Wavelength dependence of Pockels effect in strained silicon waveguides. *Optics Express* **22**, 1693 (2014).
35. Berciano, M., Marcaud, G., Damas, P., Le Roux, X., Crozat, P., Alonso Ramos, C., Pérez Galacho, D., Benedikovic, D., Marris-Morini, D., Cassan, E. & Vivien, L. Fast linear electro-optic effect in a centrosymmetric semiconductor. *Communications Physics* **1**, 64 (2018).
36. Castellan, C., Trenti, A., Vecchi, C., Marchesini, A., Mancinelli, M., Ghulinyan, M., Pucker, G. & Pavesi, L. On the origin of second harmonic generation in silicon waveguides with silicon nitride cladding. *Scientific Reports* **9**, 1088 (2019).
37. Holman, R. L., Althouse Johnson, L. M. & Skinner, D. P. Desirability of electro-optic materials for guided-wave optics. *Optical Engineering* **26**, 262134 (1987).
38. Bernasconi, P., Zgonik, M. & Gunter, P. Temperature dependence and dispersion of electro-optic and elasto-optic effect in perovskite crystals. *Journal of Applied Physics* **78**, 2651 (1995).
39. George, J. P., Smet, P. F., Botterman, J., Bliznuk, V., Woestenborghs, W., Van Thourhout, D., Neyts, K. & Beeckman, J. Lanthanide-Assisted

Deposition of Strongly Electro-optic PZT Thin Films on Silicon: Toward Integrated Active Nanophotonic Devices. *ACS Applied Materials & Interfaces* **7**, 13350 (2015).

40. Zgonik, M., Bernasconi, P., Duelli, M., Schlesser, R., Günter, P., Garrett, M. H., Rytz, D., Zhu, Y., Wu, X., Günter, P., Garrett, M. H., Rytz, D., Zhu, Y. & Wu, X. Dielectric, elastic, piezoelectric, electro-optic, and elasto-optic tensors of $BaTiO_3$ crystals. *Physical Review B* **50**, 5941 (1994).
41. Berseth, C. A., Wuethrich, C. & Reinhart, F. K. The electro-optic coefficients of GaAs: Measurements at 1.32 and 1.52 μm and study of their dispersion between 0.9 and 10 μm. *Journal of Applied Physics* **71**, 2821 (1992).
42. Nikogosyan, D. N. *Nonlinear Optical Crystals : A Complete Survey* (Springer, New York, NY, United States, 2005).
43. Wessels, B. W. Ferroelectric Epitaxial Thin Films for Integrated Optics, 659 (2007).
44. McKee, R. a., Walker, F. J., Conner, J. R., Specht, E. D. & Zelmon, D. E. Molecular beam epitaxy growth of epitaxial barium silicide, barium oxide, and barium titanate on silicon. *Applied Physics Letters* **59**, 782 (1991).
45. Gill, D. M., Block, B. A., Conrad, C. W., Wessels, B. W. & Ho, S. T. Thin film channel waveguides fabricated in metalorganic chemical vapor deposition grown $BaTiO_3$ on MgO. *Applied Physics Letters* **69**, 2968 (1996).
46. Petraru, A., Schubert, J., Schmid, M. & Buchal, C. Ferroelectric $BaTiO_3$ thin-film optical waveguide modulators. *Applied Physics Letters* **81**, 1375 (2002).
47. Abel, S., Stöferle, T., Marchiori, C., Caimi, D., Czornomaz, L., Rossel, C., Rossell, M. D., Erni, R., Sousa, M., Siegwart, H., Hofrichter, J., Stuckelberger, M., Chelnokov, A., Offrein, B. J. & Fompeyrine, J. *Electro-Optical Active Barium Titanate Thin Films in Silicon Photonics Devices* in *Advanced Photonics 2013* (Optical Society of America, Rio Grande, Puerto Rico, 2013), IW4A.5.
48. Xiong, C., Pernice, W., Ngai, J., Reiner, J., Kumarh, D., Walker, F., Ahn, C. & Tang, H. Active silicon integrated nanophotonics : ferroelectric $BaTiO_3$ devices. *Nano Letters* **14**, 1419 (2014).
49. Abel, S., Stoeferle, T., Marchiori, C., Caimi, D., Czornomaz, L., Stuckelberger, M., Sousa, M., Offrein, B. & Fompeyrine, J. A hybrid barium

titanate-silicon photonics platform for ultra-efficient electro-optic tuning. *Journal of Lightwave Technology* **34**, 1688 (2015).

50. De Dobbelaere, P., Dahl, A., Mekis, A., Chase, B., Weber, B., Welch, B., Foltz, D., Armyo, G., Masim, G., McGee, G., Wong, G., Balardeta, J., Dotson, J., Schramm, J., Hon, K., Khauv, K., Robertson, K., Stechschulte, K., Yokoyama, K., Planchon, L., Tullgren, L., Eker, M., Mack, M., Peterson, M., Rudmck, N., Milton, P., Sun, P., Bruck, R., Zhou, R., Denton, S., Fathpour, S., Gloeckner, S., Jackson, S., Pang, S., Sahni, S., Wang, S., Yu, S., Pmguet, T., De Koninck, Y., Chi, Y. & Liang, Y. *Advanced silicon photonics technology platform leveraging a semiconductor supply chain* in *2017 IEEE International Electron Devices Meeting (IEDM)* (2017), 34.1.1.
51. Abel, S., Stöferle, T., Marchiori, C., Rossel, C., Rossell, M. D., Erni, R., Caimi, D., Sousa, M., Chelnokov, A., Offrein, B. J. & Fompeyrine, J. A strong electro-optically active lead-free ferroelectric integrated on silicon. *Nature Communications* **4**, 1671 (2013).
52. Deshpande, V., Hahn, H., O'Connor, E., Baumgartner, Y., Sousa, M., Caimi, D., Boutry, H., Widiez, J., Brévard, L., Le Royer, C., Vinet, M., Fompeyrine, J. & Czornomaz, L. *First demonstration of 3D SRAM through 3D monolithic integration of InGaAs n-FinFETs on FDSOI Si CMOS with inter-layer contacts* in *2017 Symposium on VLSI Technology* (2017), T74.
53. Tong, Q. Y., Cha, G., Gafiteanu, R. & Gosele, U. Low Temperature Wafer Direct Bonding. *Journal of Microelectromechanical Systems* **3**, 29 (1994).
54. Daix, N., Uccelli, E., Czornomaz, L., Caimi, D., Rossel, C., Sousa, M., Siegwart, H., Marchiori, C., Hartmann, J. M., Shiu, K.-T., Cheng, C.-W., Krishnan, M., Lofaro, M., Kobayashi, M., Sadana, D. & Fompeyrine, J. Towards large size substrates for III-V co-integration made by direct wafer bonding on Si. *APL Materials* **2**, 086104 (2014).
55. Acosta, M., Novak, N., Rojas, V., Patel, S., Vaish, R., Koruza, J., Rossetti, G. A. & Rödel, J. $BaTiO_3$-based piezoelectrics: Fundamentals, current status, and perspectives. *Applied Physics Reviews* **4** (2017).
56. McKee, R. A., Walker, F. J. & Chisholm, M. F. Crystalline oxides on silicon: The first five monolayers. *Physical Review Letters* **81**, 3014 (1998).
57. Li, H., Hu, X., Wei, Y., Yu, Z., Zhang, X., Droopad, R., Demkov, A. A., Edwards, J., Moore, K., Ooms, W., Kulik, J. & Fejes, P. Two-

dimensional growth of high-quality strontium titanate thin films on Si. *Journal of Applied Physics* **93**, 4521 (2003).

58. Warusawithana, M. P., Cen, C., Sleasman, C. R., Woicik, J. C., Li, Y., Kourkoutis, L. F., Klug, J. A., Li, H., Ryan, P., Wang, L.-P., Bedzyk, M., Muller, D. A., Chen, L.-Q., Levy, J. & Schlom, D. G. A Ferroelectric Oxide Made Directly on Silicon. *Science* **324**, 367 LP (2009).
59. Diaz-Fernandez, D., Spreitzer, M., Parkelj, T. & Suvorov, D. Multi-stage pulsed laser deposition of high quality epitaxial ultra-thin $SrTiO_3$ on Si substrates. *Applied Surface Science* **455**, 227 (2018).
60. Park, J. W., Baek, S. H., Bark, C. W., Biegalski, M. D. & Eom, C. B. Quasi-single-crystal (001) $SrTiO_3$ templates on Si. *Applied Physics Letters* **95**, 2009 (2009).
61. Först, C. J., Ashman, C. R., Schwarz, K. & Blöchl, P. E. The interface between silicon and a high-k oxide. *Nature* **427**, 53 (2004).
62. Wei, Y., Hu, X., Liang, Y., Jordan, D. C., Craigo, B., Droopad, R., Yu, Z., Demkov, A., Edwards, J. L. & Ooms, W. J. Mechanism of cleaning Si(100) surface using Sr or SrO for the growth of crystalline $SrTiO_3$ films. *Journal of Vacuum Science & Technology B* **20**, 1402 (2002).
63. Karpenko, O. P., Yalisove, S. M. & Eaglesham, D. J. Surface roughening during low temperature Si(100) epitaxy. *Journal of Applied Physics* **82**, 1157 (1997).
64. Wills, L. A., Feil, W. A., Wessels, B. W., Tonge, L. M. & Marks, T. J. Growth studies of ferroelectric oxide layers prepared by organometallic chemical vapor deposition. *Journal of Crystal Growth* **107**, 712 (1991).
65. Reinke, M., Kuzminykh, Y., Eltes, F., Abel, S., Lagrange, T., Neels, A., Fompeyrine, J. & Hoffmann, P. Low Temperature Epitaxial Barium Titanate Thin Film Growth in High Vacuum CVD. *Advanced Materials Interfaces* **4**, 1700116 (2017).
66. Kormondy, K. J., Popoff, Y., Sousa, M., Eltes, F., Caimi, D., Rossell, M. D., Fiebig, M., Hoffmann, P., Marchiori, C., Reinke, M., Trassin, M., Demkov, A. A., Fompeyrine, J. & Abel, S. Microstructure and ferroelectricity of $BaTiO_3$ thin films on Si for integrated photonics. *Nanotechnology* **28**, 075706 (2017).
67. Dubourdieu, C., Bruley, J., Arruda, T. M., Posadas, A., Jordan-Sweet, J., Frank, M. M., Cartier, E., Frank, D. J., Kalinin, S. V., Demkov, A. a. & Narayanan, V. Switching of ferroelectric polarization in epitaxial $BaTiO_3$ films on silicon without a conducting bottom electrode. *Nature Nanotechnology* **8**, 748 (2013).

68. Zaumseil, P. High-resolution characterization of the forbidden Si 200 and Si 222 reflections. *Journal of Applied Crystallography* **48**, 528 (2015).
69. Castera, P., Tulli, D., Gutierrez, A. M. & Sanchis, P. Influence of $BaTiO_3$ ferroelectric orientation for electro-optic modulation on silicon. *Optics Express* **23**, 15332 (2015).
70. Castera, P., Gutierrez, A. M., Tulli, D., Cueff, S., Orobtchouk, R., Romeo, P. R., Saint-Girons, G. & Sanchis, P. Electro-Optical Modulation Based on Pockels Effect in $BaTiO_3$ with a Multi-Domain Structure. *IEEE Photonics Technology Letters* **28**, 990 (2016).
71. Boyd, R. W. *Nonlinear Optics* 3rd (Elsevier Inc., 2008).
72. Denev, S. A., Lummen, T. T. A., Barnes, E., Kumar, A. & Gopalan, V. Probing ferroelectrics using optical second harmonic generation. *Journal of the American Ceramic Society* **94**, 2699 (2011).
73. Trassin, M., Luca, G. D., Manz, S. & Fiebig, M. Probing ferroelectric domain engineering in $BiFeO_3$ thin films by second harmonic generation. *Advanced Materials* **27**, 4871 (2015).
74. Weber, M. J. *Handbook of Optical Materials* 1st (CRC Press, Boca Raton, 2002).
75. Cardona, M. Optical properties and band structure of $SrTiO_3$ and $BaTiO_3$. *Physical Review* **140**, 651 (1965).
76. Tang, P., Towner, D. J., Meier, A. L. & Wessels, B. W. Low-voltage, polarization-insensitive, electro-optic modulator based on a polydomain barium titanate thin film. *Applied Physics Letters* **85**, 4615 (2004).
77. Abel, S. *Electro-optic photonic devices based on epitaxial barium titanate thin films on silicon* PhD thesis (Université de Grenoble, 2014).
78. Baehr-Jones, T., Ding, R., Liu, Y., Ayazi, A., Pinguet, T., Harris, N. C., Streshinsky, M., Lee, P., Zhang, Y., Lim, A. E.-J., Liow, T.-Y., Teo, S. H.-G., Lo, G.-Q. & Hochberg, M. Ultralow drive voltage silicon traveling-wave modulator. *Optics Express* **20**, 12014 (2012).
79. Ylivaara, O. M. E., Liu, X., Kilpi, L., Lyytinen, J., Schneider, D., Laitinen, M., Julin, J., Ali, S., Sintonen, S., Berdova, M., Haimi, E., Sajavaara, T., Ronkainen, H., Lipsanen, H., Koskinen, J., Hannula, S. P. & Puurunen, R. L. Aluminum oxide from trimethylaluminum and water by atomic layer deposition: The temperature dependence of residual stress, elastic modulus, hardness and adhesion. *Thin Solid Films* **552**, 124 (2014).

80. Gösele, U., Tong, Q. Y., Schumacher, A., Kräuter, G., Reiche, M., Plößl, A., Kopperschmidt, P., Lee, T. H. & Kim, W. J. Wafer bonding for microsystems technologies. *Sensors and Actuators A* **74**, 161 (1999).
81. Selvaraja, S. K., Sleeckx, E., Schaekers, M., Bogaerts, W., Thourhout, D. V., Dumon, P. & Baets, R. Low-loss amorphous silicon-on-insulator technology for photonic integrated circuitry. *Optics Communications* **282**, 1767 (2009).
82. Lin, C., Posadas, A., Hadamek, T. & Demkov, A. A. Final-state effect on X-ray photoelectron spectrum of nominally d^1 and n-doped d^0 transition-metal oxides. *Physical Review B : Condensed Matter and Materials Physics* **92**, 035110 (2015).
83. Wang, J. L., Leroy, J., Niu, G., Saint-Girons, G., Gautier, B., Vilquin, B. & Barrett, N. Chemistry and structure of $BaTiO_3$ ultra-thin films grown by different O_2 plasma power. *Chemical Physics Letters* **592**, 206 (2014).
84. Aroyo, M. I., Perez-Mato, J. M., Orobengoa, D., Tasci, E., De La Flor, G. & Kirov, A. Crystallography online: Bilbao crystallographic server. *Bulgarian Chemical Communications* **43**, 183 (2011).
85. Cochard, C., Spielmann, T., Bahlawane, N., Halpin, A. & Granzow, T. Broadband characterization of congruent lithium niobate from mHz to optical frequencies. *Journal of Physics D: Applied Physics* **50** (2017).
86. Bogaerts, W., de Heyn, P., van Vaerenbergh, T., de Vos, K., Kumar Selvaraja, S., Claes, T., Dumon, P., Bienstman, P., van Thourhout, D. & Baets, R. Silicon microring resonators. *Laser and Photonics Reviews* **6**, 47 (2012).
87. Barrios, C. A., Almeida, V. R., Panepucci, R. & Lipson, M. Electrooptic Modulation of Silicon-on-Insulator Submicrometer-Size Waveguide Devices. *Journal of Lightwave Technology* **21**, 2332 (2003).
88. Driscoll, J. B., Sakib, M., Kumar, R., Jayatilleka, H., Sun, J. & Rong, H. A 128 Gb/s PAM4 Silicon Microring Modulator With Integrated Thermo-Optic Resonance Tuning. *Journal of Lightwave Technology* **37**, 110 (2018).
89. Komma, J., Schwarz, C., Hofmann, G., Heinert, D. & Nawrodt, R. Thermo-optic coefficient of silicon at 1550 nm and cryogenic temperatures. *Applied Physics Letters* **101**, 041905 (2012).
90. Miller, C. M. High-Speed Digital Transmitter Characterization Using Eye Diagram Analysis. *Hewlett-Packard Journal* **45**, 29 (1994).
91. Koeber, S., Palmer, R., Lauermann, M., Heni, W., Elder, D. L., Korn, D., Woessner, M., Alloatti, L., Koenig, S., Schindler, P. C., Yu, H., Bogaerts,

W., Dalton, L. R., Freude, W., Leuthold, J. & Koos, C. Femtojoule electro-optic modulation using a silicon–organic hybrid device. *Light: Science & Applications* **4**, e255 (2015).

92. Alexander, K., George, J. P., Verbist, J., Neyts, K., Kuyken, B., Thourhout, D. V. & Beeckman, J. Nanophotonic Pockels modulators on a silicon nitride platform. *Nature Communications* **9**, 3444 (2018).
93. Rabiei, P., Ma, J., Khan, S., Chiles, J. & Fathpour, S. Heterogeneous lithium niobate photonics on silicon substrates. *Optics express* **21**, 114 (2013).
94. Wang, C., Zhang, M., Chen, X., Bertrand, M., Shams-Ansari, A., Chandrasekhar, S., Winzer, P. & Lončar, M. Integrated lithium niobate electro-optic modulators operating at CMOS-compatible voltages. *Nature* **562**, 101 (2018).
95. Eltes, F., Caimi, D., Fallegger, F., Sousa, M., O'Connor, E., Rossell, M. D., Offrein, B., Fompeyrine, J. & Abel, S. Low-loss $BaTiO_3$-Si waveguides for nonlinear integrated photonics. *ACS Photonics* **3**, 1698 (2016).
96. Abel, S., Eltes, F., Ortmann, J. E., Messner, A., Castera, P., Wagner, T., Urbonas, D., Rosa, A., Gutierrez, A. M., Tulli, D., Ma, P., Baeuerle, B., Josten, A., Heni, W., Caimi, D., Czornomaz, L., Demkov, A. A., Leuthold, J., Sanchis, P. & Fompeyrine, J. Large Pockels effect in micro- and nanostructured barium titanate integrated on silicon. *Nature Materials* **18**, 42 (2019).
97. Webster, M., Lakshmikumar, K., Appel, C., Muzio, C., Dama, B. & Shastri, K. *Low-Power MOS-Capacitor Based Silicon Photonic Modulators and CMOS Drivers* in *Optical Fiber Communication Conference* (2015), W4H.3.
98. Koos, C., Leuthold, J., Freude, W., Member, S., Kohl, M., Dalton, L., Member, S., Bogaerts, W., Giesecke, A. L., Lauermann, M., Melikyan, A., Koeber, S., Wolf, S., Weimann, C., Muehlbrandt, S., Koehnle, K., Pfeifle, J., Hartmann, W., Kutuvantavida, Y., Ummethala, S., Palmer, R., Korn, D., Alloatti, L., Schindler, P. C., Elder, D. L., Wahlbrink, T. & Bolten, J. Silicon-Organic Hybrid (SOH) and Plasmonic-Organic Hybrid (POH) Integration. **34**, 256 (2016).
99. Burla, M., Hoessbacher, C., Heni, W., Haffner, C., Fedoryshyn, Y., Werner, D., Watanabe, T., Massler, H., Elder, D., Dalton, L. & Leuthold, J. 500 GHz plasmonic Mach-Zehnder modulator enabling sub-THz microwave photonics. *arXiv:1901.00477* (2018).

100. Haffner, C., Heni, W., Fedoryshyn, Y., Niegemann, J., Melikyan, A., Elder, D. L., Baeuerle, B., Salamin, Y., Josten, A., Koch, U., Hoessbacher, C., Ducry, F., Juchli, L., Emboras, A., Hillerkuss, D., Kohl, M., Dalton, L. R., Hafner, C. & Leuthold, J. All-plasmonic Mach–Zehnder modulator enabling optical high-speed communication at the microscale. *Nature Photonics* **9**, 525 (2015).
101. Hoessbacher, C., Josten, A., Baeuerle, B., Fedoryshyn, Y., Hettrich, H., Salamin, Y., Heni, W., Haffner, C., Kaiser, C., Schmid, R., Elder, D. L., Hillerkuss, D., Möller, M., Dalton, L. R. & Leuthold, J. Plasmonic modulator with >170 GHz bandwidth demonstrated at 100 GBd NRZ. *Optics Express* **25**, 1762 (2017).
102. Baeuerle, B., Heni, W., Fedoryshyn, Y., Hoessbacher, C., Koch, U., Josten, A., Watanabe, T., Uhl, C., Hettrich, H., Elder, D. L., Dalton, L. R., Möller, M. & Leuthold, J. Dual-Drive Plasmonic Transmitter with Co-Designed Driver Electronics operated at 120 GBd On-Off Keying, 10 (2019).
103. Heni, W., Fedoryshyn, Y., Baeuerle, B., Josten, A., Hoessbacher, C., Messner, A., Haffner, C., Salamin, Y., Koch, U., Watanabe, T., Elder, D. L., Dalton, L. R. & Leuthold, J. Sub-fJ/bit Operation of 100 GBd Plasmonic IQ Modulators. **1**, 20 (2019).
104. Melikyan, A., Alloatti, L., Muslija, A., Hillerkuss, D., Schindler, P. C., Li, J., Palmer, R., Korn, D., Muehlbrandt, S., Van Thourhout, D., Chen, B., Dinu, R., Sommer, M., Koos, C., Kohl, M., Freude, W. & Leuthold, J. High-speed plasmonic phase modulators. *Nature Photonics* **8**, 229 (2014).
105. Gupta, T. in *Copper Interconnect Technology* (ed Gupta, T.) 267 (Springer New York, New York, NY, 2009).
106. Shi, Y., Yan, L. & Willner, a. E. High-speed electrooptic modulator characterization using optical spectrum analysis. *Journal of Lightwave Technology* **21**, 2358 (2003).
107. Abel, S., Stark, D. J., Eltes, F., Ortmann, J. E., Caimi, D. & Fompeyrine, J. *Multi-Level Optical Weights in Integrated Circuits* in *2017 IEEE International Conference on Rebooting Computing (ICRC)* (Washington, DC, 2017).
108. Ortmann, J. E., Eltes, F., Caimi, D. & Abel, S. *Electric Field Tuning of $BaTiO_3$-on-Silicon Multi-Ring Resonators via the Pockels Effect* in *2018 IEEE 15th International Conference on Group IV Photonics (GFP)* (2018), 1.

109. Harwood, M. G., Popper, P. & Rushman, D. F. Curie Point of Barium Titanate. *Nature* **160**, 58 (1947).
110. Hoerman, B. H., Ford, G. M., Kaufmann, L. D. & Wessels, B. W. Dielectric properties of epitaxial $BaTiO_3$ thin films. *Applied Physics Letters* **73**, 2248 (1998).
111. Kay, H. F. & Vousden, P. XCV. Symmetry changes in barium titanate at low temperatures and their relation to its ferroelectric properties. *The London, Edinburgh, and Dublin Philosophical Magazine and Journal of Science* **40**, 1019 (1949).
112. Von Hippel, A. Ferroelectricity, domain structure, and phase transitions of barium titanate. *Reviews of Modern Physics* **22**, 221 (1950).
113. Pernice, W. H. P., Schuck, C., Li, M. & Tang, H. X. Carrier and thermal dynamics of silicon photonic resonators at cryogenic temperatures. *Optics Express* **19**, 3290 (2011).
114. Wright, J. B., Trotter, D. C., Zortman, W. A., Lentine, A. L., Shaner, E. A., Watts, M. R., Akturk, A. & Peckerar, M. *Cryogenic Operation of Silicon Photonic Modulators* in *Advanced Photonics Congress* (Optical Society of America, Colorado Springs, Colorado, 2012), IM2A.5.
115. Gambetta, J. M., Chow, J. M. & Steffen, M. Building logical qubits in a superconducting quantum computing system. *npj Quantum Information* **3**, 2 (2017).
116. Holmes, D. S., Ripple, A. L. & Manheimer, M. A. Energy-Efficient Superconducting Computing—Power Budgets and Requirements. *IEEE Transactions on Applied Superconductivity* **23**, 1701610 (2013).
117. Mukhanov, O. A. Energy-Efficient single flux quantum technology. *IEEE Transactions on Applied Superconductivity* **21**, 760 (2011).
118. Ladd, T. D., Jelezko, F., Laflamme, R., Nakamura, Y., Monroe, C. & O'Brien, J. L. Quantum Computing. *Nature* **464**, 45 (2010).
119. Holmes, D. S., Kadi, A. M. & Johnson, M. W. Superconducting Computing in Large-Scale Hybrid Systems. *Computer* **48**, 34 (2015).
120. O'Brien, J. L., Furusawa, A. & Vučković, J. Photonic quantum technologies. *Nature Photonics* **3**, 687 (2009).
121. Silverstone, J. W., Bonneau, D., O'Brien, J. L. & Thompson, M. G. Silicon quantum photonics. *IEEE Journal of Selected Topics in Quantum Electronics* **22**, 6700113 (2016).
122. Wilkes, C. M., Qiang, X., Wang, J., Santagati, R., Paesani, S., Zhou, X., Miller, D. A. B., Marshall, G. D., Thompson, M. G. & O'Brien, J. L. 60 dB high-extinction auto-configured Mach–Zehnder interferometer. *Optics Letters* **41**, 5318 (2016).

123. Fan, L., Zou, C. L., Cheng, R., Guo, X., Han, X., Gong, Z., Wang, S. & Tang, H. X. Superconducting cavity electro-optics: A platform for coherent photon conversion between superconducting and photonic circuits. *Science Advances* **4**, 1 (2018).
124. Javerzac-Galy, C., Plekhanov, K., Bernier, N. R., Toth, L. D., Feofanov, A. K. & Kippenberg, T. J. On-chip microwave-to-optical quantum coherent converter based on a superconducting resonator coupled to an electro-optic microresonator. *Physical Review A* **94**, 1 (2016).
125. Greganti, C., Roehsner, M. C., Barz, S., Morimae, T. & Walther, P. Demonstration of measurement-only blind quantum computing. *New Journal of Physics* **18**, 303 (2016).
126. Gehl, M., Long, C., Trotter, D., Starbuck, A., Pomerene, A., Wright, J. B., Melgaard, S., Siirola, J., Lentine, A. L. & DeRose, C. Operation of high-speed silicon photonic micro-disk modulators at cryogenic temperatures. *Optica* **4**, 374 (2017).
127. Elshaari, A. W., Zadeh, I. E., Jöns, K. D. & Zwiller, V. Thermo-Optic Characterization of Silicon Nitride Resonators for Cryogenic Photonic Circuits. *IEEE Photonics Journal* **8** (2016).
128. Harris, N. C., Ma, Y., Mower, J., Baehr-Jones, T., Englund, D., Hochberg, M. & Galland, C. Efficient, Compact and Low Loss Thermo-Optic Phase Shifter in Silicon. *Optics Express* **22**, 83 (2014).
129. He, F., Wells, B. O., Ban, Z.-G., Alpay, S. P., Grenier, S., Shapiro, S. M., Si, W., Clark, A. & Xi, X. X. Structural phase transition in epitaxial perovskite films. *Physical Review B* **70**, 235405 (2004).
130. He, F. & Wells, B. O. Lattice strain in epitaxial $BaTiO_3$ thin films. *Applied Physics Letters* **88**, 152908 (2006).
131. Tenne, D. A., Xi, X. X., Li, Y. L., Chen, L. Q., Soukiassian, A., Zhu, M. H., James, A. R., Lettieri, J., Schlom, D. G., Tian, W. & Pan, X. Q. Absence of low-temperature phase transitions in epitaxial $BaTiO_3$ thin films. *Physical Review B - Condensed Matter and Materials Physics* **69**, 2 (2004).
132. Reed, G. T., Mashanovich, G., Gardes, F. Y. & Thomson, D. J. Silicon optical modulators. *Nature Photonics* **4**, 518 (2010).
133. Xu, H., Li, X., Xiao, X., Zhou, P., Li, Z., Yu, J. & Yu, Y. High-speed silicon modulator with band equalization. *Optics Letters* **39**, 4839 (2014).
134. Mahapatra, A. & Murphy, E. J. *Electrooptic Modulators* (eds Kaminow, I. P. & Tingye, L.) 258 (Elsevier, 2002).

135. Chmielak, B., Waldow, M., Matheisen, C., Ripperda, C., Bolten, J., Wahlbrink, T., Nagel, M., Merget, F. & Kurz, H. Pockels effect based fully integrated, strained silicon electro-optic modulator. *Optics Express* **19**, 17212 (2011).
136. Alloatti, L., Korn, D., Palmer, R., Hillerkuss, D., Li, J., Barklund, A., Dinu, R., Wieland, J., Fournier, M., Fedeli, J., Yu, H., Bogaerts, W., Dumon, P., Baets, R., Koos, C., Freude, W. & Leuthold, J. 42.7 Gbit/s electro-optic modulator in silicon technology. *Optics Express* **19**, 11841 (2011).
137. Ding, R., Baehr-Jones, T., Liu, Y., Bojko, R., Witzens, J., Huang, S., Luo, J., Benight, S., Sullivan, P., Fedeli, J. M., Fournier, M., Dalton, L., Jen, A. & Hochberg, M. *A low $V_\pi L$ modulator with GHz bandwidth based on an electro-optic polymer-clad silicon slot waveguide* in *IEEE International Conference on Group IV Photonics GFP* **18** (2010), 201.
138. Chen, L., Chen, J., Nagy, J. & Reano, R. M. Highly linear ring modulator from hybrid silicon and lithium niobate. *Optics Express* **23**, 13255 (2015).
139. Bogaerts, W. & Selvaraja, S. K. Compact single-mode silicon hybrid rib/strip waveguide with adiabatic bends. *IEEE Photonics Journal* **3**, 422 (2011).
140. Yu, Z., Ramdani, J., Curless, J. A., Overgaard, C. D., Finder, J. M., Droopad, R., Eisenbeiser, K. W., Hallmark, J. A., Ooms, W. J. & Kaushik, V. S. Epitaxial oxide thin films on Si(001). *Journal of Vacuum Science & Technology B* **18**, 2139 (2000).
141. Niu, G., Yin, S., Saint-Girons, G., Gautier, B., Lecoeur, P., Pillard, V., Hollinger, G. & Vilquin, B. Epitaxy of $BaTiO_3$ thin film on Si(001) using a $SrTiO_3$ buffer layer for non-volatile memory application. *Microelectronic Engineering* **88**, 1232 (2011).
142. Abel, S., Sousa, M., Rossel, C., Caimi, D., Rossell, M. D., Erni, R., Fompeyrine, J. & Marchiori, C. Controlling tetragonality and crystalline orientation in $BaTiO_3$ nano-layers grown on Si. *Nanotechnology* **24**, 285701 (2013).
143. Vlasov, Y. & McNab, S. Losses in single-mode silicon-on-insulator strip waveguides and bends. *Optics Express* **12**, 1622 (2004).
144. *Handbook of Optical Constants of Solids* (ed Palik, E. D.) (Academic Press, Burlington, 1997).
145. Jalan, B., Engel-Herbert, R., Mates, T. E. & Stemmer, S. Effects of hydrogen anneals on oxygen deficient $SrTiO_3$-x single crystals. *Applied Physics Letters* **93**, 052907 (2008).

146. De Dood, M. J. A., Polman, A., Zijlstra, T. & Van Der Drift, E. W. J. M. Amorphous silicon waveguides for microphotonics. *Journal of Applied Physics* **92**, 649 (2002).
147. Ito, T. U., Higemoto, W., Matsuda, T. D., Koda, A. & Shimomura, K. Shallow donor level associated with hydrogen impurities in undoped $BaTiO_3$. *Applied Physics Letters* **103**, 2011 (2013).
148. Varley, J. B., Janotti, A. & Van De Walle, C. G. Hydrogenated vacancies and hidden hydrogen in $SrTiO_3$. *Physical Review B : Condensed Matter and Materials Physics* **89**, 1 (2014).
149. Yukawa, H., Nakatsuka, K. & Morinaga, M. Electronic structures of hydrogen in perovskite-type oxide, $SrTiO_3$. *Solid State Ionics* **116**, 89 (1999).
150. Baehr-Jones, T., Hochberg, M., Walker, C. & Scherer, A. High-Q optical resonators in silicon-on-insulator-based slot waveguides. *Applied Physics Letters* **86**, 081101 (2005).
151. Sun, R., Dong, P., Feng, N.-n., Hong, C.-y., Michel, J., Lipson, M. & Kimerling, L. Horizontal single and multiple slot waveguides: optical transmission at lambda = 1550 nm. *Optics Express* **15**, 17967 (2007).
152. Shen, Y., Harris, N. C., Skirlo, S., Prabhu, M., Baehr-Jones, T., Hochberg, M., Sun, X., Zhao, S., Larochelle, H., Englund, D. & Soljačić, M. Deep learning with coherent nanophotonic circuits. *Nature Photonics* **11**, 441 (2017).
153. Vandoorne, K., Mechet, P., Van Vaerenbergh, T., Fiers, M., Morthier, G., Verstraeten, D., Schrauwen, B., Dambre, J. & Bienstman, P. Experimental demonstration of reservoir computing on a silicon photonics chip. *Nature Communications* **5**, 3541 (2014).
154. Leinders, S. M., Westerveld, W. J., Pozo, J., van Neer, P., Snyder, B., O'Brien, P., Urbach, H. P., de Jong, N. & Verweij, M. D. A sensitive optical micro-machined ultrasound sensor (OMUS) based on a silicon photonic ring resonator on an acoustical membrane. *Scientific Reports* **5**, 14328 (2015).
155. Reed, G. T., Mashanovich, G. Z., Gardes, F. Y., Milos, N., Youfang, H., Thomson, D. J., Ke, L., Wilson, P. R., Sheng-Wen, C. & Hsu, S. S. *Recent breakthroughs in carrier depletion based silicon optical modulators* 2014.
156. Zhalehpour, S., Lin, J. & Rusch, L. *SiP IQ modulator Linearization by memory polynomial pre-distortion model* in *2017 IEEE Photonics Conference (IPC)* (2017), 317.

157. Xu, K., Yang, L., Sung, J., Chen, Y. M., Cheng, Z. Z., Chow, C., Yeh, C. & Tsang, H. K. Compatibility of Silicon Mach-Zehnder Modulators for Advanced Modulation Formats. *Journal of Lightwave Technology* **31**, 2550 (2013).
158. Janner, D., Tulli, D., García-Granda, M., Belmonte, M. & Pruneri, V. Micro-structured integrated electro-optic $LiNbO_3$ modulators. *Laser & Photonics Reviews* **3**, 301 (2009).
159. Chen, L., Xu, Q., Wood, M. G. & Reano, R. M. Hybrid silicon and lithium niobate electro-optical ring modulator. *Optica* **1**, 112 (2014).
160. Leuthold, J., Koos, C., Freude, W., Alloatti, L., Palmer, R., Korn, D., Pfeifle, J., Lauermann, M., Dinu, R., Wehrli, S., Jazbinsek, M., Günter, P., Waldow, M., Wahlbrink, T., Bolten, J., Kurz, H., Fournier, M., Fedeli, J., Yu, H. & Bogaerts, W. Silicon-Organic Hybrid Electro-Optical Devices. *IEEE Journal of Selected Topics in Quantum Electronics* **19**, 114 (2013).
161. Heni, W., Kutuvantavida, Y., Haffner, C., Zwickel, H., Kieninger, C., Wolf, S., Lauermann, M., Fedoryshyn, Y., Tillack, A. F., Johnson, L. E., Elder, D. L., Robinson, B. H., Freude, W., Koos, C., Leuthold, J. & Dalton, L. R. Silicon-Organic and Plasmonic-Organic Hybrid Photonics. *ACS Photonics* **4**, 1576 (2017).
162. Abel, S. & Fompeyrine, J. in *Thin Films on Silicon* 455 (World Scientific, 2015).
163. Petraru, A., Schubert, J., Schmid, M., Trithaveesak, O. & Buchal, C. Integrated optical Mach Zehnder modulator based on polycrystalline $BaTiO_3$. *Optics Letters* **28**, 2527 (2003).
164. Girouard, P., Chen, P., Jeong, Y. K., Liu, Z., Ho, S.-t. & Wessels, B. W. $\chi^{(2)}$ Modulator With 40-GHz Modulation Utilizing $BaTiO_3$ Photonic Crystal Waveguides. *IEEE Journal of Quantum Electronics* **53**, 5200110 (2017).
165. Meier, A. R., Niu, F. & Wessels, B. W. Integration of $BaTiO_3$ on Si (001) using MgO/STO buffer layers by molecular beam epitaxy. *Journal of Crystal Growth* **294**, 401 (2006).
166. Eltes, F., Kroh, M., Caimi, D., Mai, C., Popoff, Y., Winzer, G., Petousi, D., Lischke, S., Ortmann, J. E., Czornomaz, L., Zimmermann, L., Fompeyrine, J. & Abel, S. *A novel 25 Gbps electro-optic Pockels modulator integrated on an advanced Si photonic platform* in *2017 IEEE International Electron Devices Meeting (IEDM)* (San Francisco, CA, USA, 2017), 24.5.1.

167. Messner, A., Eltes, F., Ma, P., Abel, S., Baeuerle, B., Josten, A., Heni, W., Caimi, D., Fompeyrine, J. & Leuthold, J. *Integrated Ferroelectric Plasmonic Optical Modulator* in *2017 Optical Fiber Communications Conference (OFC)* (Optical Society of America, Los Angeles, 2017), Th5C.7.
168. Czornomaz, L., Daix, N., Kerber, P., Lister, K., Caimi, D., Rossel, C., Sousa, M., Uccelli, E. & Fompeyrine, J. *Scalability of ultra-thin-body and BOX InGaAs MOSFETs on silicon* in *2013 Proceedings of the European Solid-State Device Research Conference (ESSDERC)* (2013), 143.
169. Czornomaz, L., Daix, N., Uccelli, E., Djara, V., Caimi, D., Rossel, C., Sousa, M., Siegwart, H., Marchiori, C., Hartmann, J.-M. & Fompeyrine, J. Wafer Bonding: An Integration Route for Hybrid III-V/SiGe CMOS on 300 mm. *ECS Transactions* **64**, 199 (2014).
170. Bogaerts, W., Heyn, P. D., Vaerenbergh, T. V., Vos, K. D. & Kumar, S. Silicon microring resonators. *Laser & Photonics Reviews* **73**, 47 (2012).
171. Li, G., Zheng, X., Yao, J., Thacker, H., Shubin, I., Luo, Y., Raj, K., Cunningham, J. E. & Krishnamoorthy, A. V. 25 Gb/s 1V-driving CMOS ring modulator with integrated thermal tuning. *Optics Express* **19**, 20435 (2011).
172. Brosi, J.-M., Koos, C., Andreani, L. C., Waldow, M., Leuthold, J. & Freude, W. High-speed low-voltage electro-optic modulator with a polymer-infiltrated silicon photonic crystal waveguide. *Optics Express* **16**, 4177 (2008).
173. Borghi, M., Mancinelli, M., Bernard, M., Ghulinyan, M., Pucker, G. & Pavesi, L. Homodyne Detection of Free Carrier Induced Electro-Optic Modulation in Strained Silicon Resonators. *Journal of Lightwave Technology* **34**, 5657 (2016).
174. *Measurement of High-Speed Signals in Solid State Devices* (ed Marcus, R. B.) (Elsevier, 1990).
175. Müller, J., Merget, F., Azadeh, S. S., Hauck, J., García, S. R., Shen, B. & Witzens, J. Optical Peaking Enhancement in High-Speed Ring Modulators. *Scientific Reports* **4**, 6310 (2014).
176. Zhou, Q., Lau, S., Wu, D. & Shung, K. K. Piezoelectric films for high frequency ultrasonic transducers in biomedical applications. eng. *Progress in materials science* **56**, 139 (2011).
177. Rabe, K. M., Ahn, C. H. & Triscone, J.-M. *Physics of Ferroelectrics: A Modern Perspective* 1st (Springer Publishing Company, Incorporated, 2007).
178. Rouvalis, E. *Indium Phosphide Based IQ-Modulators for Coherent Pluggable Optical Transceivers* 2015.

179. Zhang, Y., Han, R. & Xiang, T. *Application of non-contact optic voltage sensor based on Pockels effect in ±800 kV convertor station* in *2016 IEEE International Conference on High Voltage Engineering and Application (ICHVE),* (2016).
180. Stan, N., Seng, F., Shumway, L., King, R. & Schultz, S. Non-perturbing voltage measurement in a coaxial cable with slab-coupled optical sensors. *Applied Optics* **56**, 6814 (2017).
181. Jin, T., Li, L., Zhang, B., Lin, H.-Y. G., Wang, H. & Lin, P. T. Monolithic Mid-Infrared Integrated Photonics Using Silicon-on-Epitaxial Barium Titanate Thin Films. *ACS Applied Materials & Interfaces* **9**, 21848 (2017).
182. Ríos, C., Stegmaier, M., Hosseini, P., Wang, D., Scherer, T., Wright, C. D., Bhaskaran, H. & Pernice, W. H. P. Integrated all-photonic non-volatile multi-level memory. *Nature Photonics* **9**, 725 (2015).
183. Hochberg, M. & Baehr-Jones, T. Towards fabless silicon photonics. *Nature Photonics* **4**, 492 (2010).
184. Cazzanelli, M., Bianco, F., Borga, E., Pucker, G., Ghulinyan, M., Degoli, E., Luppi, E., Véniard, V., Ossicini, S., Modotto, D., Wabnitz, S., Pierobon, R. & Pavesi, L. Second-harmonic generation in silicon waveguides strained by silicon nitride. *Nature Materials* **11**, 148 (2012).
185. Eltes, F., Ortmann, J. E., Urbonas, D., Caimi, D., Czornomaz, L., Mai, C., Zimmermann, L., Fompeyrine, J. & Abel, S. *Record High Pockels Coefficient in PIC-Compatible $BaTiO_3$/Si Photonic Devices* in *2018 European Conference on Optical Communication* (2018), We4C.1.
186. Knoll, D., Lischke, S., Barth, R., Zimmermann, L., Heinemann, B., Rucker, H., Mai, C., Kroh, M., Peczek, A., Awny, A., Ulusoy, C., Trusch, A., Kruger, A., Drews, J., Fraschke, M., Schmidt, D., Lisker, M., Voigt, K., Krune, E. & Mai, A. *High-performance photonic BiCMOS process for the fabrication of high-bandwidth electronic-photonic integrated circuits* in *Technical Digest - International Electron Devices Meeting, IEDM* (2015), 15.6.1.
187. Huang, W., Liu, Y., Luo, Z., Hou, C., Zhao, W., Yin, Y. & Li, X. Ferroelectric domain switching dynamics and memristive behaviors in $BiFeO_3$-based magnetoelectric heterojunctions. *Journal of Physics D: Applied Physics* **51**, 234005 (2018).
188. Masood, A., Pantouvaki, M., Lepage, G., Verheyen, P., Van Campenhout, J., Absil, P., Van Thourhout, D. & Bogaerts, W. *Comparison of heater architectures for thermal control of silicon photonic circuits* in *IEEE International Conference on Group IV Photonics GFP* **ThC2** (2013), 83.

189. Hamano, T., Towner, D. J. & Wessels, B. W. Relative dielectric constant of epitaxial BaTiO 3 thin films in the GHz frequency range. *Applied Physics Letters* **83**, 5274 (2003).
190. Hoerman, B. H., Ford, G. M., Kaufmann, L. D. & Wessels, B. W. Dielectric properties of epitaxial $BaTiO_3$ thin films. *Applied Physics Letters* **73**, 2248 (1998).
191. Messner, A., Eltes, F., Ma, P., Abel, S., Baeuerle, B., Josten, A., Caimi, D., Fompeyrine, J. & Leuthold, J. Plasmonic Ferroelectric Modulators. *Journal of Lightwave Technology* **37**, 281 (2019).
192. Dong, P., Liu, X., Chandrasekhar, S., Buhl, L. L., Aroca, R., Baeyens, Y. & Chen, Y. *224-Gb/s PDM-16-QAM modulator and receiver based on silicon photonic integrated circuits* in *2013 Optical Fiber Communication Conference (OFC/NFO)* (2013), 1.
193. Wolf, S., Hartmann, W., Lauermann, M., Zwickel, H., Kutuvantavida, Y., Kieninger, C., Freude, W. & Koos, C. *High-speed silicon-organic hybrid (SOH) modulators* in *42th European Conf. Opt. Commun. (ECOC'16)* (VDE, Berlin, Offenburg, 2016).
194. Alloatti, L., Palmer, R., Diebold, S., Pahl, K. P., Chen, B., Dinu, R., Fournier, M., Fedeli, J. M., Zwick, T., Freude, W., Koos, C. & Leuthold, J. 100 GHz silicon-organic hybrid modulator. *Light: Science and Applications* **3**, 5 (2014).
195. Pankove, J. I. Temperature Dependence of Emission Efficiency and Lasing Threshold in Laser Diodes. *IEEE Journal of Quantum Electronics* **4**, 119 (1968).
196. Hadfield, R. H. Single-photon detectors for optical quantum information applications. *Nature Photonics* **3**, 696 (2009).
197. Lauermann, M., Wolf, S., Schindler, P. C., Palmer, R., Koeber, S., Korn, D., Alloatti, L., Wahlbrink, T., Bolten, J., Waldow, M., Koenigsmann, M., Kohler, M., Malsam, D., Elder, D. L., Johnston, P. V., Phillips-Sylvain, N., Sullivan, P. A., Dalton, L. R., Leuthold, J., Freude, W. & Koos, C. 40 GBd 16QAM Signaling at 160 Gb/s in a Silicon-Organic Hybrid Modulator. *Journal of Lightwave Technology* **33**, 1210 (2015).
198. Wang, C., Zhang, M., Stern, B., Lipson, M. & Loncar, M. Nanophotonic Lithium Niobate Electro-optic Modulators. *Optics Express* **26**, 1547 (2018).
199. Eltes, F., Mai, C., Caimi, D., Kroh, M., Popoff, Y., Winzer, G., Petousi, D., Lischke, S., Ortmann, J. E., Czornomaz, L., Zimmermann, L., Fompeyrine, J. & Abel, S. A $BaTiO_3$-based electro-optic Pockels modulator

monolithically integrated on an advanced silicon photonics platform. *Journal of Lightwave Technology* **37**, 1456 (2019).

200. Lu, H., Sadani, B., Courjal, N., Ulliac, G., Smith, N., Stenger, V., Collet, M. & Bernal, M. Enhanced electro-optical lithium niobate photonic crystal wire waveguide on a smart-cut thin film. *Optics Express* **20**, 2974 (2012).
201. Muñoz, P., Micó, G., Bru, L. A., Pastor, D., Pérez, D., Doménech, J. D., Fernández, J., Baños, R., Gargallo, B., Alemany, R., Sánchez, A. M., Cirera, J. M., Mas, R. & Domínguez, C. Silicon nitride photonic integration platforms for visible, near-infrared and mid-infrared applications. *Sensors* **17**, 2088 (2017).
202. Ma, Z., Ma, Y., Chen, Z., Zheng, F., Gao, H., Liu, H. & Chen, H. Modeling of hysteresis loop and its applications in ferroelectric materials. *Ceramics International* **44**, 4338 (2018).
203. Zafar, S., Jones, R. E., Jiang, B., White, B., Kaushik, V. & Gillespie, S. The electronic conduction mechanism in barium strontium titanate thin films. *Applied Physics Letters* **73**, 3533 (1998).

ACKNOWLEDGMENTS

During the past 4.5 years at IBM, I have been fortunate enough to interact with many people who have supported me in different ways. I would in particular like to thank:

Stefan Abel and Jean Fompeyrine for the opportunity to work with them for the past years, and for their supervision during this time. It has been a pleasure and I have learned very much. I would especially like to thank Jean for accepting me as a masters student after a 5 am (PST) phone call.

Prof. Manfred Fiebig for agreeing to be my ETH advisor during my PhD, for his continuous support, and for the fruitful collaborations with his group.

Prof. Jérôme Faist and Frédéric Boeuf for co-refereeing this thesis.

Bert Offrein, my manager at IBM, for supporting my work and for giving me many chances to interact with the scientific community through collaborations and conferences.

Andreas Messner for the intense and exciting collaboration on plasmonic modulators.

IBMers past and present:

Daniele Caimi for offering his services as master wafer bonder as well as advice on various other aspects of processing.

Lukas Czornomaz for providing his invaluable insights on processing and integration, for EBL exposures at all hours of the day, for taking an interest in and supporting my work, and for hops smuggling.

Youri Popoff for his support with various cleanroom processing, often long past office hours, for the shared experience in W288.

Veeresh Deshpande for his encyclopedic knowledge of cleanroom processing, for sharing the experience at Cantillon.

Heinz Siegwart for taking care of Natasha.

Antonis Olziersky for running countless EBL jobs, often at unreasonable schedules.

Marilyne Sousa for teaching me the art of FIB lamella preparation.

Clarissa Convertino for the shared experience of processing day and night for an IEDM deadline.

Nico Mosso for sharing the duty as Predoc Presidents.

Peter Reininger for many deep technical discussions on s. cerevisiae processing.

Jackie Geler-Kremer, Elliott Ortmann, Marc Seifried, Darius Urbonas, Yannick Baumgartner, Mattia Halter, Kristy Kormondy, Florian Fallegger for making my time at IBM even more enjoyable.

Collaborators:

Lars Zimmermann, Marcel Kroh, and Despoina Petousi from IHP, for the great collaboration on integration of BTO with silicon photonics.

Jorge Barreto and the rest of the Bristol team for for their invaluable contributions to the cryogenic characterization, and for introducing me to cryogenic experiments.

Morgan Trassin, Gabriele de Luca, and Johanna Nordlander for their efforts on SHG characterization of BTO.

CONTRIBUTIONS TO THIS THESIS

This thesis is the result of many scientific collaborations. This section briefly outlines the contributions of myself and others to this work, chapter by chapter. All molecular wafer bonding in this work was performed by Daniele Caimi. All MBE depositions were performed by myself except where noted. The work was performed at IBM Research – Zurich, unless otherwise stated.

Chapter 2 - Barium titanate

The existing process for BTO deposition was transferred from a 2" tool to an 8" tool by myself. The XRD data was acquired by myself. STEM sample preparation and imaging was performed by myself. The second harmonic experiments were performed by Gabriele De Luca, Johanna Nordlander, Jacob Nürnberg and Morgan Trassin at ETH Zürich. The modeling and fitting of the data was performed by myself.

Chapter 3 - Optical losses in BTO-Si devices

The MBE growth in this chapter was performed by Jean Fompeyrine and Florian Fallegger. The device fabrication was performed by myself, Stefan Abel and Daniele Caimi. Optical measurements and data analysis were performed by myself. Annealing experiments were performed by myself, Daniele Caimi and Eamon O'Connor. XPS measurements and data analysis was performed by myself. STEM sample preparation and imaging was performed by Marilyne Sousa and Marta Rossell.

Chapter 4 - The Pockels effect in BTO-Si devices

This work was performed in collaboration with the Nanophotonics Technology Center at Universitat Politècnica de València. The XRD measurements and analysis was performed by myself and Jean Fompeyrine. STEM sample preparation and imaging was performed by myself. Device layouting was performed by myself. Device fabrication was performed by myself and

Daniele Caimi. Electro-optic characterization and data analysis was performed by Elliott Ortmann and Stefan Abel. Data transmission experiments were performed by Pau Castera, Alvaro Rosa, Ana M. Gutierrez, and Elliott Ortmann at UP València. Simulations to extract the Pockels coefficients were performed by Darius Urbonas.

Chapter 5 - A monolithically integrated Pockels modulator

This work was performed in collaboration with HIP microelectronics. PIC wafers were supplied by IHP. Device design was performed by Despoina Petousi. Molecular wafer bonding of BTO to PIC wafers was developed by Daniele Caimi and Christian Mai. 200 mm wafer bonding was performed by myself and Daniele Caimi. Device fabrication was performed by myself. STEM sample preparation and imaging was performed by myself. DC electro-optic characterization as performed by myself. RF characterization was performed at IHP by myself and Marcel Kroh.

Chapter 6 - Plasmonic BTO modulators

This work was performed in collaboration with ETH Zürich. Development of the plasmonic fabrication process was performed by myself. STEM sample preparation and imaging was performed by myself. Device fabrication was performed by myself. Electro-optic characterization was performed at ETH Zürich by myself and Andreas Messner. Data transmission experiments were performed at ETH Zürich by myself, Andreas Messner, Wolfgang Heni, Benedikt Baeuerle, and Arne Josten.

Chapter 7 - BTO for cryogenic photonic circuits

This work was performed in collaboration with the University of Bristol. Device design and device fabrication was performed by myself. Low-temperature electro-optic characterization was performed at the University of Bristol by myself, Gerrardo Villarreal-Garcia, Andy Hart, Andreas Gentile, Graham Marshall, and Jorge Barreto. Data analysis was performed by myself. Low temperature electrical measurements was performed by myself with support from Pascal Stark and Siegfried Karg.

PUBLICATIONS

Articles in peer-reviewed journals originating from results achieved during doctorate:

- *A $BaTiO_3$-based electro-optic Pockels modulator monolithically integrated on an advanced silicon photonics platform*
  F. Eltes, C. Mai, D. Caimi, M. Kroh, Y. Popoff, G. Winzer, D. Petousi, S. Lischke, J. E. Ortmann, L. Czornomaz, L. Zimmermann, J. Fompeyrine, S. Abel.
  Journal of Lightwave Technology **37**, 1456 (2019)
  Contribution: MBE growth, 200 mm bonding, modulator fabrication, STEM sample preparation and imaging, modulator characterization, data analysis.

- *Large Pockels effect in micro- and nano-structured barium titanate integrated on silicon*
  (S. Abel*, F. Eltes*) *equal contributions, J. E. Ortmann, A. Messner, P. Castera, T. Wagner, D. Urbonas, A. Rosa, A. M. Gutierrez, D. Tulli, P. Ma, B. Baeuerle, A. Josten, W. Heni, D. Caimi, L. Czornomaz, A. A. Demkov, J. Leuthold, P. Sanchis, J. Fompeyrine.
  Nature Materials **18**, 42 (2019)
  Contribution: MBE growth, AFM measurements, XRD measurements, device design, device fabrication, STEM sample preparation and imaging, characterization of plasmonic devices.
  - See also: *Strong Pockels materials*
    M. Li, H. X. Tang. News and Views, *Nature Materials* **18**, 9 (2019)

- *Plasmonic Ferroelectric Modulators*
  A. Messner, F. Eltes, P. Ma, S. Abel, B. Baeuerle, A. Josten, W. Heni, D. Caimi, J. Fompeyrine, J. Leuthold.
  Journal of Lightwave Technology **37**, 42 (2019)
  Contribution: MBE growth, device design, device fabrication, SEM imaging, device characterization.

- *Stabilization of ferroelectric $Hf_xZr_{1-x}O_2$ films using a millisecond flash lamp annealing technique*
  E. O'Connor, M. Halter, F. Eltes, M. Sousa, A. Kellock, S. Abel, J. Fompeyrine.
  APL Materials **6**, 121103 (2018)
  Contribution: HRSTEM sample preparation and imaging.

- *Strain enhancement of the electro-optical response in $BaTiO_3$ films integrated on Si(001)*
  K. D. Fredrickson, V. V. Vogler-Neuling, K. J. Kormondy, D. Caimi, F. Eltes, M. Sousa, J. Fompeyrine, S. Abel, A. A. Demkov.
  Physical Review B **98**, 75136 (2017)
  Contribution: MBE growth of STO and BTO.

- *Low Temperature Epitaxial Barium Titanate Thin Film Growth in High Vacuum CVD*
  M. Reinke, Y. Kuzminykh, F. Eltes, S. Abel, T. LaGrange, A. Neels, J. Fompeyrine, P. Hoffmann.
  Advanced Materials Interfaces **4**, 1700116 (2018)
  Contribution: MBE growth of STO.

- *Microstructure and ferroelectricity of $BaTiO_3$ thin films on Si for integrated photonics*
  K. J. Kormondy, Y. Popoff, M. Sousa, F. Eltes, D. Caimi, M. D. Rossell, M. Fiebig, P. Hoffmann, C. Marchiori, M. Reinke, M. Trassin, A. A. Demkov, J. Fompeyrine, S. Abel.
  Nanotechnology **28**, 075706 (2017)
  Contribution: HRSTEM sample preparation and imaging.

- *Barium titanate ($BaTiO_3$) RF characterization for application in electro-optic modulators*
  A. Rosa, D. Tulli, P. Castera, A.M. Gutierrez, A. Griol, M. Baquero, B. Vilquin, F. Eltes, S. Abel, J. Fompeyrine, P. Sanchis.
  Optical Materials Express **7**, 4328 (2017)
  Contribution: MBE growth of STO and BTO.

- *Barium titanate ($BaTiO_3$) RF characterization for application in electro-optic modulators*
  F. Eltes, D. Caimi, F. Fallegger, M. Sousa, E. O'Connor, M.D. Rossell, B. Offrein, J. Fompeyrine, S. Abel.
  ACS Photonics **3**, 1698 (2016)
  Contribution: Optical mode simulations, device fabrication, loss measurements and data analysis, XPS measurements and data analysis.

Papers presented at international conferences during doctorate:

- *$BaTiO_3$-based modulators for integrated optical interconnects*
  F. Eltes, J. Fompeyrine, S. Abel.
  SPIE Photonics West, Optical Interconnects XIX, San Francisco (2019). (Invited)

- *First cryogenic electro-optic switch on silicon with high bandwidth and low power tunability*
  F. Eltes, J. Barreto, D. Caimi, S. Karg, A. A. Gentile, A. Hart, P. Stark, N. Meier, M. G. Thompson, J. Fompeyrine, S. Abel.
  IEEE International Electron Devices Meeting (IEDM), San Francisco (2018).

- *Silicon photonics enhanced with nonlinear barium titanate thin films*
  F. Eltes.
  European Optical Society Biennial Meeting (EOSAM), Delft (2018). (Invited)

- *Monolithic Integration of Si/$BaTiO_3$ Electro-Optic Modulators on a Silicon Photonics Platform*
  F. Eltes, D. Caimi, C. Mai, G. Winzer, D. Petousi, S. Lischke, L. Czornomaz, L. Zimmermann, J. Fompeyrine, S. Abel.
  IEEE Photonics Conference (IPC), Reston (2018). (Best student paper award)

- *Record High Pockels Coefficient in PIC-Compatible $BaTiO_3$/Si Photonic Devices*
  F. Eltes, J. E. Ortmann, D. Urbonas, D. Caimi, L. Czornomaz, C. Mai, L. Zimmermann, J. Fompeyrine, S. Abel.
  European Conference on Optical Communication (ECOC), Rome

(2018).

- *Integrated Ferroelectric $BaTiO_3$/Si Plasmonic Modulator for 100 Gbit/s and Beyond*
  (A. Messner*, F. Eltes*) *equal contributions, P. Ma, S. Abel, B. Baeuerle, A. Josten, W. Heni, D. Caimi, J. Fompeyrine, J. Leuthold.
  Optical Fiber Communications Conference (OFC), San Diego (2018). (Invited)

- *A novel 25 Gbps electro-optic Pockels modulator integrated on an advanced Si photonic platform*
  F. Eltes, M. Kroh, D. Caimi, C. Mai, Y. Popoff, G. Winzer, D. Petousi, S. Lischke, J.E. Ortmann, L. Czornomaz, L. Zimmermann, J. Fompeyrine, S. Abel.
  IEEE International Electron Devices Meeting (IEDM), San Francisco (2017). (Best student paper award)

- *Integrated Ferroelectric Plasmonic Optical Modulator*
  (A. Messner*, F. Eltes*) *equal contributions, P. Ma, S. Abel, B. Baeuerle, A. Josten, W. Heni, D. Caimi, J. Fompeyrine, J. Leuthold.
  Optical Fiber Communications Conference (OFC), San Diego (2017). (Postdeadline paper)